HHS Public Access

Author manuscript

Prog Nucl Magn Reson Spectrosc. Author manuscript; available in PMC 2020 June 01.

Published in final edited form as:

Prog Nucl Magn Reson Spectrosc. 2019 ; 112-113: 55–102. doi:10.1016/j.pnmrs.2019.05.002.

Characterizing micro-to-millisecond chemical exchange in nucleic acids using offresonance $R_{1\rho}$ relaxation dispersion

Atul Rangadurai[1], **Eric S. Szymaski**[1], **Isaac J. Kimsey**[1,2], **Honglue Shi**[3], **Hashim M. Al-Hashimi**[1,3,*]

[1]Department of Biochemistry, Duke University School of Medicine, Durham, NC, 27710, USA

[2]Present address Nymirum, 4324 S. Alston Avenue, Durham, NC, 27713, USA

[3]Department of Chemistry, Duke University, Durham, NC, 27710, USA

Abstract

This review describes off-resonance $R_{1\rho}$ relaxation dispersion NMR methods for characterizing microsecond-to-millisecond chemical exchange in uniformly $^{13}C/^{15}N$ labeled nucleic acids in solution. The review opens with a historical account of key developments that formed the basis for modern $R_{1\rho}$ techniques used to study chemical exchange in biomolecules. A vector model is then used to describe the $R_{1\rho}$ relaxation dispersion experiment, and how the exchange contribution to relaxation varies with the amplitude and frequency offset of an applied spin locking field, as well as the population, exchange rate, and differences in chemical shifts of two exchanging species. Mathematical treatment of chemical exchange based on the Bloch-McConnell equations is then presented and used to examine relaxation dispersion profiles for more complex exchange scenarios including three-state exchange. Pulse sequences that employ selective Hartmann-Hahn cross-polarization transfers to excite individual ^{13}C or ^{15}N spins are then described for measuring off-resonance $R_{1\rho}(^{13}C)$ and $R_{1\rho}(^{15}N)$ in uniformly $^{13}C/^{15}N$ labeled DNA and RNA samples prepared using commercially available $^{13}C/^{15}N$ labeled nucleotide triphosphates. Approaches for analyzing $R_{1\rho}$ data measured at a single static magnetic field to extract a full set of exchange parameters are then presented that rely on numerical integration of the Bloch-McConnell equations or the use of algebraic expressions. Methods for determining structures of nucleic acid excited states are then reviewed that rely on mutations and chemical modifications to bias conformational equilibria, as well as structurebased approaches to calculate chemical shifts. Applications of the methodology to the study of DNA and RNA conformational dynamics are reviewed and the biological significance of the exchange processes is briefly discussed.

*To whom correspondence should be addressed: hashim.al.hashimi@duke.edu, Tel: 919-660-1113, Fax: 919-684-8885.

Declaration of Interests

Hashim M. Al-Hashimi (H.M.A.) is an advisor to and holds an ownership interest in Nymirum Inc., which is an RNA-based drug discovery company. The research reported in this article was performed by Duke University faculty and students and was funded by NIH and NIGMS contracts to H.M.A.

Dedication: This review is dedicated to Prof. James H. Prestegard on the occasion of his 75th birthday

Graphical abstract

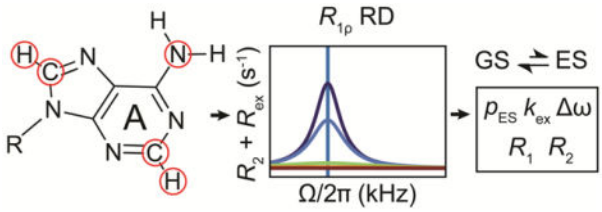

Keywords

$R_{1\rho}$ relaxation dispersion; chemical exchange; nucleic acid dynamics; Hoogsteen; tautomers

1. Introduction

The fundamental importance of conformational flexibility to the biological function of nucleic acids was evident at the birth of structural biology when it was immediately apparent that the two strands in DNA had to come apart to allow access to genetic information[1]. However only over the past decade, thanks in part to developments in solution-state NMR[2–6], has the true nature of nucleic acid flexibility and its roles in replication, gene expression, and regulation come to light[3, 4, 7–9]. Like proteins, the structures of nucleic acids undergo complex fluctuations over timescales spanning more than twelve orders of magnitude from picoseconds to seconds[10–12].

Here, we review methods based on the measurement of $R_{1\rho}(^{13}C)$ and $R_{1\rho}(^{15}N)$ relaxation dispersion (RD)[13, 14] for characterizing microsecond-to-millisecond chemical exchange in uniformly $^{13}C/^{15}N$ labeled nucleic acids in solution. Motions on this timescale are of particular interest because they coincide with the timescales for breaking base pairs (BPs, see glossary for abbreviations), the basic building block of nucleic acid structure. These motions can lead to formation of high-energy non-native conformations referred to as “excited states” (ESs)[15] that correspond to local minima in the free energy landscape. ESs have structural and therefore functional properties that can differ substantially from the native “ground state” (GS) conformation, enabling them to serve as molecular switches or targets for drug discovery. $R_{1\rho}$ RD experiments have revealed a wide variety of such motions in DNA and RNA, which were previously unknown, and are now believed to play important roles in gene expression and regulation[9, 11, 16–18].

$R_{1\rho}$ is one of several RD experiments that can be used to characterize microsecond-tomillisecond chemical exchange. $R_{1\rho}$ experiments offer some advantages relative to Carr Purcell-Meiboom-Gill (CPMG) experiments[19, 20], particularly for nucleic acid applications given the scarcity of ideal ^{15}N spin probes[9, 21]. These advantages include enhanced sensitivity to faster microsecond timescale motions[22], ability to robustly determine a complete set of exchange parameters using experiments performed at a single static magnetic field[23], and perhaps most importantly, applicability to uniformly $^{13}C/^{15}N$ labeled samples[13, 21], which can be readily prepared using standard biochemical protocols. However, relative to CPMG, offresonance $R_{1\rho}$ experiments can be more difficult

to implement, and perhaps for this reason, have not been as widely applied to the study of chemical exchange in biomolecules. The goal of this review is to provide readers with the conceptual foundations needed to use $R_{1\rho}$ RD experiments for characterizing chemical exchange. While the focus is on nucleic acids, many topics covered should be of utility to those interested in studying proteins, and to those who are using other RD methods to characterize chemical exchange in nucleic acids. The reader is also referred to other excellent reviews on $R_{1\rho}$ RD methods, with specific application to proteins[5, 13]. It should be noted that in recent years, there have also been significant developments in the application of Chemical Exchange Saturation Transfer (CEST) experiments for characterizing slow millisecond timescale chemical exchange in proteins[24–27], that have been extended to nucleic acids[28–32] and that afford advantages similar to those of $R_{1\rho}$.

The review is organized in the following manner: Section 2 provides a historical account of key developments that led to $R_{1\rho}$ RD methods described here. Section 3 uses a vector model to describe dephasing of the magnetization during the $R_{1\rho}$ experiment as a conceptual framework for understanding basic aspects of the experiment, with a focus on two-state exchange. This is followed by mathematical treatment of chemical exchange using the Bloch-McConnell equations in Section 4. Section 5 reviews pulse sequences for measuring offresonance $R_{1\rho}(^{13}\mathrm{C})$ and $R_{1\rho}(^{15}\mathrm{N})$ RD in uniformly labeled nucleic acids while Section 6 is devoted to data analysis methods to obtain the exchange parameters. Section 7 reviews methods for determining structures of nucleic acid ESs, and finally Section 8 reviews some example applications to DNA and RNA. Since we have carried out many off-resonance $R_{1\rho}$ studies of chemical exchange in nucleic acids, most of the applications reviewed in Sections 7 and 8 come from our group. However, to provide a more balanced perspective of what is now a rapidly evolving field applying a range of NMR RD methods to the study of chemical exchange in nucleic acids, we also refer to earlier on-resonance $R_{1\rho}$ studies which set the stage for the off resonance $R_{1\rho}$ applications, and also make references to CPMG and CEST studies of nucleic acids when appropriate.

2. Brief historical account of relaxation dispersion in NMR with a focus on $R_{1\rho}$ and nucleic acids

The theoretical and experimental underpinnings of NMR RD techniques were conceived soon after the observation of NMR in condensed matter systems independently by Bloch, Hansen, and Packard at Stanford University[33], and by Purcell, Torrey, and Pound at Harvard University[34]. Examining the historical progression from these initial studies helps one to highlight the motivation behind these developments, which frequently was unrelated to measuring dynamics, as well as key challenges that had to be overcome to make modern biological applications possible. We will find that, while the basics of RD experiments were conceived for applications to small organic molecules, the desire to characterize chemical exchange in biomolecules drove key developments in both theory and experiment that made it possible to robustly and quantitatively extract exchange parameters of interest. While the focus will be on $R_{1\rho}$, we shall also make references to CPMG and CEST RD experiments to help place these developments into a broader context. A timeline showing some of the milestones to the development of RD NMR is provided in Fig. 1. While we have tried our

best to provide an accurate portrayal of this history, this is not intended to be an exhaustive compilation of the many important contributions to the development of RD NMR, and we apologize for any omissions.

2.1. 1930–1960: Genesis of NMR relaxation dispersion methods

The $R_{1\rho}$ experiment involves measuring exchange contributions (R_{ex}) to nuclear spin relaxation in the rotating frame. The phenomenon of spin relaxation and its experimental measurement was well established for electrons even before the observation of NMR by Bloch and Purcell. The Dutch physicist Cornelis Gorter first reported electron spin-lattice and spinspin relaxation in the mid 1930s[35, 36]. Gorter found that the electron magnetic moments of paramagnetic substances such as the sulfate salts of iron and chromium needed some time to return back to equilibrium after changing the external magnetic field[36]. Gorter, who is credited with coining the term “NMR”[37], is also well-known for his unsuccessful attempt to observe NMR, a failure which ironically could be attributed to his poor choice of lithium fluoride as a sample given its long spin-lattice relaxation time[38].

Theoretical estimates for nuclear spin-lattice relaxation times were available as early as the 1930s[39]. Some of the first quantitative experimental measurements were performed in 1948, when Pound *et al.* measured spin-lattice (T_1) and spin-spin (T_2) relaxation times in condensed matter[40]. Pound also derived expressions relating T_1 and T_2 to the rotational correlation time, thus establishing a link between relaxation and dynamics[40]. Later efforts were focused on improving the methods used to measure T_1 and T_2[41–43]. While attempting to develop methods for measuring T_1, Erwin Hahn “accidently” discovered the spin-echo which would prove invaluable to measure T_2 and form the basis for the very first RD experiments[44]. A few years later, Carr, Purcell, Meiboom, and Gill[19, 20] extended the spin-echo into a series of 180° pulses to suppress contributions of the static field inhomogeneity and of translational diffusion, resulting in the development of the CPMG experiment. As an unintended consequence, the train of 180° pulses also provided a means to suppress R_{ex} to a variable extent, thus forming the basis for the CPMG RD experiment (see below).

The phenomena of chemical exchange and many aspects of RD experiments can be described without recourse to a quantum description. The origins of the Bloch-McConnell (B-M) equations[45], which constitute the theoretical foundation for NMR RD experiments, can be traced back to the phenomenological Bloch equations, which were introduced in 1946, that use classical physics to describe the motion of macroscopic nuclear magnetization. Bloch realized that bulk magnetization resulting from the application of a longitudinal magnetic field (B_0) could be forced to undergo precession by application of a transverse magnetic field. He developed equations to describe this dynamic behavior that also treat the influence of T_1 and T_2 relaxation on the magnetization[46]. Bloch theorized that forced precession would induce an electric signal (“nuclear induction”) in an appropriately placed coil, and subsequently verified this prediction using a water sample[33]. Gutowsky, Slichter, Meiboom and others[47–51] later extended the Bloch equations and developed expressions that took into account the influence of chemical exchange on the behavior of magnetization in the absence of transverse magnetic fields.

These expressions helped explain why line shapes changed when altering temperature or pH. In the late 1950s, McConnell recognized that chemical exchange provides mechanisms for directly transferring components of magnetization between exchanging states (i.e., $M_{ji} \rightarrow M_{ki}$; $i = x, y$ or z; for states j and k), and explicitly introduced exchange terms into the Bloch equations to take this transfer into account, resulting in the development of the B-M equations[45]. Hahn independently came to a similar realization even earlier in 1952 while accounting for the influence of scalar couplings and chemical shifts during spin-echoes[52].

As is the case for CPMG, the $R_{1\rho}$ experiment was not conceived for the purpose of measuring chemical exchange. In the mid 1950s, while developing a theory to account for the magnetic behavior of solids under the influence of strong transverse radio frequency (RF) fields, Redfield discovered a phenomenon that he referred to as “rotary saturation” or “saturation in the rotating frame”[53]. Redfield realized that one could spin-lock magnetization along an effective field direction through application of an RF field. Inspired by Rabi’s picture of the rotating frame[54], Redfield recognized that spin-locked magnetization could be tilted through application of a second RF field perpendicular to the effective field, in a manner analogous to how Bloch tilted magnetization away from the B_0 field[33]. The subsequent recovery of the magnetization along the effective field following removal of the second RF field was described by a relaxation time $T_{1\rho}$, which Redfield recognized to be sensitive to spin-spin interactions in the solid. Redfield measured $T_{1\rho}$ for metals such as aluminium and copper as a function of the strength of the applied transverse RF field, thus performing the very first $R_{1\rho}$ RD measurements. $R_{1\rho}$ RD measurements in liquids were reported some four years later by Solomon in 1959[55] who tested theoretical expressions relating $R_{1\rho}$ to the rotational correlation time that were developed earlier by Winter *et al.*[56]. Solomon performed these $R_{1\rho}$ measurements in a manner similar to the pulsed methods used routinely nowadays. An adiabatic half passage was used to tilt the magnetization to the transverse plane, following which the spin-locking field was applied for a given time and switched off to measure the signal in the transverse plane. The variation of the signal amplitude with the time for which the spin-locking field was applied was used to obtain $R_{1\rho}$. An on-resonance RD profile was reported showing the dependence of $R_{1\rho}(^1\mathrm{H})$ on the applied spin-lock amplitude for the protons of formamide (Fig. 2A).

2.2. 1960–1970s: Applications to small molecules

In the early 1960s, Meiboom and colleagues realized that RD experiments could be used to characterize chemical exchange. Using on-resonance $R_{1\rho}(^1\mathrm{H})$[57] and CPMG(^{1}H)[58, 59] experiments, they estimated the rates of proton transfer in water. These experiments did not rely on the modulation of the chemical shift by the exchange process, but rather, on the modulation of the proton resonance frequency due to changes in scalar couplings and quadrupolar interactions as the protons exchanged between water molecules containing ^{16}O and ^{17}O. During the same period, approaches based on saturation transfer, which later were to form the basis for the CEST experiment, were used to investigate the kinetics of proton exchange between 2-hydroxy acetophenone and salicylaldehyde in 1963[24] and internal proton-transfer in acetylacetone in 1964[60].

RD measurements probing exchange contributions due to the modulation of chemical shifts soon followed with applications to small organic compounds. These landmark studies of conformational exchange in small molecules formed the basis for the modern RD applications to biomolecules. In an early application, Allerhand and Gutowsky used CPMG(^{1}H) experiments to characterize the hindered rotation of amide groups in dimethylcarbamyl chloride and *N,N* dimethyltrichloroacetamide[61] as well as chair-to-chair inter-conversion in cyclohexane[62] (Fig. 2B). Analogous $R_{1\rho}$ RD studies were conducted in the early 1970s by Morgan, Strange and colleagues[63]. The exchange rate (250–2000 s^{-1}) and difference in chemical shift between the exchanging axial and equatorial protons (20–25 Hz) deduced for the chair-to-chair interconversion of cyclohexane (Fig. 2B), assuming two-state exchange between equally populated states, were in good agreement with the values measured previously using CPMG[62]. Morgan, Strange and colleagues also demonstrated the feasibility of using on-resonance $R_{1\rho}$(^{31}P) and $R_{1\rho}$(^{1}H) to measure *J*-couplings and T_2 for halides of phosphorus[64] and hydrogen[65, 66], and also examined the impact of RF and B_0 field inhomogeneity on the accuracy of $R_{1\rho}$ measurements[67]. Other early applications included the determination of the activation energies for the rotation of amide groups in urea derivatives, based on the temperature dependence of $R_{1\rho}$[68]. This period also saw applications of saturation transfer to characterize conformational exchange in small molecules[69, 70], kinetics of proton exchange[71], and reaction rates[72].

2.3. 1970s–2000s: Applications to biomolecules

Applications of RD methods to biomolecules began to emerge in the early 1970s with initial studies focusing on measuring RD data on small substrates to characterize enzymesubstrate binding kinetics. In one of the earliest applications of $R_{1\rho}$ RD to the study of chemical exchange in biomolecules, Sykes[73] in 1969 measured on-resonance $R_{1\rho}$(^{19}F) RD on the trifluoroacetyl-phenylalanine substrate and thereby characterized its binding kinetics to the enzyme chymotrypsin (Fig. 2C). Not only was this the first measurement of $R_{1\rho}$ RD involving biological macromolecules, it was also the first measurement of exchange contributions to $R_{1\rho}$ arising from chemical shift modulation. It was shown that the rate constants for binding as well as the chemical shifts of the bound trifluoroacetyl-phenylalanine could be deduced from $R_{1\rho}$ RD measurements. In analogy to $R_{1\rho}$, the first biological application of CPMG RD involved characterizing the kinetics of N-fluoroacetyl-D-tryptophan binding to α-chymotrypsin using ^{19}F as a probe[74]. During the same period, ^{1}H CEST experiments were also applied to study the kinetics of trimethoprim binding to dihydrofolate reductase[75]. Many modern applications have continued to use RD NMR with great success to probe the kinetics of intermolecular association[76–79]. This period also saw the application of $R_{1\rho}$[80–82] and CPMG[83–85] experiments to measure T_2 for the purpose of characterizing fast picosecond-to-nanosecond timescale motions in proteins and nucleic acids.

During the 1970s and 80s, ^{1}H RD was used to study chemical exchange due to conformational changes in the biomolecules themselves, with initial applications to protein side chains and oligonucleotides. In one of the earliest applications, Williams *et al.* used ^{1}H CEST to measure the temperature-dependent kinetics of rotation of a tyrosine residue about the C^{β}-C^{γ} bond in ferrocytochrome C, and obtain the activation energy for the process[86].

$R_{1\rho}(^1H)$ RD experiments were also used to characterize backbone and side-chain conformational exchange in peptides[87–90]. This period also witnessed the introduction of ROESY experiments that relied on transverse cross relaxation in the presence of a spin-locking field for transferring magnetization between spins[91, 92]. The experiment was later extended to include spin-locking fields far off-resonance[93–95] and has been used to study conformational changes[96], reaction rates[97] and base opening[98] in the context of nucleic acids, in addition to investigating their hydration dynamics[99, 100]. The 1980s also saw the application of imino proton exchange methods by Gueron, Leroy, and co-workers, to study base pair opening in DNA duplexes[101, 102] and tetrads[103].

By the early 1990s, RD NMR had emerged as a technique for probing micro-to-millisecond timescale motions, bridging the gap between picosecond-to-nanosecond timescale motions accessible by T_1, T_2, and NOE measurements[104–106] and millisecond timescale motions detectable by T_2 measurements and line-shape analysis. Given the advances in hardware[107, 108], the stage was set for applications to measure chemical exchange in biomolecules, initially using ^1H probes and later ^{13}C and ^{15}N probes as well.

It may come as a surprise that early applications of RD to study conformational exchange in large biomolecules used $R_{1\rho}$ rather than CPMG, and that the first target molecules were DNA duplexes rather than proteins. Ikuta[109], James[110] and Frenkiel[111] measured onresonance $R_{1\rho}(^1H)$ RD for cytosine-H5, guanine-H8 and adenine-H2 and reported micro-tomillisecond timescale exchange in the DNA double helix (Fig. 2D). These early experiments did not provide the chemical shifts of the exchanging species, and as a consequence, it was not possible to deduce the identity of the ES. We now know that these very first observations of chemical exchange in DNA most likely represented transitions between Watson-Crick and Hoogsteen BPs, based on off-resonance $R_{1\rho}$ measurements performed a quarter century later[17, 112–117] (see Fig 2J). Analogous Hoogsteen transitions were characterized in G-G mismatches during the mid 1990s by Peck and colleagues[118] using $R_{1\rho}(^1H)$ RD measurements targeting base guanine-H8.

Following the introduction of methods for preparing $^{13}C/^{15}N$ labeled proteins in the late 1980s and 1990s (reviewed in Bolton *et al.*[119]) and the development of 2D methods for measuring heteronuclear spin-lattice R_1 (= $1/T_1$) and spin-spin R_2 (= $1/T_2$) relaxation rate constants[104, 120, 121], it became feasible to carry out detailed residue specific studies of conformational exchange in biomolecules. In an early application, Wuthrich *et al.*[122] used a 2D $R_{1\rho}(^{15}N)$ RD experiment developed by Wagner *et al.*[123] to probe the kinetics of backbone conformational changes in bovine pancreatic trypsin inhibitor (BPTI) (Fig. 2E). During the same period, Kay, Torchia, and Bax pioneered the 2D CPMG(^{15}N) experiment[104] to suppress chemical exchange contributions and allow the accurate measurement of residue specific T_2 values in proteins for studies of picosecond-to-nanosecond dynamics. Early applications of CPMG to measure T_2 frequently revealed micro-to-millisecond exchange contributions, but these were often not investigated further to obtain details regarding the underlying exchange process[124, 125]. This changed in 1994, when Arseniev *et al.* performed the first 2D ^{15}N CPMG RD measurement on a protein[126] by varying the delay between the hard 180° pulses. Millisecond timescale backbone motions in a fragment of bacteriorhodopsin were characterized and tentatively assigned to the

bending of the transmembrane alpha helices. Many studies appeared thereafter during the 1990s applying $R_{1\rho}$ and CPMG to study conformational exchange in a variety of proteins (reviewed by Loria *et al.*[22]). Other early applications included the use of CPMG(^{1}H) RD to investigate the dynamics of water molecules as they exchanged between the bulk and the hydration layer of proteins[127].

The development of methods for preparing ^{13}C/^{15}N labeled RNA[128] and DNA[129] during the late 1980s and early 1990s also opened the door for the application of heteronuclear 2D $R_{1\rho}$ experiments to nucleic acids, initially with a focus on measuring on-resonance $R_{1\rho}$(^{13}C). Using on-resonance adenine sugar $R_{1\rho}$(C1') RD measurements, Lancelot *et al.* in 1997[130] and Chattopadhyaya *et al.* in 2000[131] reported microsecond timescale exchange in a DNA duplex. While the nature of the exchange process was unknown, it again likely represented Watson Crick to Hoogsteen transitions[17, 112–117]. During the same period, Pardi and Hoogstraten performed some of the first $R_{1\rho}$ RD measurements on RNA, reporting microsecond timescale exchange in the lead-dependent ribozyme[132] and hammerhead ribozyme[133] based on aromatic base $R_{1\rho}$(^{13}C) measurements. From these measurements, k_{ex} as well as the product $p_{GS}p_{ES}\Delta\omega^2$ could be determined, where k_{ex} is the exchange rate (units s^{-1}), $\Delta\omega$ is the difference in chemical shift between the exchanging species (units rad s^{-1}), and p_{GS} and p_{ES} are the populations of the GS and ES, respectively. This period also saw application of CPMG(^{13}C) RD to RNA by Marion *et al.*, who estimated exchange contributions to transverse relaxation using random fractionally ^{13}C labeled samples to suppress homonuclear C-C scalar couplings[134].

This was followed by many studies employing $R_{1\rho}$(^{13}C) experiments to examine chemical exchange in RNA and DNA during the 2000s. For example, Butcher *et al.* characterized widespread chemical exchange in the U6-RNA stem loop containing a single nucleotide bulge[135]. The exchange was hypothesized to arise from the flipping out of a bulge nucleotide in a manner dependent on protonation of a flanking A-C mismatch (Fig. 2F). This was validated based on pH-dependent chemical shift measurements, providing a rare example in which structural features of nucleic acid ESs could be deduced and tested. Other studies exposed exchange on a microsecond timescale involving changes in sugar pucker in the GAAA tetraloop[136] as well as changes in exchange dynamics in RNA upon binding to proteins[137]. Subsequent studies by Varani *et al.* also revealed micro-to-millisecond timescale exchange related to motions of loop residues in RNA and G-C BPs in duplex DNA[138–140].

2.4. 2000s-present: Detailed characterization of chemical exchange in biomolecules

The 2000s witnessed key advances in methodology that improved the ability to characterize chemical exchange using NMR RD methods. CPMG(^{13}C and ^{15}N) experiments could not be used to study processes slower than ~2 ms due to difficulties associated with deconvoluting in-phase and anti-phase relaxation contributions during the relaxation period when using long interval periods between 180° pulses[141]. This drawback was addressed by the development of relaxation-compensated CPMG experiments by Palmer and Loria in 1999[142] that permitted the usage of 180° pulse trains with larger intervals by averaging the contributions of in-phase and anti-phase relaxation during the relaxation period. Another

limitation was that CPMG data could only be used to determine the magnitude of Δω, but not its sign. This prevented determination of the ES chemical shifts that later proved critical for their structural elucidation. This problem was addressed in 2002 when Kay *et al.*[143] introduced HSQC/HMQC methods for determining the sign of Δω, permitting for the first time complete characterization of an exchange process using CPMG based methods, for a mutant of T4 lysozyme. Other developments in CPMG experiments (reviewed in Palmer *et al.*[5]) soon followed, including the use of constant time relaxation periods[144, 145], double/multiple quantum based methods[146–148], extension to different types of spins in proteins[149, 150], and TROSY[151] based methods to extend applications to larger proteins[142, 152]. The first structural characterization of an ES was reported in 2004, when in a landmark study, Kay *et al.* reported the structure of a protein folding intermediate of a mutant Fyn SH3 domain, using chemical shifts obtained from CPMG(^{15}N) RD measurements[153] (Fig. 2G).

During the same time period, advances were also being made in the $R_{1\rho}$ experiment with specific application to proteins. Early $R_{1\rho}$ RD experiments[123, 154, 155] employed hard pulses to align the magnetization of all spins along their effective fields. This limited the experiment to relatively high spin-lock amplitudes (>1000 Hz), consequently leaving millisecond motions largely undetected. In addition, algebraic expressions relating $R_{1\rho}$ RD to the exchange parameters (p_{ES}, k_{ex}, Δω, R_1 and R_2) were only available for the fast exchange limit[63, 87, 156]. While this allowed estimation of k_{ex}, resolving p_{ES} and Δω was not possible; rather only the product $p_{ES}p_{GS}\Delta\omega^2$ could be determined. Finally, methods for suppressing dipole-dipole CSA cross correlated relaxation (DD/CSA)[157] had yet to be developed, and discrepancies were being reported for relaxation rates measured using $R_{1\rho}$ and CPMG[158, 159].

In the early 2000s, advances were made that addressed these limitations. In a milestone study, Palmer *et al.* in 2002[23] provided expressions for the exchange contribution to $R_{1\rho}$ outside of the fast exchange limit (Fig. 2H). These expressions showed that a complete thermodynamic and kinetic characterization of an exchange process including the sign of Δω was feasible based on off-resonance $R_{1\rho}$ RD data measured at a single static magnetic field. In 2005, Kay *et al.* introduced an $R_{1\rho}$ RD experiment that employed a selective excitation scheme developed by Bodenhausen and co-workers[160–162] to investigate exchange contributions at individual ^{15}N spins in a 1D manner[163]. In addition to permitting facile alignment of the magnetization along the effective field for a wide variety of offsets and spin-lock amplitudes, contributions from cross-correlated dipole-dipole/CSA relaxation[157] and evolution under J_{NH} scalar couplings could be optimally suppressed with the use of continuous-wave ^{1}H irradiation during the spin-lock period. This culminated in the first extraction of all exchange parameters using $R_{1\rho}$ measurements at a single magnetic field by Kay *et al.* in 2005[163] for a mutant of the Fyn SH3 domain, thus demonstrating the utility of the expressions developed earlier by Palmer *et al.*[23] (Fig. 2I).

These advances initially made for proteins were later integrated in 2009[21] into a pulse sequence employing low spin-lock amplitudes optimized for measuring $R_{1\rho}(^{13}C)$ for base (C6/C8) and sugar (C1′) spins in nucleic acids. This study demonstrated the feasibility of performing off-resonance $R_{1\rho}$ RD experiments on uniformly ^{13}C/^{15}N nucleic acids, which

could be prepared using commercially available $^{13}C/^{15}N$ labeled nucleotide triphosphates. This made it possible for the first time to extract all exchange parameters in nucleic acids, including the sign of Δω. By permitting the use of low spin-lock amplitudes, the experiment also made it possible to access slow millisecond timescale exchange in nucleic acids, given the challenges of applying CPMG(^{13}C) to uniformly $^{13}C/^{15}N$ labeled samples. This $R_{1\rho}$ experiment permitted more detailed studies of chemical exchange in nucleic acids, and when combined with methods for modulating conformational exchange using mutagenesis and chemical modifications (Section 7), it became possible to visualize the structural identity of the nucleic acid ESs, first in DNA[17] (Fig. 2J) and soon after in RNA[16]. The experiment was later extended to target base imino[112, 164] and amino[165] ^{15}N spins as well as sugar ^{13}C spins[117, 166], culminating in 3D structure determination of an ES in the DNA double helix, specifically the Hoogsteen BPs mentioned earlier[116, 117].

Five years following the application of low spin-lock off-resonance $R_{1\rho}$ to nucleic acids, and building on efforts that resurrected the CEST experiment to characterize chemical exchange in proteins[167–169], Zhang *et al.*[28, 170] demonstrated the utility of ^{13}C CEST for characterizing slow millisecond timescale chemical exchange in uniformly $^{13}C/^{15}N$ labeled RNA samples, as well as allowing direct access to structural and dynamic properties of ESs such as residual dipolar couplings (RDCs)[171, 172]. Like $R_{1\rho}$, the CEST experiment also allows the determination of all exchange parameters and has been widely applied in studies of nucleic acid dynamics[29–32]. Concurrently, significant advances were made in preparing RNA samples with selective labeling schemes, which further extended the domain of applicability of CPMG to nucleic acids[18, 136, 173–177]. With the $R_{1\rho}$, CEST, and CPMG methodologies in place, one is now in a much better position to characterize motions in DNA and RNA occurring on the microto-millisecond timescale and to examine their roles in gene expression and regulation.

Perhaps the most important lesson that can be drawn from this brief historical account is that RD methods have their roots in magnetic resonance studies that were not intended to characterize chemical exchange, but rather, flow from human curiosity. This underscores the importance of fostering basic science research in magnetic resonance even if clear applications are not obvious in the short run. Indeed, it is very likely the case that there are other NMR phenomena such as Hahn’s echo discovered many decades ago, that can be adapted to modern applications to biological problems. Our account also illustrates how important it was following the initial discovery of the RD methods to tightly integrate developments in hardware, sample labeling, theory, and pulse sequence design to make possible the modern quantitative applications to biomolecules.

3. Description of $R_{1\rho}$ relaxation dispersion using a vector model

RD experiments for studying equilibrium chemical exchange can be understood without recourse to a rigorous quantum mechanical description. To understand the $R_{1\rho}$ RD experiment, one needs to understand how exchange between a GS and an ES leads to dephasing of the observable bulk magnetization, and to what extent dephasing varies with the amplitude (ω_1, units rad s^{-1}) and offset frequency (Ω, units rad s^{-1}) of an applied spin-locking field, as well as the exchange parameters of interest, namely the fractional

population of the GS (p_{GS}) and ES (p_{ES}), the exchange rate (k_{ex}, units s^{-1}), and the difference between the chemical shifts of the GS and ES ($\Delta\omega = \omega_{0,ES} - \omega_{0,GS}$ and $\Delta\overline{\omega} = \overline{\omega}_{0,ES} - \overline{\omega}_{0,GS}$, where $\omega_{0,ES}$ and $\overline{\omega}_{0,ES}$, and $\omega_{0,GS}$ and $\overline{\omega}_{0,GS}$ are the Larmor frequencies, of the spin in the ES and GS, in units of rad s^{-1} and ppm respectively). In this section, we use a vector model to describe how two-state exchange leads to dephasing of the magnetization during an $R_{1\rho}$ RD experiment. The goal is to help the reader visualize and thereby better understand the $R_{1\rho}$ experiment. A mathematical treatment applicable to *n*-state exchange will be presented in Section 4.1. This section will ignore the influence of scalar couplings, the treatment of which requires a quantum-mechanical description based on the Liouville-von Neumann equation[178–180] or average Hamiltonian theory[181].

3.1. Free precession chemical exchange

We first consider the simplest case and examine how chemical exchange leads to dephasing of the magnetization under free precession, i.e., in the absence of a spin-locking field. We will find that similar mechanisms lead to dephasing of the magnetization in the presence of a spin-locking field during an $R_{1\rho}$ experiment. We consider conformational exchange between a major GS and a sparsely populated ES (Fig. 3A). We will ignore the effects of longitudinal and transverse relaxation, and consider a spin that has different chemical shifts in the GS and ES ($\omega_{0,GS} \neq \omega_{0,ES}$).

To understand how chemical exchange impacts the NMR spectrum, we first need to understand the stochastic nature of the exchange process as this ultimately dictates how it will dephase bulk magnetization. Two-state exchange can be described by forward (k_1) and backward (k_{-1}) rate constants (units s^{-1}):

$$GS \underset{k_{-1}}{\overset{k_1}{\rightleftharpoons}} ES \quad (1)$$

with the exchange rate $k_{ex} = k_1 + k_{-1}$ (units s^{-1}), which can be understood to be the rate constant at which the equilibrium state is restored following a perturbation that pushes the system away from equilibrium. Assuming transition-state theory, the rate constants are related to the free energies of activation according to the Eyring equation:

$$k_1 = \frac{\kappa k_B T}{h} \exp\left(\frac{-\Delta G_1^{\ddagger}}{RT}\right) \quad (2)$$

$$k_{-1} = \frac{\kappa k_B T}{h} \exp\left(\frac{-\Delta G_{-1}^{\ddagger}}{RT}\right) \quad (3)$$

where κ is the transmission coefficient describing the fraction of barrier crossing events that lead to the formation of the products from the reactants, R is the universal gas constant (units J K^{-1} mol^{-1}), k_B is the Boltzmann constant (units J K^{-1}), T is the temperature (units K), h is Planck's constant (units J s), and $\Delta G_1^{\ddagger}$ and $\Delta G_{-1}^{\ddagger}$ are free energies of activation (units J mol^{-1}) for the forward and backward reactions, respectively.

Importantly, molecules do not spend a fixed amount of time in either the GS or ES before interconverting (Fig. 3B). Rather, they spend variable amounts of time. A molecule may spend a short time visiting the ES on one occasion but spend a longer time on a second visit. Why is that the case? At the microscopic level, not all molecules are equal; rather they have free energies that follow a Boltzmann distribution $\exp\left(\frac{-\Delta G}{RT}\right)$ where ΔG is the free energy of a molecule relative to a reference state. The probability that a molecule has the energy required to cross a barrier $\Delta G^{\ddagger}$ will be proportional to $\exp\left(\frac{-\Delta G^{\ddagger}}{RT}\right)$. As a consequence, the dwell time (τ) molecules spend in conformation i follows an exponential distribution $\exp\left(\frac{-\tau}{<\tau_i>}\right)<\tau_i>^{-1}$ where $<\tau_i>$is the average dwell time or lifetime of the i^{th} state (Fig. 3C). Therefore, while we will often simply refer to the lifetime of the GS or ES, this actually represents an average over what in reality is an exponential distribution of dwell times. The lifetimes of the GS $<\tau_{GS}>$and ES $<\tau_{ES}>$ are given by reciprocals of k_1 and k_{-1}, respectively:

$$<\tau_{GS}> = 1/k_1 \quad (4)$$

$$<\tau_{ES}> = 1/k_{-1} \quad (5)$$

We first consider a hypothetical scenario where a molecule exists in two distinct conformations GS and ES that do not interconvert. The transverse magnetizations M_{GS} and M_{ES} are initially aligned along the x-axis after application of a $90°_y$ pulse and will experience an effective field ($\boldsymbol{B_{eff}}$, bold refers to a vector) equal to $\boldsymbol{B_0}$ aligned along the z-axis of the laboratory frame. Consequently, M_{GS} and M_{ES} will precess around $\boldsymbol{B_0}$ with frequencies $\omega_{0,GS}$ and $\omega_{0,ES}$, respectively, and the NMR spectrum consists of two lines centered at frequencies $\omega_{0,GS}$ and $\omega 0,_{ES}$.

It is instructive to examine the behavior of the magnetization in a rotating frame, as this will also prove important when describing the dephasing of the magnetization during an $R_{1\rho}$ experiment (Section 3.2). In a rotating frame precessing at a frequency ω_{rf} (units rad s^{-1}), M_{GS} and M_{ES} precess with offset frequencies Ω_{GS} and Ω_{ES} (units rad s^{-1}) respectively, around the z axis:

$$\Omega_{GS} = \omega_{0,GS} - \omega_{rf} \quad (6)$$

$$\Omega_{ES} = \omega_{0,ES} - \omega_{rf} \quad (7)$$

The magnitude of the effective fields experienced by the GS ($B_{\text{eff,GS}}$) and the ES ($B_{\text{eff,ES}}$) is reduced from B_0 to ΔB_{GS} and ΔB_{ES} (units Tesla), respectively:

$$B_{eff,GS} = \Delta B_{GS} = \frac{\Omega_{GS}}{\gamma} \quad (8)$$

$$B_{eff,ES} = \Delta B_{ES} = \frac{\Omega_{ES}}{\gamma} \quad (9)$$

where γ is the gyromagnetic ratio (units rad s^{-1} $Tesla^{-1}$).

We now examine how chemical exchange affects M_{GS} and M_{ES}, and the NMR spectrum. The exchange contribution will vary depending on the NMR chemical shift timescale, defined as the ratio between k_{ex} and $\Delta\omega$ ($k_{ex}/\Delta\omega$). Under the slow exchange limit ($k_{ex} << \Delta\omega$), the GS and ES are long-lived and two discrete resonances are observed in the NMR spectrum centered at $\omega_{0,GS}$ and $\omega_{0,ES}$ (Fig. 4A). However, compared to the case in which the GS and ES do not interconvert, the resonances are broadened by the exchange process. This is because exchange leads to the dephasing of the magnetization.

To visualize dephasing of M_{GS}, initially aligned along the x-axis, we move into a rotating frame precessing at a frequency of $\omega_{0,GS}$. In this frame, the magnetization of the GS spins is stationary ($\Omega_{GS} = 0$) while that of the ES spins precesses with frequency $\Delta\omega$ (Fig. 4B). The magnetization belonging to a GS spin will be stationary for the duration of the dwell time τ_{GS}. When the molecule transforms into the ES, the magnetization associated with the spin will start to precess with frequency $\Omega_{ES} = \Delta\omega$ for duration τ_{ES}, leading to a change in phase angle given by $\tau_{ES}\Delta\omega$ (Fig. 4B). The precession then stops again for some duration τ_{GS} when the molecule switches back to the GS, and so on. Depending on the exchange rate, many such transitions may occur during acquisition. As spins within the same molecule or across molecules will spend varying amounts of time in the GS or ES, the GS spins will be associated with different phase angles leading to dephasing of the bulk GS magnetization along the x-axis (M_{GSx}) (Fig. 4C). This causes M_{GSx} to decrease exponentially over time with the rate constant given by $R_{ex,GS}$ (Fig. 4D). Why is the decay exponential? This again goes back to the exponential distribution of the dwell times τ_{GS} and τ_{ES} (Fig. 5), which causes the probability that the magnetization of the different spins are aligned to decrease exponentially with time. Chemical exchange leads to a line-broadening contribution given by $R_{ex,GS}/\pi$ to the GS resonance in addition to the linebroadening due to intrinsic transverse relaxation ($R_{2,GS}/\pi$). Put alternatively, $R_{ex,GS}$ denotes the contribution to transverse relaxation of the GS resonance due to chemical exchange, and is dependent on the exchange parameters p_{ES}, k_{ex} and $\Delta\omega$.

In an analogous manner, the dephasing of M_{ES} can be visualized by moving into a rotating frame precessing at $\omega_{0,ES}$. In this frame, the ES magnetization is stationary ($\Omega_{ES} = 0$) but will much more quickly transform into the GS and start to precess with frequency $\Omega_{GS} = -\Delta\omega$, typically for a longer time relative to the GS when it transforms to the ES. As a result, the ES bulk magnetization experiences a greater degree of dephasing and the ES resonance experiences a greater degree of line-broadening as compared to the GS resonance, i.e., $R_{ex,ES} > R_{ex,GS}$.

Algebraic expressions for $R_{ex,GS}$ and $R_{ex,ES}$ at the slow exchange limit ($k_{ex} << \Delta\omega$) can be obtained by solving the B-M equations under free precession conditions (Section 4.1)[13, 14, 22]:

$$R_{ex,GS} = p_{ES}k_{ex} = k_1 \quad (10)$$

$$R_{ex,ES} = p_{GS}k_{ex} = k_{-1} \quad (11)$$

$$R_{ex,GS} + R_{ex,ES} = k_{ex} \quad (12)$$

In the slow exchange limit, $R_{ex,ES} > R_{ex,GS}$ and are equal to the backward and forward rate constants, respectively. In addition, increasing k_{ex} increases R_{ex} because this increases the frequency of transitions between the GS and ES. Furthermore, R_{ex} is independent of $\Delta\omega$ (valid for $k_{ex}/\Delta\omega \sim< 0.2$, Fig. 6) but does depend on p_{ES}. For $k_{ex}/\Delta\omega \sim< 0.2$, changing $\Delta\omega$ for a fixed k_{ex} does not significantly change the NMR chemical shift timescale and therefore the R_{ex} contribution. However, it should be noted that the NMR timescale can vary in the presence of a spin-locking field during the $R_{1\rho}$ experiment[13, 182]. Consequently, although R_{ex} is independent of $\Delta\omega$ in general under slow exchange (Fig. 6), this will not necessarily be the case during the $R_{1\rho}$ experiment (see Section 6.2). The observed transverse relaxation rate ($R_{2,obs}$) is given by the sum of contributions due to intrinsic relaxation ($R_{2,GS}$ and $R_{2,ES}$) and due to chemical exchange ($R_{ex,GS}$ and $R_{ex,ES}$):

$$R_{2,obs,GS} = R_{2,GS} + R_{ex,GS} = R_{2,GS} + p_{ES}k_{ex} = R_{2,GS} + k_1 \quad (13)$$

$$R_{2,obs,ES} = R_{2,ES} + R_{ex,ES} = R_{2,ES} + p_{GS}k_{ex} = R_{2,ES} + k_{-1} \quad (14)$$

As k_{ex} increases, R_{ex} continues to increase in the slow exchange regime, which can be defined as $k_{ex}/\Delta\omega < 0.2$. Under slow exchange, the observed resonance frequencies for the GS and ES are to a good approximation given by $\omega_{0,GS}$ and $\omega_{0,ES}$, respectively. Increasing k_{ex} further moves the system into the intermediate exchange regime, which can be defined as

$0.2 < k_{ex}/\Delta\omega < 2$ (Fig. 4A). The broadened GS and ES resonances now begin to shift toward one another until they coalesce when $k_{ex} \sim \Delta\omega$, at a frequency ($\omega_{0,OBS}$) distinct from the populationweighted average of $\omega_{0,GS}$ and $\omega_{0,ES}$ ($\omega_{0,AVG} = p_{GS}\omega_{0,GS} + p_{ES}\omega_{0,ES}$). At coalescence, the line broadening is maximum. This is because the GS-ES transition frequency is high, while $<\tau_{GS}>$ and $<\tau_{ES}>$ are sufficiently long to cause substantial dephasing of the magnetization. The exchange contribution can again be visualized by moving into a rotating frame precessing at the frequency $\omega_{0,OBS}$. In this frame, both the GS and ES magnetizations undergo precession, resulting in dephasing of the bulk magnetization corresponding to the observed resonance. In contrast to the slow exchange limit, B-M simulations indicate that R_{ex} depends on $\Delta\omega$ in the intermediate exchange regime[14, 22].

As k_{ex} increases further, the broadened resonance begins to shift and sharpen, and the system moves into the fast exchange regime ($k_{ex}/\Delta\omega > 2$) (Fig. 4A). Under these conditions, the observed resonance frequency $\omega_{0,OBS}$ is to a good approximation given by the populationweighted average $\omega_{0,AVG}$. The exchange contribution can again be visualized by moving into a rotating frame precessing at frequency $\omega_{0,AVG}$ (Fig. 4E), in which exchange results in dephasing of the bulk magnetization corresponding to the AVG resonance. Expressions for the exchange contribution ($R_{ex,AVG}$) to the observed relaxation rate ($R_{2,obs,AVE}$) at the fast exchange limit ($k_{ex} >> \Delta\omega$) can be obtained by solving the B-M equations (Section 4.1) and are given by[13]:

$$R_{2,obs,AVG} = R_{2,AVG} + R_{ex,AVG} = \left(p_{GS}R_{2,GS} + p_{ES}R_{2,ES}\right) + p_{GS}p_{ES}\Delta\omega^2/k_{ex} \quad (15)$$

As in slow exchange, R_{ex} depends on p_{ES} under fast exchange. However, in contrast to slow exchange, decreasing k_{ex} increases R_{ex} under fast exchange, as spins spend longer periods of time in the GS and/or ES and conversely, increasing k_{ex} decreases R_{ex} as $<\tau_{GS}>$ and/or $<\tau_{ES}>$ decrease. Moreover, R_{ex} is now proportional to $\Delta\omega^2$. Note that the appearance of a single resonance in the NMR spectrum does not imply that the system is in fast exchange; the system could be in intermediate exchange or even under slow exchange since the larger R_{ex} contribution to a minor ES resonance could render it undetectable[22, 183].

3.2. $R_{1\rho}$ in the absence of chemical exchange

While NMR line shapes carry rich information about chemical exchange[184], they cannot be used to reliably determine all exchange parameters of interest. The $R_{1\rho}$ experiment, and RD experiments in general, provide an alternative means to extract this information. These experiments modulate the effective field experienced by a given spin, thereby enhancing the sensitivity to the exchange parameters.

The $R_{1\rho}$ experiment entails the application of a continuous RF spin-locking $\boldsymbol{B_1}$ field along the x or y-axis, transverse to the static $\boldsymbol{B_0}$ field. The purpose of the spin-locking field is to control $\boldsymbol{B_{eff,GS}}$ and $\boldsymbol{B_{eff,ES}}$, and therefore, the extent to which the bulk magnetization is dephased due to chemical exchange. In this section, we will ignore chemical exchange and first examine how the magnetization is spin-locked, how changing the spin-lock parameters

alters the effective field, and lay out the theoretical basis for describing the $R_{1\rho}$ experiment using a vector model.

Let us first examine how $\boldsymbol{B_1}$ applied along the x-axis affects $\boldsymbol{B_{eff}}$ experienced by a given spin. $\boldsymbol{B_1}$ is a linearly oscillating field with amplitude $2B_1$ (units Tesla) and frequency ω_{rf} (units rad s^{-1}; positive/negative values refer to clockwise/anti-clockwise rotations, respectively), both of which are specified by the user (Fig. 7A):

$$\boldsymbol{B_1} = 2B_1\cos(\omega_{rf}t)\hat{\boldsymbol{x}} \quad (16)$$

The linearly oscillating $\boldsymbol{B_1}$ field can be decomposed into two rotating fields $\boldsymbol{B_1}^+$ and $\boldsymbol{B_1}^-$ each with an amplitude B_1 rotating in opposite directions in the transverse plane with frequencies ω_{rf} (clockwise) and $-\omega_{rf}$ (counterclockwise) (Fig. 7A):

$$\boldsymbol{B_1} = \boldsymbol{B_1^+} + \boldsymbol{B_1^-} \quad (17)$$

$$\boldsymbol{B_1^+} = B_1\cos(\omega_{rf}t)\hat{\boldsymbol{x}} - B_1\sin(\omega_{rf}t)\hat{\boldsymbol{y}} \quad (18)$$

$$\boldsymbol{B_1^-} = B_1\cos(\omega_{rf}t)\hat{\boldsymbol{x}} + B_1\sin(\omega_{rf}t)\hat{\boldsymbol{y}} \quad (19)$$

The treatment of $\boldsymbol{B_1}$ is simplified by working in a frame rotating with frequency $+\omega_{rf}$ (Fig. 7B). In this frame, the vector $\boldsymbol{B_1}^+$ is aligned along the x-axis and has a length B_1, while $\boldsymbol{B_1}^-$ rotates at $2\omega_{rf}$ and can be ignored. The magnetization precesses with an offset frequency Ω around the zaxis and the spin experiences a reduced field ΔB along the z-axis as described in Section 3.1. $\boldsymbol{B_{eff}}$ experienced by an ensemble of spins with an offset Ω is given by the vector sum:

$$\boldsymbol{B_{eff}} = \boldsymbol{B_1} + \boldsymbol{\Delta B} \quad (20)$$

It is common practice to express $\boldsymbol{B_{eff}}$, $\boldsymbol{B_1}$, and $\boldsymbol{\Delta B}$ in terms of the precession frequency $\boldsymbol{\omega}$ (units rad s^{-1}) of the magnetization around the effective field:

$$\boldsymbol{\omega} = \gamma \boldsymbol{B} \quad (21)$$

$$\omega = \gamma B \quad (22)$$

Using ω is useful because dephasing of the magnetization due to chemical exchange during the $R_{1\rho}$ experiment is governed by the frequencies of precession. For the remainder of the review, we will replace the vector $\boldsymbol{B}$ and its magnitude B with $\boldsymbol{\omega}$ and ω, respectively:

$$\boldsymbol{\omega_1} = \gamma \boldsymbol{B_1} \quad (23)$$

$$\omega_1 = \gamma B_1 \quad (24)$$

$$\boldsymbol{\Omega} = \boldsymbol{\omega_0} - \boldsymbol{\omega_{rf}} = \gamma \boldsymbol{\Delta B} \quad (25)$$

$$\Omega = \omega_0 - \omega_{\mathrm{rf}} = \gamma \Delta B \quad (26)$$

$$\boldsymbol{\omega_{eff}} = \boldsymbol{\Omega} + \boldsymbol{\omega_1} \quad (27)$$

$$\omega_{\mathrm{eff}} = \left(\Omega^2 + \omega_1^2\right)^{1/2} \quad (28)$$

The applied $\boldsymbol{\omega_1}$ field will change both the orientation and the magnitude of the effective field $\boldsymbol{\omega_{eff}}$ experienced by a spin in a manner dependent on both $\boldsymbol{\Omega}$ and $\boldsymbol{\omega_1}$ as shown in Fig. 7C. For example, when $\boldsymbol{\omega_1}$ is applied on resonance ($\omega_{rf} = \omega_0$), $\boldsymbol{\Omega} = 0$, $\boldsymbol{\omega_{eff}} = \boldsymbol{\omega_1}$ and $\boldsymbol{\omega_{eff}}$ is aligned along the x-axis (Fig. 7C). If on the other hand ω_1 is applied off-resonance ($\omega_{rf} \neq \omega_0$), $\boldsymbol{\Omega} \neq 0$, $\boldsymbol{\omega_{eff}} = \boldsymbol{\omega_1} + \boldsymbol{\Omega}$, and $\boldsymbol{\omega_{eff}}$ is no longer in the transverse plane but is tilted away from the z-axis by an angle θ (units rad) that depends on both ω_1 and Ω (Fig. 7C):

$$\theta = tan^{-1}\left(\frac{\omega_1}{\Omega}\right) \quad (29)$$

Figure 8 shows additional examples of how changing ω_1 or Ω (through changes in ω_{rf}) changes both the amplitude and orientation of $\boldsymbol{\omega_{eff}}$. In principle, all possible orientations and amplitudes of $\boldsymbol{\omega_{eff}}$ can be realized experimentally by a suitable choice of ω_1 and Ω. As $R_{1\rho}$ experiments are most sensitive to an exchange process when $k_{ex} \sim \omega_{eff}$, the experimentally accessible effective fields define the detection limit of the experiment, as elaborated in Section 4.2.1.

During the $R_{1\rho}$ experiment, $\boldsymbol{\omega_1}$ is applied immediately after the magnetization of interest has been aligned along z′, the direction of $\boldsymbol{\omega_{eff}}$, using an appropriate preparatory pulse as described in Section 5.2 (Fig. 9). In the absence of $\boldsymbol{\omega_1}$, the magnetization precesses around $\boldsymbol{B_0}$ with frequency $\boldsymbol{\omega_0}$. However, in the presence of $\boldsymbol{\omega_1}$, precession is eliminated, and the magnetization is 'spin-locked' along $\boldsymbol{\omega_{eff}}$, although its magnitude is subject to decay due to relaxation (Fig. 9). It is important to note that the magnetization remains spin-locked along $\boldsymbol{\omega_{eff}}$ as long as R_2 and R_1 are both smaller than ω_1 and Ω. If those conditions are not met, the magnetization can veer off and deviate from $\boldsymbol{\omega_{eff}}$ (Fig. 10).

The $R_{1\rho}$ experiment measures the rate of relaxation of the magnetization that is spinlocked along $\boldsymbol{\omega_{eff}}$ (Fig. 9). In the absence of chemical exchange, the relaxation will be governed by R_1 and R_2[13]. To obtain expressions relating $R_{1\rho}$ to R_1 and R_2, we use the Bloch equations[46], which model the behavior of the magnetization in the rotating frame of the spin locking field:

$$\frac{d}{dt}\begin{pmatrix} M_x \\ M_y \\ M_z \end{pmatrix} = \begin{pmatrix} -R_2 & -\Omega & 0 \\ \Omega & -R_2 & -\omega_1 \\ 0 & \omega_1 & -R_1 \end{pmatrix}\begin{pmatrix} M_x \\ M_y \\ M_z \end{pmatrix} + R_1\begin{pmatrix} 0 \\ 0 \\ M_{z,eq} \end{pmatrix} \quad (30)$$

where M_x, M_y and M_z are the x, y and z components of the bulk magnetization respectively and $M_{z,eq}$ refers to the equilibrium z magnetization. The diagonal and $M_{z,eq}$ terms describe the influence of relaxation while off-diagonal terms describe interchange between M_x and M_y, and M_y and M_z, due to precession around $\boldsymbol{\Omega}$/z-axis and $\boldsymbol{\omega_1}$/x-axis, respectively, in the absence of chemical exchange and spin-locking field. The Bloch equations assume that the interactions between spins are independent of, and significantly weaker than, the interactions between the spins and the external field, i.e., $\tau_c << T_2$, where τ_c is the rotational correlation time[53]. This condition is readily satisfied for biomacromolecules in solution where $\tau_c \sim 5$–30 ns and $T_2 \sim 5 - 200$ ms.

Moving into a doubly rotating frame in which the z-axis is aligned along z′ (Fig. 9) simplifies the description of the magnetization and allows derivation of a key expression for $R_{1\rho}$[123, 185–188]. This is achieved through rotation of the coordinate frame (in the rotating frame of the spin-locking field) around the y-axis by the angle θ. This second rotation has the effect of nullifying rotations about $\boldsymbol{\omega_{eff}}$ at a frequency of ω_{eff}. The Bloch equations in the doubly rotating frame are given by:

$$\frac{d}{dt}\begin{pmatrix} M'_x \\ M'_y \\ M'_z \end{pmatrix} = \begin{pmatrix} -R_2 cos^2(\theta) - R_1 sin^2(\theta) & -\left(\Omega^2 + \omega_1^2\right)^{1/2} & (R_1 - R_2) sin(\theta)\cos(\theta) \\ \left(\Omega^2 + \omega_1^2\right)^{1/2} & -R_2 & 0 \\ (R_1 - R_2) sin(\theta)\cos(\theta) & 0 & -R_2 cos^2(\theta) - R_1 sin^2(\theta) \end{pmatrix} \begin{pmatrix} M'_x \\ M'_y \\ M'_z \end{pmatrix} \quad (31)$$

$$+ R_1 \begin{pmatrix} -sin(\theta) M_{z,eq} \\ 0 \\ cos(\theta) M_{z,eq} \end{pmatrix}$$

where M_x', M_y' and M_z' are the components of the magnetization in the doubly rotated frame. M_x' and M_y' are perpendicular to $\boldsymbol{\omega_{eff}}$, while M_z' is oriented along $\boldsymbol{\omega_{eff}}$. Although algebraic expressions for M_z' are complicated in the general case, one can make the simplifying assumption[187] $\omega_1 \gg (R_1 - R_2) sin(\theta) cos(\theta)$ which is valid under most experimental conditions. In general, rapid interconversion between the M_x' and M_y' components of the magnetization due to the $\left(\Omega^2 + \omega_1^2\right)^{1/2}$ term averages the cross-relaxation term $(R_1 - R_2) sin(\theta) cos(\theta)$ between M_x' and M_z' to zero[187]. The evolution of M_x' and M_y', and M_z' are uncoupled and M_z' decays mono-exponentially with a rate constant $R_{1\rho}$ given by a weighted sum of R_1 and R_2:

$$M'_Z = M'_Z(0) \exp\left(-R_{1\rho} t\right) \quad (32)$$

$$R_{1\rho} = R_1 \, cos^2\theta + R_2 sin^2\theta \quad (33)$$

Thus, rotating the coordinate frame introduces contributions to decay along $\boldsymbol{\omega_{eff}}$ due to longitudinal and transverse relaxation to variable extents[13], depending on the orientation (tilt angle) of $\boldsymbol{\omega_{eff}}$. The relative weights of R_1 ($cos^2\theta$) and R_2 ($sin^2\theta$) can be understood as corresponding to their fractional contributions to the length of a unit vector oriented along $\boldsymbol{\omega_{eff}}$. The above expression shows that in the absence of chemical exchange, $R_{1\rho}$ does not provide any information beyond that which can be obtained from measuring R_1 and R_2.

The above expressions also lay the basis for the vector model that will be used to describe the $R_{1\rho}$ experiment in subsequent sections. Setting R_1 and R_2 to 0, the B-M equations in the doubly rotating frame reduce to:

$$\frac{dM'_x}{dt} = -\left(\Omega^2 + \omega_1^2\right)^{1/2} M'_y \quad (34)$$

$$\frac{dM'_y}{dt} = \left(\Omega^2 + \omega_1^2\right)^{1/2} M'_x \quad (35)$$

$$\frac{dM'_z}{dt} = 0 \quad (36)$$

From above equations, in the absence of relaxation M_x' and M_y' vary sinusoidally with time, while M_z' stays constant. Therefore, if the magnetization is initially aligned along $\boldsymbol{\omega_{eff}}$, $M_x'(0) = 0$ and $M_y'(0) = 0$, M_z' does not change with time while M_x' and M_y' remain zero; the magnetization is always aligned along $\boldsymbol{\omega_{eff}}$ and is spin-locked. In contrast, the magnetization tilted away from $\boldsymbol{\omega_{eff}}$ ($M_x'(0) \neq 0$ or $M_y'(0) \neq 0$) will precess around $\boldsymbol{\omega_{eff}}$ on the surface of a cone with a constant amplitude of $M_z'(0)$ and with precession frequency $\omega_{eff} = \left(\Omega^2 + \omega_1^2\right)^{1/2}$. Precession of the GS and ES magnetizations around their respective effective fields forms the basis for the vector model, which will be used to describe the R_{ex} contribution to $R_{1\rho}$.

3.3. Dephasing of magnetization during $R_{1\rho}$

We now examine how chemical exchange leads to dephasing of the magnetization in the rotating frame during an $R_{1\rho}$ experiment. For $\Delta\omega \neq 0$, the GS and ES will be associated with effective fields $\boldsymbol{\omega_{eff,GS}}$ and $\boldsymbol{\omega_{eff,ES}}$ respectively, in the rotating frame of $\boldsymbol{\omega_1}$ (Fig. 11A):

$$\boldsymbol{\omega}_{eff,GS} = \boldsymbol{\omega_1} + \boldsymbol{\Omega}_{GS} \quad (37)$$

$$\omega_{eff,GS} = \left(\omega_1^2 + \Omega_{GS}^2\right)^{1/2} \quad (38)$$

$$\boldsymbol{\omega}_{eff,ES} = \boldsymbol{\omega_1} + \boldsymbol{\Omega}_{ES} \quad (39)$$

$$\omega_{eff,ES} = \left(\omega_1^2 + \Omega_{ES}^2\right)^{1/2} \quad (40)$$

where the offsets Ω_{GS} and Ω_{ES} are defined in Section 3.1. We see that in the presence of 2-state chemical exchange between GS and ES, one must consider two non-parallel effective fields $\boldsymbol{\omega_{eff,GS}}$ and $\boldsymbol{\omega_{eff,ES}}$ that have different amplitudes, and around which the GS and ES magnetization vectors precess (Fig 11A). For *n*-state chemical exchange with *n* unique

chemical shifts, there would be one effective field for each of the *n* states (Fig. 11A). As described below, the dephasing of the magnetization during $R_{1\rho}$ is analogous to that in free precession, the major difference being that the axes of rotation for the GS and ES magnetization are different.

For intermediate and fast exchange, it is useful to define an average effective field $\boldsymbol{\omega}_{\mathbf{eff,AVG}}$ corresponding to $\omega_{0,\mathrm{AVG}}$:

$$\boldsymbol{\omega}_{eff,AVG} = \boldsymbol{\omega}_{\mathbf{1}} + \boldsymbol{\Omega}_{AVG} \quad (41)$$

$$\boldsymbol{\Omega}_{AVG} = \Omega_{AVG}\hat{z} \quad (42)$$

$$\Omega_{AVG} = \omega_{0,AVG} - \omega_{rf} = \left(p_{GS}\omega_{0,GS} + p_{ES}\omega_{0,ES}\right) - \omega_{rf} \quad (43)$$

In the selective 1D $R_{1\rho}$ experiments reviewed here in Section 5.2, both M_{GS} and M_{ES} are initially aligned along an effective field $\boldsymbol{\omega}_{\mathbf{eff,OBS}}$ before the application of the spin-locking field, which depends on ω_1 and $\Omega = \omega_{0,\mathrm{OBS}} - \omega_{\mathrm{rf}}$, where ω_{OBS} corresponds to the GS resonance frequency ($\omega_{0,\mathrm{OBS}} = \omega_{0,\mathrm{GS}}$) in the case of slow exchange or to the average resonance frequency ($\omega_{0,\mathrm{OBS}} = \omega_{0,\mathrm{AVG}}$) in the case of fast exchange (Fig. 11B). In general, simulations indicate that for intermediate to fast exchange ($0.1 < k_{ex}/\Delta\omega < 5$) and low p_{ES} (< 10%), alignment along $\boldsymbol{\omega}_{\mathbf{eff,AVG}}$ is a valid approximation and does not appreciably influence the RD profiles. However, deviations can arise particularly for high p_{ES} (> 10%)(Section 6.1).

Now let us examine how the magnetization is dephased due to exchange in the rotating frame in the presence of the spin-locking field. M_{GS} and M_{ES} are initially aligned along $\boldsymbol{\omega}_{\mathbf{eff,OBS}}$ and precess around $\boldsymbol{\omega}_{\mathbf{eff,GS}}$ and $\boldsymbol{\omega}_{\mathbf{eff,ES}}$ with frequencies $\omega_{\mathrm{eff,GS}}$ and $\omega_{\mathrm{eff,ES}}$, respectively (Fig. 11C). When a GS spin switches to the ES, its associated magnetization starts to precess around $\boldsymbol{\omega}_{\mathbf{eff,ES}}$ with frequency $\omega_{\mathrm{eff,ES}}$. When the molecule switches back to the GS, the magnetization associated with the spin starts again to precess around $\boldsymbol{\omega}_{\mathbf{eff,GS}}$ with frequency $\omega_{\mathrm{eff,GS}}$ and so on. Once again, because molecules spend varying amounts of time in the GS precessing around $\boldsymbol{\omega}_{\mathbf{eff,GS}}$ or in the ES precessing around $\boldsymbol{\omega}_{\mathbf{eff,ES}}$, exchange causes dephasing of the bulk magnetization (Fig. 11C) in a manner analogous to free precession in the absence of a spinlocking field (Fig. 4C). Here, $\boldsymbol{\omega}_{\mathbf{eff,GS}}$ and $\boldsymbol{\omega}_{\mathbf{eff,ES}}$ acts as 'dephasers' that scramble or randomize the orientation of M_{GS} and M_{ES}. Unlike free precession, in which the magnetization remains transverse, the exchange in this case results in magnetization that is arranged in a 3D "bouquet", which fans out exponentially with time (Fig. 11C). As in free precession, the exchange causes the projection of the bulk magnetization onto the vector $\boldsymbol{\omega}_{\mathbf{eff,OBS}}$ to decay exponentially with time resulting in an R_{ex} contribution to $R_{1\rho}$. The $R_{1\rho}$ experiment entails measuring the exponential decay of the

magnetization along $\boldsymbol{\omega}_{\mathbf{eff,OBS}}$ as a function of time, from which R_{ex} can be deduced. The $R_{2\rho}$ experiment measures the decay of M_x'/M_y' orthogonal to $\boldsymbol{\omega}_{\mathbf{eff,OBS}}$[13, 182].

The exponential decay of the magnetization associated with a single 3D bouquet provides a single $R_{1\rho}$ value that is not sufficient to extract all exchange parameters of interest. Thus, additional data is needed. This is accomplished by changing the scramblers $\boldsymbol{\omega}_{\mathbf{eff,GS}}$ and $\boldsymbol{\omega}_{\mathbf{eff,ES}}$ by changing the spin-lock parameters ω_1 and Ω (via changes in ω_{rf}). This changes the extent of dephasing of the magnetization, the resulting magnetization bouquets and the associated R_{ex} contributions, in a manner that depends on the exchange parameters, providing a means for their determination. Experiments in which the carrier is on-resonance and ω_1 is varied are referred to as "on-resonance" $R_{1\rho}$ experiments, while those that vary both ω_1 and Ω are referred to as "off-resonance" $R_{1\rho}$ experiments. The validity of the vector description of the $R_{1\rho}$ experiment can be verified through comparison with numerical solutions to the B-M equations (Fig. 12).

It is interesting to ask whether the net magnetization resulting from the vector sum over the bouquet remains perfectly aligned along $\boldsymbol{\omega}_{\mathbf{eff,OBS}}$. The answer depends on the timescale for chemical exchange as defined under free precession conditions. For fast exchange, the net magnetization as well as M_{GS} and M_{ES} are aligned along $\boldsymbol{\omega}_{\mathbf{eff,AVG}}$ (Fig. 13A). In contrast, under slow exchange conditions, M_{ES} can deviate from its initial alignment along $\boldsymbol{\omega}_{\mathbf{eff,GS}}$ towards $\boldsymbol{\omega}_{\mathbf{eff,ES}}$ while M_{GS} remains along $\boldsymbol{\omega}_{\mathbf{eff,GS}}$, causing the net magnetization to deviate towards $\boldsymbol{\omega}_{\mathbf{eff,AVG}}$ (Fig. 13B). This deviation of the net magnetization is proportional to p_{ES} and $\Delta\omega$. Even when the net magnetization is not along $\boldsymbol{\omega}_{\mathbf{eff,GS}}$ under slow exchange, the decay of the component along $\boldsymbol{\omega}_{\mathbf{eff,GS}}$ can still be mono-exponential (Fig. 13B). Note that the above statements are only valid under conditions when the relaxation rates R_1 and R_2 are smaller than ω_1 and Ω, as discussed in Section 3.2.

3.4. On-resonance $R_{1\rho}$

While off-resonance $R_{1\rho}$ experiments provide the best means for characterizing exchange as they afford the maximal amount of data, on-resonance experiments are often performed initially, typically to screen spins for the presence of chemical exchange. We review this simpler on-resonance $R_{1\rho}$ experiment and then later move to the more general offresonance $R_{1\rho}$ experiments.

In the on-resonance experiment, $\boldsymbol{\Omega} = 0$, $\boldsymbol{\omega}_{\mathbf{eff}} = \boldsymbol{\omega}_{\mathbf{1}}$, and R_{ex} simply adds to R_2 in a manner analogous to free precession (Section 3.1)[23, 63, 87, 156, 189]:

$$R_{1\rho} = R_2 + R_{ex}(\omega_1) \quad (44)$$

where R_2 is assumed to be the population-weighted average of $R_{2,GS}$ and $R_{2,ES}$, i.e., $R_2 = p_{GS}R_{2,GS} + p_{ES}R_{2,ES}$, which is valid for $|R_{2,GS} - R_{2,ES}| << k_{ex}$[13, 190]. It is also assumed that R_{ex} and R_2 are not correlated, which is a reasonable approximation given that they report on dynamics occurring on different timescales (i.e., $\tau_c << 1/k_{ex}$)[13, 45]. It is also assumed that $\tau_c << T_2$ as described in Section 3.2, $k_{ex} < \omega_{GS,0}$ and $k_{ex} < \omega_{ES,0}$[191], and

that the decay of the magnetization is mono-exponential; deviations from mono-exponential behavior can arise under slow exchange conditions with high p_{ES}[23](Section 4.2).

Setting $R_1 = R_2 = 0$, $R_{1\rho} = R_{ex}$, a vector description can be used to model how R_{ex} varies with ω_1. Increasing ω_1 decreases the angle φ between $\boldsymbol{\omega}_{\mathbf{eff,GS}}$ and $\boldsymbol{\omega}_{\mathbf{eff,ES}}$ (Fig. 14A). Intuitively, this should reduce dephasing of the magnetization and R_{ex} since rotations around axes that have similar orientations should be less effective in scrambling magnetization compared to the case when the axes have very different orientations. Indeed, vector simulations show that for hypothetically fixed $\boldsymbol{\omega}_{\mathbf{eff,GS}}$ and $\boldsymbol{\omega}_{\mathbf{eff,ES}}$, R_{ex} is maximum for $\varphi = \pi/2$ while it is zero for $\varphi = 0$ (Fig. 15A). It is important to note that in an actual on-resonance $R_{1\rho}$ experiment, changing ω_1 also changes $\boldsymbol{\omega}_{\mathbf{eff,GS}}$ and $\boldsymbol{\omega}_{\mathbf{eff,ES}}$ (Fig. 14A). Simulations show that when fixing φ, R_{ex} increases with $\omega_{eff,ES}$ until it approaches k_{ex} after which it plateaus, while showing little variation with $\omega_{eff,GS}$ (Fig. 15B). Simulations also suggest that overall, the decrease in φ outweighs the increase in $\omega_{eff,ES}$ to cause a net decrease in R_{ex} with increasing ω_1 under on-resonance conditions. This can be appreciated from the diminished spread of the magnetization bouquet depicted using a Sanson Flamsteed projection[192] in Fig. 14A and Supplementary Movie 1. At very high ω_1, the measured value of $R_{1\rho}$ approaches R_2 and this illustrates how by changing ω_1 it is feasible to resolve the R_2 contribution to $R_{1\rho}$ (Fig. 14B).

The above framework also helps us rationalize why R_{ex} increases with $\Delta\omega$; as $\Delta\omega$ increases so does φ, thus increasing R_{ex} (Fig. 14A, Supplementary Movie 2). Algebraic expressions (Section 6.2) show that R_{ex} is proportional to $\Delta\omega^2$ in the presence of a spin-locking field. How R_{ex} varies with ω_1 will also depend on other exchange parameters. Fig. 14B shows on-resonance RD profiles for various values of p_{ES} and k_{ex}. Corresponding profiles for a wider range of k_{ex} and p_{ES} are shown in Fig. 16. From these RD profiles, we see that R_{ex} increases with p_{ES}. For $p_{ES} << p_{GS}$, R_{ex} will be maximum at a given ω_1 when $k_{ex} = \left(\Delta\omega^2 + \omega_1^2\right)^{1/2}$ and will decrease for other k_{ex} values, as can be appreciated from algebraic expressions in Section 6.2.

3.5. Off-resonance $R_{1\rho}$

Although the variation of R_{ex} with ω_1 depends on all exchange parameters, it is not possible to determine each of them individually from on-resonance $R_{1\rho}$ RD profiles measured at a single magnetic field[13]. Rather, inspection of algebraic equations (see Section 6.2) reveals that in general only k_{ex} and $p_{GS}p_{ES}\Delta\omega^2$ can be obtained under fast exchange (Eqn. 66) while $p_{GS}p_{ES}\Delta\omega^2 k_{ex}$ and $(\Delta\omega^2 + k_{ex}^2)$ can be determined under slow exchange when $p_{ES} << p_{GS}$ (Eqn. 65). Changing ω_{rf}, the carrier frequency of the spin-locking field, provides a means of obtaining additional data that can address this gap. As will be elaborated upon in Section 4.2, the variation of R_{ex} with ω_{rf} during an off-resonance $R_{1\rho}$ experiment features a symmetric peak centered at a position that corresponds to $\omega_{0,ES}$[23]. This makes it possible to determine $\Delta\omega$ including its sign, thereby enabling one to resolve the $p_{GS}p_{ES}\Delta\omega^2$ term obtained in the onresonance experiment, while generally also improving the ability to characterize all other exchange parameters.

Under fast exchange conditions, changing Ω_{AVG} in an off-resonance $R_{1\rho}$ experiment makes it possible to sample additional configurations of $\boldsymbol{\omega}_{\mathbf{eff,GS}}$ and $\boldsymbol{\omega}_{\mathbf{eff,ES}}$ relative to the onresonance $R_{1\rho}$ experiment. In principle, $\boldsymbol{\omega}_{\mathbf{eff,GS}}$ and $\boldsymbol{\omega}_{\mathbf{eff,ES}}$ are each specified by two parameters (length and angle with respect to the z-axis) that can vary independently to assume all allowed configurations. However, experimentally, since both the GS and ES always sense the same $\boldsymbol{\omega}_{\mathbf{1}}$, not all parameters can be varied independently. Rather, once ω_1 and Ω_{AVG} are specified, all four remaining parameters (two lengths and two angles) are fixed, due to the relations:

$$\Omega_{GS} = \Omega_{AVG} - p_{ES}\Delta\omega \quad (45)$$

$$\Omega_{ES} = \Omega_{AVG} - p_{GS}\Delta\omega \quad (46)$$

Consequently, specifying ω_1 and Ω_{AVG} determines $\boldsymbol{\omega}_{\mathbf{eff,GS}}$ and $\boldsymbol{\omega}_{\mathbf{eff,ES}}$, and the angle φ between them:

$$\varphi = tan^{-1}\left(\frac{\omega_1}{\Omega_{GS}}\right) - tan^{-1}\left(\frac{\omega_1}{\Omega_{GS}+\Delta\omega}\right) \quad (47)$$

In an analogous manner, specifying Ω_{GS} in addition to ω_1 during an off-resonance $R_{1\rho}$ experiment under slow exchange conditions also fixes $\boldsymbol{\omega}_{\mathbf{eff,GS}}$ and $\boldsymbol{\omega}_{\mathbf{eff,ES}}$.

A general expression for $R_{1\rho}$ applicable for off-resonance conditions is given by[23]:

$$R_{1\rho} = R_1 cos^2\theta + R_2 sin^2\theta + R_{ex}(\omega_1, \Omega) sin^2\theta \quad (48)$$

where θ is the angle between $\boldsymbol{\omega}_{\mathbf{eff,OBS}}$ and the z-axis, which corresponds to $\boldsymbol{\omega}_{\mathbf{eff,AVG}}$ for intermediate and fast exchange, and $\boldsymbol{\omega}_{\mathbf{eff,GS}}$ for slow exchange (Fig. 11B). Similar assumptions apply as for on-resonance $R_{1\rho}$ (Section 3.4). The expression is analogous to that for $R_{1\rho}$ in the absence of exchange, except for the addition of the R_{ex} term. Note that because R_{ex} adds to transverse relaxation, it is also weighted by $\sin^2\theta$. Thus, R_{ex} will depend on the extent of dephasing of the total magnetization along the effective field as measured by $R_{1\rho}$, which in turn depends on both the angle φ and $\omega_{eff,ES}$ as described in Section 3.4, and also on $\sin^2\theta$, which measures the fractional contribution to $R_{1\rho}$ from dephasing in the transverse plane.

As mentioned earlier, a key feature of the off-resonance experiment is that R_{ex} is maximum when on-resonance with the ES, providing a means of determining Δω and $\omega_{0,ES}$. We can use the vector model to understand this important point. We focus on the case in which $\omega_{eff,ES} > k_{ex}$, typically valid for $k_{ex} < \sim 300\ s^{-1}$ usually corresponding to the slow exchange regime. Under these conditions, the variation of $R_{1\rho}$ with Ω_{GS} is dominated by changes in φ,

while the dependency on $\omega_{eff,ES}$ is weak, as $R_{1\rho}$ has already reached saturation relative to $\omega_{eff,ES}$ (Fig. 15B).

Let us first consider the case in which ω_1 is fixed and the carrier is gradually moved far off-resonance, i.e., $|\Omega_{GS}| >> 0$. This causes $\omega_{eff,GS}$ and $\omega_{eff,ES}$ to gradually tilt away from the transverse plane, decreasing φ while $\theta \rightarrow \pi$ for $\Omega_{GS} << 0$ and $\theta \rightarrow 0$ for $\Omega_{GS} >> 0$. As the angle φ decreases, the decrease in $R_{1\rho}$ due to reduced scrambling of the magnetization outweighs the decrease in $\sin^2\theta$, leading to a net decrease in R_{ex} (Fig. 17). There comes a point at which $\boldsymbol{\omega_{eff,GS}}$ and $\boldsymbol{\omega_{eff,ES}}$ are aligned nearly parallel to $\boldsymbol{\omega_0}$ ($\theta \rightarrow 0$) and $R_{1\rho}$ is dominated by R_1 rather than by $R_2 + R_{ex}$. This provides a means for resolving the R_1 contribution to $R_{1\rho}$. Furthermore, this also increases the uncertainty in R_{ex} as one moves off-resonance. In practice, Ω is chosen such that $|\Omega| < 3.5\omega_1$ and $\theta < 15°$[21].

As we move closer to being on-resonance with the GS or ES, both $\boldsymbol{\omega_{eff,GS}}$ and $\boldsymbol{\omega_{eff,ES}}$ decrease in amplitude and are increasingly tilted toward the transverse plane, tending towards $\theta \rightarrow \pi/2$ and consequently increasing $\sin^2\theta$. This increase in $\sin^2\theta$ is outweighed by the increase in $R_{1\rho}$ due to the concurrent increase in φ, resulting in a net increase in R_{ex} (which, in the absence of relaxation, is equal to $R_{1\rho}/\sin^2\theta$) (Fig. 17). Again, intuitively, the maximum dephasing and therefore $R_{1\rho}$ should be achieved when the angle φ is maximum. This is indeed the case; $R_{1\rho}$ is maximum when placing the carrier right in the middle between $\omega_{0,GS}$ and $\omega_{0,ES}$ ($\omega_{rf} = ½ (\omega_{0,GS} + \omega_{0,ES})$, $\Omega_{GS} = ½(\omega_{0,GS} - \omega_{0,ES})$) (Fig. 17). However, this is not the offset that maximizes R_{ex}. Rather, as noted by Palmer[23], the maximum R_{ex} is always achieved when placing the offset on-resonance with $\omega_{0,ES}$ as this maintains a large φ angle while also minimizing θ and therefore $\sin^2\theta$. This results in a smaller $\sin^2\theta$ term and a larger $R_{1\rho}$ value, consequently maximizing R_{ex} (Fig. 17). Put in different words, the trade-off between maximizing φ and consequently $R_{1\rho}$, in combination with minimizing θ to reduce $\sin^2\theta$ is best satisfied when onresonance with the ES. The underlying basis for this rule lies in the fact that the orientations of the effective fields are coupled to the angle φ in $R_{1\rho}$ experiments. Thus, under slow exchange, off-resonance RD profiles are centered at $-\Delta\omega$, while under fast exchange conditions they are centered at $-p_{GS}\Delta\omega \sim -\Delta\omega$ when $p_{ES} << p_{GS}$, as described by Palmer *et al.*[23, 179, 182]. Under intermediate exchange, they are centered at $-(\Delta\omega-\psi)$, where ψ is the observed resonance frequency in the presence of exchange, assuming $\omega_{0,GS} = 0$ and $\omega_{0,ES} = \Delta\omega$.

It should be apparent that off-resonance $R_{1\rho}$ not only provides a means of characterizing the exchange parameters associated with R_{ex} and micro-to-millisecond exchange, but, as an added bonus, it simultaneously allows one to determine R_1 and R_2, which can be used to characterize fast picosecond-to-nanosecond dynamics.

4. Illustrative examples of $R_{1\rho}$ relaxation dispersion profiles

In this section, we review the B-M equations, which are first-order differential equations describing the evolution of the magnetization in the presence of chemical exchange, relaxation, and $\boldsymbol{B_0}$ and $\boldsymbol{B_1}$ magnetic fields. We then use the B-M equations to simulate off-resonance $R_{1\rho}$ RD profiles for a wide range of exchange scenarios, including three-state exchange with various topologies, and for cases in which $R_{2,GS}$ and $R_{2,ES}$ are unequal.

Theoretical simulations will be accompanied in some cases with experimental examples. The goal is to develop a deeper understanding regarding how off-resonance $R_{1\rho}$ RD profiles vary as a function of the exchange parameters and to extend description of the $R_{1\rho}$ experiment to three-state exchange.

4.1. Description of chemical exchange using Bloch-McConnell equations

We first review the B-M equations for a two-state system in the absence of chemical exchange, and later move to systems with two-state chemical exchange. In the absence of chemical exchange, M_{GS} and M_{ES} can be treated independently, evolving according to their respective relaxation matrices. For a two-state system without chemical exchange, the Bloch equations take the following form in the rotating frame of $\boldsymbol{\omega_1}$:

$$\frac{d}{dt}\begin{pmatrix} M_{GSx} \\ M_{ESx} \\ M_{GSy} \\ M_{ESy} \\ M_{GSz} \\ M_{ESz} \end{pmatrix} = \begin{pmatrix} -R_{2,GS} & 0 & -\Omega_{GS} & 0 & 0 & 0 \\ 0 & -R_{2,ES} & 0 & -\Omega_{ES} & 0 & 0 \\ \Omega_{GS} & 0 & -R_{2,GS} & 0 & -\omega_1 & 0 \\ 0 & \Omega_{ES} & 0 & -R_{2,ES} & 0 & -\omega_1 \\ 0 & 0 & \omega_1 & 0 & -R_{1,GS} & 0 \\ 0 & 0 & 0 & \omega_1 & 0 & -R_{1,ES} \end{pmatrix} \begin{pmatrix} M_{GSx} \\ M_{ESx} \\ M_{GSy} \\ M_{ESy} \\ M_{GSz} \\ M_{ESz} \end{pmatrix} + \begin{pmatrix} 0 \\ 0 \\ 0 \\ 0 \\ R_{1,GS}M_{z,eq,GS} \\ R_{1,ES}M_{z,eq,ES} \end{pmatrix} \quad (49)$$

As in the case for the Bloch equations for a single state (Section 3.2), the diagonal elements of the relaxation matrix and $M_{z,eq}$ terms describe the influence of R_1 and R_2 on M_{GS} and M_{ES}. The off-diagonal elements in the relaxation matrix describe the interchange between the x and y components ($M_{GSx} \rightarrow M_{GSy}$ and $M_{ESx} \rightarrow M_{ESy}$) and between the y and z components ($M_{GSy} \rightarrow M_{GSz}$ and $M_{ESy} \rightarrow M_{ESz}$) components due to precession about the z and x-axes under $\boldsymbol{\Omega}$ and $\boldsymbol{\omega_1}$, respectively. The equations are valid for $\tau_c << T_2$ (see Section 3.2).

The Bloch equations can be modified to accommodate chemical exchange, by adding exchange terms describing the magnetization transfer between the states at rates equal to the rate constants for chemical exchange[45]. They can be written in matrix form as follows:

$$\frac{d}{dt}\overrightarrow{\boldsymbol{M}(t)} = K\overrightarrow{\boldsymbol{M}(t)} + \overrightarrow{\boldsymbol{B}} \quad (50)$$

where

$$\overrightarrow{\boldsymbol{M}(t)} = \begin{pmatrix} M_{GSx} \\ M_{ESx} \\ M_{GSy} \\ M_{ESy} \\ M_{GSz} \\ M_{ESz} \end{pmatrix} \quad (51)$$

$$K = \begin{pmatrix} -R_{2,GS} & 0 & -\Omega_{GS} & 0 & 0 & 0 \\ 0 & -R_{2,ES} & 0 & -\Omega_{ES} & 0 & 0 \\ \Omega_{GS} & 0 & -R_{2,GS} & 0 & -\omega_1 & 0 \\ 0 & \Omega_{ES} & 0 & -R_{2,ES} & 0 & -\omega_1 \\ 0 & 0 & \omega_1 & 0 & -R_{1,GS} & 0 \\ 0 & 0 & 0 & \omega_1 & 0 & -R_{1,ES} \end{pmatrix} + \begin{pmatrix} -k_1 & k_{-1} & 0 & 0 & 0 & 0 \\ k_1 & -k_{-1} & 0 & 0 & 0 & 0 \\ 0 & 0 & -k_1 & k_{-1} & 0 & 0 \\ 0 & 0 & k_1 & -k_{-1} & 0 & 0 \\ 0 & 0 & 0 & 0 & -k_1 & k_{-1} \\ 0 & 0 & 0 & 0 & k_1 & -k_{-1} \end{pmatrix} \quad (52)$$

and

$$\vec{B} = \begin{pmatrix} 0 \\ 0 \\ 0 \\ 0 \\ R_{1,GS}M_{z,eq,GS} \\ R_{1,ES}M_{Z,eq,ES} \end{pmatrix} \quad (53)$$

The diagonal terms in the matrix of rate constants correspond to the decrease of M_{GS} and M_{ES} due to exchange events in which spins leave the GS ($M_{GS} \rightarrow M_{ES}$) or the ES ($M_{ES} \rightarrow M_{GS}$). In contrast, the off-diagonal terms correspond to the increase of M_{GS} and M_{ES} due to exchange events in which spins arrive at the GS ($M_{ES} \rightarrow M_{GS}$) or the ES ($M_{GS} \rightarrow M_{ES}$). As molecules in the GS transform into the ES with a rate of k_1[GS], where [GS] is the concentration of the GS species, the associated components of the magnetization of the GS (M_{GSi}, i = x, y or z) decrease with rates of $k_1 M_{GSi}$, as M_{GSi} is proportional to [GS]. Analogous considerations are also applicable for the case of *n*-state exchange. The assumptions under which the above equations are valid are given in Section 3.4. It should be noted that the B-M equations can be used to treat the behavior of the magnetization under free precession conditions by setting $\omega_1 = 0$.

The solution to a first-order linear differential equation such as $\frac{d}{dt}\vec{M(t)} = K\vec{M(t)} + \vec{B}$ has the form:

$$\vec{M(t)} = \sum_{i=1}^{6} \exp(\lambda_i t)\vec{l}_i + \vec{a} \quad (54)$$

where λ_i and $\vec{l}_i$ are the i^{th} eigenvalue and eigenvector of matrix K respectively, and $\vec{a}$ is the stationary solution[23, 193]. For realistic values of exchange parameters, considering the presence of an inhomogeneous spin-locking field, the decay of the magnetization in most cases is mono-exponential and dominated by the least negative eigenvalue, denoted as $R_{1\rho}$[23, 163]. Indeed, even if the spin-locking field is homogeneous, with the exception of exchange scenarios with low k_{ex} and high p_{ES}, the decay of the magnetization is mono-

exponential, as described in Section 4.2. A non-monoexponential decay of the magnetization is typically a consequence of oscillatory motions of a component of the magnetization that is not parallel to the effective field. The effects of such oscillatory motions are diminished by inhomogeneous spin-locking fields because of differences in the frequencies of oscillation of the magnetization in different parts of the sample. An analogous solution is also valid for the case of *n*-state exchange with arbitrary topological complexity as described by Palmer[193, 194]. Thus, the variation of $R_{1\rho}$ with ω_1 and Ω can be used to characterize chemical exchange, including $n > 2$ state exchange with arbitrary topologies, so long as the decay of magnetization is mono-exponential.

4.2. Off-resonance $R_{1\rho}$ relaxation dispersion profiles for two and three-state exchange

Understanding how off-resonance $R_{1\rho}$ RD profiles vary with exchange parameters is essential when analyzing $R_{1\rho}$ data. Here, we explore these variations by numerically integrating the B-M equations. The initial alignment of magnetization assumed in these simulations was performed as described in Section 6.1.

4.2.1. Two-state exchange—Fig. 18 shows representative off-resonance RD profiles for two-state GS⇌ES exchange as a function of p_{ES} and k_{ex}. These profiles show the dependence of $R_{2,eff} = R_2 + R_{ex}$ on Ω and ω_1. Over this range of p_{ES} and k_{ex}, the RD profiles feature a symmetric peak centered near −Δω. The height of the peak relative to the baseline (which is at R_2) is equal to R_{ex}.

Increasing p_{ES} increases the peak height (R_{ex}) in addition to its width, and higher spin-lock amplitudes are needed to suppress larger R_{ex} contributions (Fig. 18). For a given ω_1 and Ω, algebraic expressions in Section 6.2 (Eqn. 65) show that R_{ex} increases until k_{ex} approaches $\left(\Omega_{ES}^2 + \omega_1^2\right)^{1/2}$ (for $p_{ES} << p_{GS}$) where it reaches a maximum (Fig. 19), and is maximally dependent on ω_1. Representative experimental RD profiles for two-state exchange are shown in Fig. 20 for nucleic acid systems with different exchange regimes.

Simulated RD profiles for a wider range of p_{ES} and k_{ex} are shown in Fig. 21. The RD profiles are flat for extremes of very slow (≤ 0.2 s^{-1}) or fast (≥ 100,000 s^{-1}) k_{ex} and for low p_{ES} (≤ 0.01 %) (Fig. 21). In line with this, exchange processes in nucleic acids that have been experimentally characterized using off-resonance $R_{1\rho}$ RD have p_{ES} between 0.02 % and 14 %, and k_{ex} between ~400 s^{-1} to 50,000 s^{-1}[16, 164, 195]. In general, for fast exchange with k_{ex} on the order of 20,000 s^{-1}, the RD profiles are broad with small R_{ex}, making it more difficult to define the peak center and therefore Δω, and higher spin-lock amplitudes are needed to suppress the smaller R_{ex} contributions. However, the profiles continue to remain centered at −Δω. This is in contrast to the fast exchange equations, which predict that the profiles should be centered at 0[196] (Eqn. 66, Section 6.2).

Additional simulations were performed to assess more rigorously the detection limits of the off-resonance $R_{1\rho}$ RD experiment for two-state exchange. While the results vary depending on the exchange parameters and measurement uncertainty, some general remarks can be made. For typical values of $\Delta\varpi$, the slowest exchange process that can be reliably detected has k_{ex} ~ 10 s^{-1} although even k_{ex} ~ 1 s^{-1} can be reliably characterized for high p_{ES} (Fig.

22). The upper limit for k_{ex} is ~50,000 s^{-1} although this can vary depending on the exchange parameters and measurement uncertainty. The lower limit for p_{ES} is ~0.02 % for a ^{15}N spin with very large $\Delta\overline{\omega}(30\,\text{ppm})$ associated with deprotonation[197], but is more typically ~0.1 % for a ^{13}C spin with $\Delta\overline{\omega} = 3$ ppm (Fig. 22). As expected, doubling Δω allows ~4-fold smaller p_{ES} values to be characterized given that R_{ex} is proportional to $p_{ES}\Delta\omega^2$ (Section 6.2).

Interestingly, under slow exchange ($k_{ex}/\Delta\omega < 0.1$) with high p_{ES} (> 1 %), the simulated RD profiles are asymmetric, particularly for low ω_1 (Fig. 21). These asymmetries arise due to gradual changes in the alignment of M_{ES} from its initial state along $\boldsymbol{\omega_{eff,GS}}$ toward $\boldsymbol{\omega_{eff,ES}}$ during the relaxation period. For high p_{ES}, this veering off of M_{ES} also leads to oscillations in the magnetization decay[23, 163]($p_{ES} \geq 1\%$, $k_{ex} \leq 20\ s^{-1}$) (Fig. 13C). These contributions can be suppressed by avoiding an equilibration delay following selective excitation of the GS so as to minimize M_{ES} during the relaxation period (Section 5.2)[28].

The RD profiles in Fig. 21 also show that 10-fold changes in p_{ES} or k_{ex} can result in very large changes in the RD profiles. For example, large and significant RD (p_{ES} = 10 %, k_{ex} = 20000 s^{-1}) can become undetectable (p_{ES} = 10 %, k_{ex} = 100000 s^{-1}). One cannot therefore simply relate a change in magnitude in the RD profile to a corresponding change in exchange parameters. A related point is that there is a danger of over-interpreting the absence of RD as evidence for the absence of an ES. Thus, it is advisable to vary experimental conditions in order to bring exchange processes within the detection limits of the experiment.

4.2.2. Three-state exchange: Star-like topology without minor exchange—So far we have considered two-state exchange involving a single ES. However, several $R_{1\rho}$ studies report two detectable ESs in nucleic acids[117, 195, 197]. As detailed by Palmer[193], the way in which a second ES impacts the RD profile will depend on the kinetic topology. We first consider the topology ES2⇌GS⇌ES1 in which direct exchange between ES1 and ES2 (ES1⇌ES2) is assumed to be sufficiently slow as to have a negligible effect on $R_{1\rho}$ (Fig. 23). The shape of such topologies in which multiple ESs exchange with the GS, but not amongst each other, resembles a star, and therefore these topologies are called “star-like”. We examine how inclusion of ES2⇌GS exchange impacts the two-state RD profiles observed for GS⇌ES1 exchange. To aid in visualizing the two ES contributions, the simulations assume that the ESs have Δω values with opposite signs, i.e., $\Delta\omega_1\Delta\omega_2 < 0$, where $\Delta\omega_1 = \omega_{0,ES1} - \omega_{0,GS}$ and $\Delta\omega_2 = \omega_{0,ES2} - \omega_{0,GS}$, $\omega_{0,ES1}$ and $\omega_{0,ES2}$ being the Larmor frequencies of ES1 and ES2, respectively.

As shown in Fig. 23A, the RD profiles for star-like three-state exchange are approximately given by the sum of two RD profiles for each of the two two-state exchange processes, with the three-state exchange resulting in a larger R_{ex} compared to either of the two separate two-state processes[193]. Two separate RD peaks are observed centered at $-\Delta\omega_1$ and $-\Delta\omega_2$. Similar behavior would be applicable for the case of having three or more ESs in a startopology, in which each ES would be associated with its own RD profile. It should be noted that two ESs in a star-like topology can be resolved even if they have identical Δω values, as long as they have sufficiently different k_{ex} and/or p_{ES} values (Fig. 23B).

An example of a star-like topology has been reported for DNA duplexes in the context of Watson-Crick to Hoogsteen (A(*anti*)-T(*anti*) to A(*syn*)-T(*anti*) and G(*anti*)-C(*anti*) to G(*syn*)-C^+(*anti*)) transitions in B-DNA. The RD profiles measured for the sugar C3′ show two discrete peaks[117] (Fig. 24). Here, the C3′ spins sense Watson-Crick to Hoogsteen transitions of the constituent BP and its neighbor. The RD profiles could be satisfactorily fitted to three-state exchange with a star-like exchange topology as expected, given that the Watson-Crick to Hoogsteen transitions at neighboring BPs are independent of one another and can occur with different rates[117].

4.2.3. Three-state exchange: Triangular and linear topologies with minor exchange—We now consider how the off-resonance $R_{1\rho}$ RD profiles vary for three-state exchange in the presence of direct exchange between the two ESs in a triangular topology. By definition exchange processes not involving the dominant GS are referred to as ‘minor’ [193], thus the exchange rate between the two ESs is denoted by $k_{ex,minor}$. As expected, when $k_{ex,minor}$ is slow relative to $k_{ex,1}$ describing GS⇌ES1 and $k_{ex,2}$ describing ES2⇌GS exchange, the RD profiles are identical to those obtained for the star topology (Fig. 25). The contribution from exchange between the two ESs increases as $k_{ex,minor}$ approaches $k_{ex,1}$ or $k_{ex,2}$. This has the effect of ‘averaging’ the ES1 and ES2 chemical shifts[195], resulting in an asymmetric RD profile in which the positions of RD peaks of the two ESs shift toward one another. Further increasing $k_{ex,minor}$ results in coalescence of the two ES RD peaks at a position determined by a populationweighted average over the Δω values of ES1 and ES2 (Fig. 25). This is analogous to what happens in free precession chemical exchange when two resonances coalesce in going from slow to fast exchange (Fig. 4A)[22].

Direct exchange between ESs has been reported experimentally for G-T/U mismatches exchanging between the wobble GS and two Watson-Crick-like ESs formed by tautomerization (ES1) or ionization (ES2) of the bases[165, 195, 197]. Under neutral pH, the RD profiles show a single ES (ES1), which was shown to be comprised of two distinct tautomeric species that exist in rapid equilibrium G^{enol}-T/U⇌G-T^{enol}/U^{enol} leading to a single coalesced RD peak[195]. Interestingly, a second ES (ES2) comprising anionic Watson-Crick G-T^-/U^- was observed at higher pH, leading to deviations in the RD profiles from the perfect symmetry expected for two-state exchange. Some RD profiles showed a statistically significant improvement when fitted to a three-state model with minor exchange in a triangular rather than a star-like topology[195] (Fig. 26). It should be noted that fitting RD profiles for a three-state system undergoing minor exchange without taking it into account can result in errors in the estimates of $\Delta\omega_1$ and $\Delta\omega_2$.

When the exchange is slow between the GS and one of the two ESs, the system can be described by a ‘linear’ topology GS⇌ES1⇌ES2[193]. Here, the detectability of ES2 can be determined by the kinetics of the GS⇌ES1 exchange. Once again, two discrete ESs peaks are observed or a single coalesced peak, depending on the exchange parameters including the relative values of $k_{ex,1}$ and $k_{ex,minor}$ (Fig. 25).

As the appearance of three-state RD profiles can vary greatly with exchange parameters, the authors’ group provides an interactive tool (https://github.com/alhashimilab/

InteractiveProfiles), which allows a user to vary the exchange parameters for a three-state system and simulate the effect on the RD profile.

4.2.4. Impact of unequal R_2 for ground and excited states—The above simulations assume equal R_1 and R_2 values for the GS and ES, i.e., $\Delta R_1 = R_{1,ES} - R_{1,GS} = 0$ and $\Delta R_2 = R_{2,ES} - R_{2,GS} = 0$. Deviations from this assumption can arise, particularly for R_2. For example, transitions toward ESs can entail the flipping in or out of nucleotide bases[16] that can be accompanied by large changes in ps-ns dynamics and therefore R_2[7, 198–200]. Especially for large RNAs, this can amount to ΔR_2 for C6/C8 and C1′ as large as ~100 s^{-1}[201]. Secondly, nucleic acid ESs can feature ionized or tautomeric bases[195, 197], which can have different dipolar contributions to relaxation, profoundly affecting R_2. Finally, melting/annealing of duplexes as well as dimerization of hairpins can involve large changes in overall molecular tumbling that can also lead to large ΔR_2[190]. It is therefore instructive to understand how differences in ΔR_2 impact the RD profiles.

As noted by Kay *et al.*, a non-zero ΔR_2 has characteristic effects on the RD profile[187, 202]. For large $\Delta R_2 \sim 100\ s^{-1}$, the RD peak is no longer symmetric, and $R_{2,eff}$ values are larger for offsets that correspond to having the ES near resonance[187] (Fig. 27A). The magnitude of the asymmetry depends primarily on $\Delta R_2/k_{ex}$; in the limit of $\Delta R_2/k_{ex} = 0$, the RD profiles are symmetric but they become increasingly more asymmetric with increasing $\Delta R_2/k_{ex}$[202]. The asymmetry due to unequal R_2 is in general larger for smaller $\Delta\bar{\omega}$ values (Fig. 27B). Even in the limit of $\Delta\bar{\omega} = 0$ ppm, an ES can be detected provided it has a sufficiently large ΔR_2; for $p_{ES} > 10$ %, ΔR_2 as small as 20 – 30 s^{-1} can be detected even when $\Delta\bar{\omega} = 0$ ppm [187]. The off-resonance RD profiles in such cases are symmetrically centered at the carrier frequency but are ‘inverted’ (Fig. 27C) relative to the canonical two-state RD profiles (Section 4.2.1).

5. Experiments for measuring off-resonance $R_{1\rho}$ relaxation dispersion in uniformly $^{13}C/^{15}N$ labeled nucleic acids

5.1. Challenges and solutions for measuring off-resonance $R_{1\rho}$

1D $R_{1\rho}$ experiments employing selective excitation schemes reviewed here for measuring $R_{1\rho}(^{15}N)$ and $R_{1\rho}(^{13}C)$ in nucleic acids are straightforward adaptations of experiments originally developed to measure $R_{1\rho}(^{15}N)$ and $R_{1\rho}(^{13}C)$ in proteins[154, 203, 204]. Before we describe the 1D $R_{1\rho}$ experiments, we review three key challenges that were addressed to allow optimal measurements of $R_{1\rho}$ in biomolecules.

5.1.1. Spin-lock amplitude limitations associated with alignment of magnetization along the effective field—So far we have considered the behavior of a single spin during the $R_{1\rho}$ experiment. In practice, one is interested in measuring $R_{1\rho}$ simultaneously for a large number of spins in a biomolecule. This presents a challenge, as the different spins in a molecule generally have different Larmor frequencies and will therefore be associated with different effective fields. Aligning all spins along their respective effective fields is not straightforward, particularly when using low spin-lock amplitudes, for which differences in the effective field orientations are most significant.

Early heteronuclear 2D $R_{1\rho}$ experiments employed high spin-lock amplitudes (>1000 Hz) and/or high offsets and used hard pulses to align the magnetization of all spins along a common effective field[154, 203, 204]. As $R_{1\rho}$ experiments are sensitive to exchange processes with $k_{ex} \sim \omega_{eff}$, this limited sensitivity to motions on the fast microsecond timescale. The misalignment of spins that are far off-resonance, and gradual decay of the magnetization component perpendicular to $\boldsymbol{\omega_{eff,OBS}}$ due to the inhomogeneity of the spin-locking field results in oscillations during the relaxation period and in losses in sensitivity[205, 206]. Alternative magnetization alignment schemes were subsequently developed that used adiabatic ramps with amplitude, phase or frequency modulation to optimally align as many spins as possible along their respective effective fields[181, 205, 207–209]. While these schemes improved magnetization alignment, they were still limited to high spin-lock amplitudes, since low amplitudes require long adiabatic sweeps to optimally align the magnetization of individual spins along a broad range of effective field orientations, resulting in large sensitivity losses due to relaxation[181, 208].

5.1.2. Suppressing cross-correlated relaxation and heteronuclear scalar couplings—

It has long been recognized that cross correlation between dipolar and chemical shift anisotropy (DD_{NH}/CSA_N) contributions to relaxation can affect ^{15}N T_1 and T_2 measurements in macromolecules[157, 210, 211]. Cross-correlated relaxation converts transverse or longitudinal spin operators of order one to order two (S_x -> $2S_xI_z$ and S_z -> $2S_zI_z$ where $S = {}^{15}N$ and $I = {}^{1}H$), thus introducing an alternative mode of relaxation in addition to auto-relaxation. For nucleic acids, in addition to sizeable DD_{NH}/CSA_N contributions to imino ^{15}N relaxation, suppressing DD_{CH}/CSA_C is also important for ^{13}C relaxation measurements in which the DD_{CH}/CSA_C contributions can be significant[201].

During the 1990s, it became apparent that various schemes used to suppress DD_{NH}/CSA_N interactions in ^{15}N RD experiments, such as appropriately spaced 180° ^{1}H pulses and ^{1}H decoupling elements[122, 205, 207, 209, 212, 213] were leading to systematic discrepancies in T_2 values measured using $R_{1\rho}$ and CPMG[158, 159]. This was later attributed to the evolution of heteronuclear $^{1}J_{NH}$ couplings[180, 181] during the $R_{1\rho}$ experiment, as a result of simultaneously pulsing on ^{15}N and ^{1}H for spin-locking and decoupling respectively. This led to the development of new approaches for more effectively suppressing both CSA_N/DD_{NH} and $^{1}J_{NH}$ scalar coupling evolution in $R_{1\rho}$ experiments that employ appropriately spaced ^{1}H pulses[181] or continuous wave ^{1}H irradiation with periodic phase inversion[180]. Although the 2D experiment developed by Palmer *et al.*[181] could be used to measured $R_{1\rho}(^{15}N)$ RD using low spin-lock amplitudes (150–1000 Hz), in practice, the use of adiabatic pulses for magnetization alignment resulted in significant losses in sensitivity, precluding collection of a large set of off-resonance $R_{1\rho}$ RD data for obtaining a complete set of exchange parameters.

5.1.3. Homonuclear scalar couplings complicate application of CPMG(^{13}C) in uniformly labeled nucleic acids—

For proteins, CPMG(^{15}N) RD experiments provide a wealth of information regarding chemical exchange[22]. For nucleic acids, suitable imino ^{15}N probes are only available for half the residues (guanine and uridine/thymine) and rarely for flexible sites of interest due to rapid exchange of imino protons with the solvent. For this

reason, there has always been interest in using ^{13}C spins as probes of nucleic acid dynamics[134]. However, extensive homonuclear C-C scalar (J_{CC}) coupling networks in base and sugar moieties in uniformly ^{13}C labeled nucleic acid samples complicate the application of CPMG RD experiments as hard 180° pulses can excite many coupled ^{13}C spins simultaneously[134, 136]. To address this problem, much effort has been directed toward the production of site-labeled[136, 177] or fractionally labeled[134] nucleotide-triphosphates (NTPs) through biomass production for use in enzymatic synthesis. Unfortunately, the site-labeled precursors are not commercially available. Interestingly, even though methods for site-specific incorporation of ^{13}C labels using phosphoramidite chemistry were available as early as the 1990s[214], it is only recently[18, 173, 174, 176, 215] that these methods have been used to enable CPMG studies of chemical exchange in nucleic acids. However, as is the case with site-labeled NTPs, these amidites are not commercially available. Furthermore, obtaining a large number of chemical shifts for ES characterization can become prohibitive with site-labeled samples, owing to the necessity for synthesizing separate samples with different labeling schemes.

5.1.4. Selective excitation addresses challenges in $R_{1\rho}$ relaxation dispersion studies of nucleic acids—

The 1D $R_{1\rho}(^{15}N)$ experiment introduced by Kay *et al.* in 2005[163] addresses many of the above-mentioned limitations. The experiment employs selective excitation schemes pioneered by Bodenhausen and colleagues[160–162] to excite signals corresponding to individual spins of interest. Rather than measuring $R_{1\rho}$ simultaneously for multiple spins at once, off-resonance $R_{1\rho}$ RD profiles are measured one at a time for specific spins in a molecule. This bypassed the need to simultaneously align multiple spins along their effective fields altogether since each spin is aligned one at a time. By obviating the need for adiabatic ramps, much lower spin-lock amplitudes (~25 Hz for ^{15}N) could be employed, broadening the sensitivity of $R_{1\rho}$ to millisecond timescale motions[163]. In addition, DD_{NH}/CSA_N (or DD_{CH}/CSA_C) and heteronuclear J_{NH} (or J_{CH}) scalar coupling evolution could be effectively suppressed by the application of an on-resonance ^1H continuous wave field[163, 211] during the spin-lock period. In addition, J_{CN} and J_{CC} scalar couplings could be more readily suppressed in $R_{1\rho}$ experiments by application of selective spin locking fields during the relaxation period. One downside is as the extra time needed to collect separate RD profiles for individual spins in a given molecule, relative to 2D $R_{1\rho}$ experiments.

A straightforward modification of the original 1D $R_{1\rho}(^{15}N)$ experiment allows $R_{1\rho}(^{15}N)$ and $R_{1\rho}(^{13}C)$ data to be measured in uniformly $^{13}C/^{15}N$ labeled nucleic acids[21, 112], and will be described in Section 5.2. These $R_{1\rho}$ experiments have been used to measure RD for a variety of sugar and base $^{13}C/^{15}N$ probes to obtain insights into chemical exchange over a broad range of timescales from micro to milliseconds in uniformly $^{13}C/^{15}N$ labeled nucleic acids ranging in size from 24–56 nucleotides[16, 21, 112, 117, 164–166].

5.2. Selective 1D pulse sequences for measuring $R_{1\rho}$ in uniformly $^{13}C/^{15}N$ labeled nucleic acids

Pulse sequences for measuring $R_{1\rho}(^{15}N)$ and $R_{1\rho}(^{13}C)$ in uniformly labeled nucleic acids in a 1D manner are shown in Fig. 28A. The experiments employ selective cross polarization

(CP)[160–162] to excite individual ^{15}N or ^{13}C spins of interest through the selective transfer of magnetization from directly bonded ^{1}H spins. This is accomplished by applying a 90°$_x$ pulse to create transverse I_y (I = ^{1}H) magnetization followed by spin-locking in the rotating frame by application of a long and selective 90° RF pulse (B_I) along the y-axis. Simultaneously, a long RF pulse (B_S) is applied along x on the S spin (S = ^{13}C or ^{15}N) to satisfy the Hartmann-Hahn matching condition $\gamma_I B_I = \gamma_S B_S$. The spins are then allowed to exchange magnetization in a manner dependent on the magnitude and duration of the RF fields, leading to generation of transverse S_x magnetization. In theory, complete transfer of magnetization from spin I to spin S takes place when the duration of the CP transfer (τ_{CP}) is set to $(2k\text{-}1)/J_{IS}$ and the amplitude of the RF pulses ($\omega_{CP} = \gamma_I B_I = \gamma_S B_S$) is set to $\omega_{CP}/2\pi = \left(\frac{\left(4n^2 - (2k-1)^2\right)}{(2k-1)^2}\right)^{1/2} J_{IS}/4$ (valid for $2(\omega_{CP}/2\pi) \sim J_{IS}$), where n and k are positive integers such that $n \geq k$ and J_{IS} is the scalar coupling between spins I and S. In practice, smaller values of τ_{cp} (= $1/J_{IS}$) are preferred so as to minimize sensitivity losses due to relaxation. Furthermore, as demonstrated by Bodenhausen *et al.*[216] lower values of $\omega_{CP}/2\pi\left(= 3^{1/2} J_{IS}/4\right)$ are also preferred because the transfer is more selective and less sensitive to RF field inhomogeneities and mismatches in the Hartmann-Hahn matching condition. The values of ω_{CP} and τ_{CP} are adjusted from their initial settings (Table 1) to maximize the signal intensity at the end of the $R_{1\rho}$ experiment, when setting the relaxation delay T_{relax} = 0. For AX and non-equivalent AX_2 spin systems (A = ^{13}C/^{15}N, X = ^{1}H), the CP transfer generates A_x magnetization from longitudinal X_z. For equivalent AX_2 spin systems, the transfer generates $A_x + 4X_{1Z}X_{2Z}A_X$ coherences. In the latter case, some magnetization will be lost due to competing pathways arising from evolution of the three-spin coherences[217].

The transverse S_x magnetization is then rotated to S_z through application of a hard 90° pulse. This is a followed by a delay $\tau_{eq} \sim 3/k_{ex}$ to allow equilibration of p_{GS} and p_{ES} (Fig. 28A). This is necessary as the ES, since it has a chemical shift different from the GS, may not have been excited by the selective Hartmann-Hahn transfer. A second hard pulse with a tip angle θ, i.e., the tilt angle of $\boldsymbol{\omega_{eff,OBS}}$, is then used to align the S_z magnetization of both the GS and ES along $\boldsymbol{\omega_{eff,OBS}}$ (Fig. 11B). A purge element is used to suppress magnetization from spins that have similar ^{1}H but different ^{13}C or ^{15}N Larmor frequencies via the application of a delay (ζ), that allows for dephasing of spins precessing with a frequency different from that of the target[163]. The ζ delay and purge element can be placed either before[21] or right after the spin-lock period[112, 163] (Fig. 28A).

The ^{13}C/^{15}N magnetization is then spin-locked during the relaxation period (T_{relax}) along $\boldsymbol{\omega_{eff,OBS}}$ by the application of a spin-locking field to the spin of interest. Here, care is taken to minimize Hartmann-Hahn transfers between pairs of scalar coupled spins such as C5–C6 (in pyrimidines), C1′-C2′, and C4/6-C8 (in purines) to typically < 1% of the maximum transfer efficiency[21]. This is accomplished by ensuring that the difference in the effective field strengths experienced by two coupled spins (*S1* and *S2*) is much greater than the coupling constant between them. The Hartmann-Hahn transfer efficiencies (A_{HAHA}) between spins *S1* and *S2* can be computed using[92]:

$$A_{HAHA} = \left(1 + \left(\frac{\omega_{eff,S1} - \omega_{eff,s2}}{0.5J_n(1 + cos(\theta_{S1} - \theta_{S2}))}\right)^2\right)^{-1} \quad (55)$$

where ω_{eff} and θ are the effective fields and tip angles of the two spins, and J_n is the scalar coupling between them. The offsets that minimize unwanted Hartmann-Hahn transfers (A_{HAHA} < 1%) in $R_{1\rho}(^{13}C)$ RD experiments are listed for a variety of ^{13}C spins in Table 2. In general, extraneous Hartmann-Hahn magnetization transfers are less relevant for ^{15}N spins compared to ^{13}C, owing to the smaller size of the J_n couplings (< 10 Hz)[218].

Selective irradiation of the ^{13}C or ^{15}N spins with a spin-locking field (Fig. 28A) during the relaxation period also serves to suppress evolution under J_{CC}, J_{NC}, and J_{NN}. These scalar coupling constants also set a lower limit on the spin-lock amplitude that can be used and, consequently, the slowest process that can be probed using $R_{1\rho}$ when working with isotopically labeled samples. Typically, ω_1 is set to be approximately three times larger than the largest relevant scalar coupling (Table 1). In contrast, the highest spin-lock amplitude that can be used is determined by the probe hardware, and this in turn determines the fastest process that can be probed using off-resonance $R_{1\rho}$ (Table 1). Spin-lock amplitudes as high as ~6.4 kHz for ^{15}N can be used with a cryo-probe (QCI Bruker) as compared to 4 kHz for a room-temperature probe, allowing measurement of exchange processes with exchange rates as high as 40000 s^{-1}[219].

During the relaxation period, evolution under $^1J_{NH}$ (or $^1J_{CH}$) and DD_{NH}/CSA_N (or DD_{CH}/CSA_C) are efficiently suppressed using a strong ^1H continuous-wave field (ω_{1H}) applied on the resonance of interest[211, 220] (Fig. 28A). ω_{1H} is chosen to be larger than the maximum effective ($^{13}C/^{15}N$) spin-locking field ($\omega_{1H} > \omega_{eff(max)}$) to avoid unwanted C-H or N-H polarization transfers during the spin-lock period through accidentally fulfilling a Hartmann-Hahn matching condition[163] (Table 1). The amino NH_2 spin system is also subject to dipole-dipole (DD_{NHA}/DD_{NHB}) cross-correlated relaxation, which can result in the generation of doubly antiphase magnetization ($4I_{1z}I_{2z}S_x$) from in-phase magnetization during the relaxation period. The DD_{NHA}/DD_{NHB} cross-correlated relaxation contribution scales as $(\tau_c/2)(3\cos^2\theta - 1)$[221], where θ is the angle between the two N-H bonds. The angular term is small (~ −0.125) for amino –NH_2 groups in which the angle between the bonds is ~120°. Thus, the DD_{NHA}/DD_{NHB} contribution for a 10 BP duplex is estimated to be ~0.5 s^{-1} and can be safely ignored[165]. In an analogous manner, extraneous contributions from J couplings and cross relaxation must also be taken into account when performing ^1H RD experiments, for which pulse sequences based on selective 1D excitation have also been reported[222, 223]. As the higher γ value for ^1H allows one to achieve higher spin-lock amplitudes, $R_{1\rho}(^1H)$ holds great promise for characterizing faster exchange processes in nucleic acids in the future, potentially without the need for isotopic enrichment.

At the end of the relaxation period, the component of the net magnetization along $\boldsymbol{\omega_{eff,OBS}}$ is tilted back along z by the application of a hard pulse, and is transferred back from ^{13}C or ^{15}N to ^1H using CP for subsequent detection (Fig. 28A). Consistent temperature throughout the experiment is maintained by a heat-compensation element[21, 163] that is applied far

offresonance; this consists of ^{1}H and ^{13}C or ^{15}N spin-locking fields applied for a given amount of time ($T_{max} - T_{relax}$), where T_{max} is the longest relaxation time and T_{relax} is the relaxation time in a given scan. T_{max} is typically set to a value that results in ~30% intensity loss relative to the value measured at $T_{relax} = 0$ for the resonance of interest, while also taking into account probe hardware limitations that may arise for longer T_{max}. The water signal is suppressed using either low amplitude presaturation during inter-scan delays with additional purge elements for ^{13}C experiments or with a WATERGATE element[224] before acquisition for ^{15}N experiments (Fig. 28A). Decoupling pulses are applied to ^{13}C or ^{15}N during acquisition. The spins in nucleic acids that can be targeted using these 1D $R_{1\rho}$ experiments are shown in Fig. 28B.

The experiment yields a 1D ^{1}H NMR spectrum for the resonance of interest and in some cases additional nearby resonances, especially if their chemical shifts overlap in both ^{1}H and ^{13}C/^{15}N dimensions (Fig. 29). A total of ~10 T_{relax} delays are typically measured and the intensity of the peak of interest is fitted to a mono-exponential decay $I = I_0 \exp(-R_{1\rho} T_{relax})$ using a nonlinear fitting algorithm to obtain the value of $R_{1\rho}$ (Fig. 29). On-resonance $R_{1\rho}$ data is typically collected initially by setting $\Omega = 0$ and decay curves are measured at ~ 20 $\omega_1/2\pi$ values ranging between 50 – 2000 Hz and 50 – 3600 for ^{15}N and ^{13}C, respectively. Off-resonance $R_{1\rho}$ data are then measured by varying both $\Omega/2\pi$ and $\omega_1/2\pi$ (typically three or more values spanning the ranges described above). The maximum value $\Omega_{max}/2\pi$ is generally set to ~$3 - 4 \times \omega_1/2\pi$ (Section 3.5). Typically, a total of ~ 24 values of $\Omega/2\pi$ are chosen with equal spacing to span $\pm \Omega_{max}/2\pi$ symmetrically about $\Omega/2\pi = 0$. In cases where there is an *a priori* estimate of $\omega_{0,ES}$, offsets can be chosen accordingly to sample points where R_{ex} would be non-zero. Note that it may be important to collect $R_{1\rho}$ data for multiple experimental sample conditions, as the appearance of the profiles is sensitive to the conditions used (Section 4.2, Section 7.2.3).

5.3. Calibrating the spin-lock amplitude

When setting up the $R_{1\rho}$ experiment it is important to calibrate the ^{13}C and ^{15}N spin-lock amplitudes[22, 180]. This involves finding the optimal power in dB (decibels) or W (watts) for the spin-lock pulse of a given frequency. In general, spin-lock amplitude calibration is done when setting up experiments on a new probe and need not be repeated when switching samples or changing temperature. The calibration is performed using a modified version of the $R_{1\rho}$ pulse sequence in which the pulses with phases ϕ_3 and ϕ_4 flanking the spin-lock element that tilt magnetization along $\boldsymbol{\omega_{eff,OBS}}$ have been removed (Fig. 28A). This can be done by omitting the pulses from the pulse program or by simply setting the pulse duration to zero. The rationale is to detect the precession of net magnetization around the x or y axis due to the spin-locking field, and use this information to infer its amplitude. The following protocol can be used for calibration:

1. Select a sharp and well-resolved resonance for calibration that exhibits minimal or no chemical exchange to avoid complications from exchange processes. For experiments with nucleic acids, it is preferable to perform ^{13}C calibration using A-C8 or G-C8 spins as they permit the use of spin-lock amplitudes as low as ~50 Hz (Table 1).

2. Compile a table containing $\omega_1/2\pi$ values (in Hz) to be calibrated and associated power levels P (in dB). For $^{13}C/^{15}N$ calibration, we choose 24 $\omega_1/2\pi$ values between 50 and 3600 Hz and 50 and 2000 Hz respectively. The power levels P for each spin-locking field can initially be estimated based on the calibration of rectangular 90° pulse lengths for ^{15}N or ^{13}C.

3. Record 1D experiments for an array of spin-lock durations T_{relax} under on-resonance conditions for each ω_1 value. Usually, 33 durations are used in increments of $\pi/(2\omega_1)$ from 0 to $8*2\pi/\omega_1$ s[21]. For example, a spin-lock amplitude $\omega_1/2\pi$ of 100 Hz would be incremented 33 times from 0–80 ms in increments of 2.5 ms. This ensures that there are 4 points for one rotation of the net magnetization about the spin-locking field, enabling extraction of the frequency of rotation, in accordance with the Nyquist sampling theorem.

4. The resultant peak intensity should be a sinusoidal function of $\omega_{1,real} T_{relax}$ where $\omega_{1,real}$ is the real spin-lock frequency corresponding to the power P (Fig. 30A). Calculate $\omega_{1,real}$ by fitting the peak intensities to the equation $I(T_{relax}) = I_0 exp(-R \cdot T_{relax}) cos(\omega_{1,real} T_{relax} + \phi)$, where I is the peak intensity, I_0 is the intensity when $T_{relax} = 0$, R is the relaxation rate and ϕ is a phase correction factor.

5. Repeat Step 2 and 3 for all ω_1 in the table, and obtain $\omega_{1,real}$ for all P values.

6. Fit P and $\omega_{1,real}$ to a logarithmic equation $P = a log_{10}(\omega_{1,real}) + b$. Ideally this fit should give $R^2 > 0.99$. If the data points deviate from linearity, polynomial fitting can be adopted instead. An example of an ideal calibration curve is shown in Fig. 30B.

7. Use the equation given by the fit in step 6 to back-calculate P for a desired ω_1 within the range of amplitudes used for calibration.

6. Data Analysis

Two general approaches can be used to analyze off-resonance $R_{1\rho}$ data to extract the exchange parameters (Fig. 29). The most general approach involves numerically integrating the B-M equations[45] to find exchange parameters that best satisfy the measured $R_{1\rho}$ data. A second approach to fit $R_{1\rho}$ data involves using algebraic expressions that make various assumptions and which are valid for different ranges of exchange conditions. The two approaches are often used hand in hand, with the algebraic expressions often being used to obtain initial guesses for the B-M fitting as well as for developing an intuitive understanding for how the RD profiles vary with spin-lock and exchange parameters.

6.1. Numerical integration of Bloch-McConnell equations

In the authors' group, we use an in-house python program called "Bloch-McConnell Numerical Simulator" or BMNS (available from https://github.com/alhashimilab/BMNS) to numerically integrate the B-M equations and thereby simulate or fit $R_{1\rho}$ data. The analysis described below is valid when the magnetization decay is dominated by a single exponential decay[13, 23]. In uncommon cases where the decay is not mono-exponential, one needs to

directly fit it by integrating the B-M equations, without extracting $R_{1\rho}$. BMNS takes the following parameters as input:

1. List of Ω, ω_1, $R_{1\rho}$ and the uncertainty of $R_{1\rho}$ (see Section 6.3).
2. Initial guesses for the exchange parameters (p_{ES1}, p_{ES2}, k_{ex1}, k_{ex2}, $\Delta\omega_1$, $\Delta\omega_2$, $R_{2,GS}$, $R_{2,ES1}$, $R_{2,ES2}$, $R_{1,GS}$, $R_{1,ES1}$, $R_{1,ES2}$) for a given exchange topology as well as their ranges. For example, for three-state exchange, one has to specify whether the topology is star-like, linear, or triangular by appropriately setting individual rate constants to zero (Section 4.2). The initial guesses are typically either assigned arbitrarily and/or obtained from fitting the $R_{1\rho}$ data to an appropriate algebraic expression (Section 6.2). The ranges for the exchange parameters are typically chosen to be large to avoid biases. In general, fitting the RD data is carried out assuming $R_{1,GS} = R_{1,ES}$ and $R_{2,GS} = R_{2,ES}$ unless there is reason to suspect otherwise. Note that deviations from the latter assumption can result in significant errors in the fitted p_{ES} and k_{ex} values even when $|R_{2,GS}-R_{2,ES}| << k_{ex}$[190].
3. The initial alignment of the magnetization. For slow exchange, the magnetization is initially aligned along $\boldsymbol{\omega_{eff,GS}}$ (GS alignment), while more typically, for fast and intermediate exchange, the magnetization is aligned along $\boldsymbol{\omega_{eff,AVG}}$ (AVG alignment). If not known *a priori*, the mode of alignment can be determined during the fitting procedure based on the value of $k_{ex}/|\Delta\omega|$; with $k_{ex}/|\Delta\omega| \leq 1$ and $k_{ex}/|\Delta\omega| > 1$ corresponding to GS and AVG alignments, respectively. We recommend fitting RD profiles assuming both possible alignments for completeness. For low $p_{ES,}$ the choice of alignment has little effect on fitting $R_{1\rho}$ data. However, for intermediate to fast exchange ($0.1 < k_{ex}/\Delta\omega < 5$), with high p_{ES} (> 10%), a line shape analysis shows that the observed peak is actually neither at $\omega_{0,GS}$ nor at $\omega_{0,AVG}$ (Fig. 31A). Thus, calculation of effective fields assuming GS or AVG alignments leads to asymmetries in the RD profile around Ω = 0, that are especially pronounced at low ω_1, when deviations in Ω can have a large influence on the effective field orientations (Fig. 31B, 31C). This artifact can be corrected by selecting an initial magnetization alignment based on line shape simulations, and then adjusting the effective fields to take this into account (Eqn. 37, 39). This also enables determination of the effective fields and alignment directions for any arbitrary set of exchange parameters. Temperaturedependent $R_{1\rho}$ measurements can also be used to deduce the alignment scheme when both schemes equally fit the data well, as described in Section 6.4.3. Each of the above inputs can be specified for individual $R_{1\rho}$ data sets measured on multiple spins, which can also be fit globally using shared parameters.

Fitting of the $R_{1\rho}$ data is then carried out through least-squares minimization of the function F that quantifies the agreement between the experimentally measured $R_{1\rho}$ data $\left(R_{1\rho(i)}^{exp}\right)$ and values calculated $\left(R_{1\rho(i)}^{Calc}\right)$ using the B-M equations for a given set of exchange parameters and a user-specific exchange topology:

$$F = \frac{\chi^2}{2} \quad (56)$$

$$\chi^2 = \sum_{i=1}^{N} \left(\frac{R_{1\rho(i)}^{Calc} - R_{1\rho(i)}^{exp}}{\sigma_{exp(i)}} \right)^2 \quad (57)$$

$\sigma_{exp(i)}$ is the experimental uncertainty in $R_{1\rho}$ (estimated using Monte-Carlo or bootstrap approaches outlined in Section 6.3) and the summation i is over the total number of $R_{1\rho}$ data points N (total number of combinations of spin-lock amplitudes and offsets).

The initial guesses for the exchange parameters are used as input to predict the $R_{1\rho}$ data by using the B-M equations (Section 4.1). This involves numerically integrating the B-M equations to determine M_{GS} and M_{ES} as a function of time, and then fitting the projection of the net magnetization along $\boldsymbol{\omega_{eff,OBS}}$ (depending on the initial alignment of the magnetization) to determine $R_{1\rho}$. The χ^2 value is then computed and a second iteration is attempted choosing different values for the exchange parameters from the user defined range, in a manner that minimizes the χ^2, using least-squares minimization[225]. BMNS uses a Trust Region Reflective algorithm for this purpose. This process is repeated iteratively until a local minimum is found. To minimize computational cost and also avoid being trapped in local minima in the multidimensional parameter space during least-squares minimization, an adaptive memory programming framework[226] for global space optimization can be used. Here, once a local minimum is found, the search function tunnels out of this local minimum and resumes optimization from a new starting point. Alternatively, a brute force grid search over the multidimensional parameter space can also be performed, although it is computationally expensive.

The goodness of the fit is evaluated by normalizing the computed χ^2 values to take into account the degrees of freedom to obtain a reduced χ^2 ($\chi^2 red$), so as to enable comparisons between different exchange models:

$$\chi^2 red = \frac{\chi^2}{N - K} \quad (58)$$

where N is the total number of $R_{1\rho}$ data points and K the number of fitted parameters for a given exchange model. In general, a value $\chi^2 red < 1.5$ is considered to be reasonable though care should be taken if a fit gives $\chi^2 red < 1$ as this may indicate over-fitting of the data. Convergence of the fitted exchange parameters when starting with different initial guesses can also be used to assess the robustness of the fit. The different exchange models (two-state versus three-state star-like/triangular/linear) and fitting modes (individual versus global) used in the B-M fitting are evaluated for statistical significance using Akaike information (AIC) and Bayesian information (BIC) criteria[227, 228] (Fig. 29). They quantify the

likelihood or probability of one model relative to another for fitting a given data set, by taking into account the goodness of fit and the complexity or degrees of freedom of the models:

$$AIC\ weight = \frac{\exp(-0.5\Delta AIC)}{1+\exp(-0.5\Delta AIC)} \quad (59)$$

$$BIC\ weight = \frac{\exp(-0.5\Delta BIC)}{1+\exp(-0.5\Delta BIC)} \quad (60)$$

where ΔAIC and ΔBIC denote the differences in AIC and BIC values between the models. The AIC and BIC values themselves are defined as follows:

$$AIC = \begin{cases} N\ln\left(\frac{RSS}{N}\right)+2K, & where\ \frac{N}{K} \geq 40 \\ N\ln\left(\frac{RSS}{N}\right)+2K+\frac{2K(K+1)}{N-K-1}, & where\ \frac{N}{K} < 40 \end{cases} \quad (61)$$

$$BIC = N\ln\left(\frac{RSS}{N}\right)+K\ln(N) \quad (62)$$

where $RSS = \Sigma_{i=1}^{N}\left(R_{1\rho(i)}^{Calc} - R_{1\rho(i)}^{exp}\right)^2$ is the residual sum of squares for a given exchange model. Degeneracies can arise near under particular exchange scenarios that can make it difficult to reliably determine all exchange parameters. Near the fast exchange limit ($k_{ex}/\Delta\omega > 10$), it becomes difficult to reliably separate Δω from p_{ES} as R_{ex} becomes proportional to $p_{ES}\Delta\omega^2$[13, 196]. Under slow exchange conditions, there are also degeneracies in resolving p_{ES} and k_{ex} as R_{ex} becomes proportional to $p_{ES}k_{ex}$[229, 230].

6.2. Algebraic equations

Algebraic expressions that make various approximations can also be used to fit the variations of off-resonance $R_{1\rho}$ with ω_1 and Ω to extract the desired exchange parameters (reviewed in Massi *et al.*[13]). They give a better understanding of the dependence of $R_{1\rho}$ on the exchange parameters relative to the B-M equations. These expressions assume that the decay of the magnetization is mono-exponential. The most versatile expression for two-site chemical exchange is given by the following equation derived from a Laguerre approximation[231] and more recently via perturbation theory applied to an *n*-site BM evolution matrix[194]:

$$R_{1\rho} = R_1 cos^2\theta + R_2 sin^2\theta + \frac{sin^2\theta p_{GS} p_{ES} k_{ex} \Delta\omega^2}{\left\{\omega^2_{eff,GS}\omega^2_{eff,ES}/\omega^2_{eff,AVG} + k^2_{ex} - sin^2\theta p_{GS} p_{ES}\Delta\omega^2\left(1 + \frac{2k^2_{ex}\left(p_{GS}\omega^2_{eff,GS} + p_{ES}\omega^2_{eff,ES}\right)}{\omega^2_{eff,GS}\omega^2_{eff,ES} + \omega^2_{eff,AVG}k^2_{ex}}\right)\right\}} \quad (63)$$

$$\theta = tan^{-1}\left(\frac{\omega_1}{\Omega_{AVG}}\right) \quad (64)$$

The Laguerre equation is valid under conditions of fast exchange, and deviations can arise for slow to intermediate exchange when $p_{ES} > 30\%$ especially for low spin-lock amplitudes (< 400 Hz)[9, 231]. This results from the fact that the Laguerre equation assumes AVG alignment.

Simpler expressions have also been derived that entail the use of alternative approximations[13]. An expression for $R_{1\rho}$ valid for very asymmetric populations ($p_{ES} << p_{GS}$) for arbitrary chemical shifts is given below:

$$R_{1\rho} = R_1 cos^2\theta + R_2 sin^2\theta + \frac{sin^2\theta p_{GS} p_{ES} k_{ex} \Delta\omega^2}{\Omega^2_{ES} + k^2_{ex} + \omega^2_1} \quad (65)$$

while an alternative expression that is valid only in the fast exchange limit ($k_{ex} >> \Delta\omega$) for arbitrary populations is given by[63, 189]:

$$R_{1\rho} = R_1 cos^2\theta + R_2 sin^2\theta + \frac{sin^2\theta p_{GS} p_{ES} k_{ex} \Delta\omega^2}{k^2_{ex} + \omega^2_1 + \Omega^2_{AVG}} \quad (66)$$

The two equations above can be used to fit off-resonance data; however, deviations can arise under conditions when the assumptions inherent to the equations are not satisfied.

For three-state exchange without direct “minor” exchange between ES1 and ES2 (ES2⇌GS⇌ES1), one can use the following equation[193]:

$$R_{1\rho} = R_1 cos^2\theta + R_2 sin^2\theta + sin^2\theta\left(\frac{k_1\Delta\omega^2_1}{\Omega^2_{ES1} + \omega^2_1 + k^2_{-1}} + \frac{k_2\Delta\omega^2_2}{\Omega^2_{ES2} + \omega^2_1 + k^2_{-2}}\right) \quad (67)$$

where k_1 and k_{-1} are the GS⇌ES1 forward and reverse rate constants, and k_2 and k_{-2} are the GS⇌ES2 forward and reverse rate constants, respectively. From the equation, it can be appreciated that the exchange contribution for a star-like three-state topology is essentially the sum of exchange contributions due to the individual two-state processes as described in Section 4.2.2. Expressions for three-state exchange with significant minor exchange have also been reported[193]. These equations have been generalized to *n*-site exchange for star-like, complex linear, and non-linear topologies by Palmer *et al.*[194]. All the above equations assume that R_2 results from a population-average over all ES and GS species. Algebraic expressions for $R_{1\rho}$ for cases where R_2 for the GS and ES are not equal have also been reported in the literature[187, 202].

When fitting $R_{1\rho}$ data using the above equations, one starts with broad initial estimates for the exchange parameters and optimizes initial guesses to achieve agreement with the experimental data. However, biased starting estimates coupled with conventional local optimization methods can lead to being trapped in local minima. In such cases, the use of simulated annealing and basin-hopping schemes[226] can prove beneficial for finding global minima and for exploring the search space more broadly.

χ^2_{red} values can be used to assess the quality of fit as described in Section 6.1. A poor fit may suggest deviations from the assumed exchange model or from the range of validityof the algebraic equations used. Once again, statistical tests (e.g. AIC and BIC weights)[227, 228] can be used to assess the likelihood of one model or exchange topology over the other.

6.3. Estimating uncertainties in exchange parameters

Uncertainty in the fitted exchange parameters can be estimated using the standard error of the fit, as well as bootstrap and Monte Carlo based approaches[196]. A parent set of $R_{1\rho}$ rates (Ω, ω_1, $R_{1\rho}$ and σ) is used for all methods. The standard error of a fit can be obtained as the square root of the diagonal elements of the covariance matrix of the fitted parameters.

In the bootstrap approach:

1. A large number (typically 500–1000) child data sets of the same size as the parent data set are generated by randomly sampling $R_{1\rho}$ data points with replacement from the parent data set. Here, an individual data point can be either excluded or chosen multiple times in a given child data set.
2. Each child data set and the parent data set are fit to the Laguerre[231] or B-M equations to obtain the five exchange parameters: p_{ES}, k_{ex}, $\Delta\omega$, R_1 and R_2.
3. The uncertainty in the exchange parameters is then determined by calculating the standard deviation between the fitted parameters of the child data sets and those of the parent data set.

In the Monte Carlo approach:

1. The parent data set is fit to the Laguerre equation[231] or B-M equations[45] to obtain the exchange parameters.

2. 1000 child data sets are generated using the exchange parameters and the Laguerre or B-M equations, and the associated Ω and ω_1 values of the parent data set. Each child data set is then corrupted by noise according to the $R_{1\rho}$ error from the parent data set and re-fitted using the Laguerre equation or B-M integration.

3. The uncertainty in the exchange parameters is then determined by calculating the standard deviation between the fitted parameters of the child data sets and those of the parent data set.

Similar methods can also be used for determination of errors in $R_{1\rho}$ for each ω_1 and Ω combination while fitting the mono-exponential decays.

6.4. Extracting exchange parameters

6.4.1. Deducing the total number of excited states—Early on, it is important to deduce the total number of ESs sensed by the $R_{1\rho}$ measurements as this influences the models used in fitting the data. Deviations from symmetric RD profiles expected for two-state exchange, and the appearance of more than one RD peak is an indication of additional ESs as described for three-state exchange in Figure 24. In addition, different spins in a molecule may sense different ESs. To gauge such cases, the $R_{1\rho}$ data measured for the spins are initially subjected to B-M fitting individually. A plot of k_{ex} versus p_{ES} for the different spins is then examined to identify the total number of distinct ESs. A representative k_{ex} vs. p_{ES} plot for HIV-1 TAR shows clusters at two distinct locations consistent with two ESs (Fig. 32). Whether or not global fitting of the data with a common p_{ES} and k_{ex} is statistically justified also provides a means of gauging the total number of ESs.

6.4.2. Deducing the chemical shifts of the excited states—The chemical shift of the ES ($\omega_{0,ES}$) can be calculated from the Δω value obtained from fitting the RD data and peak position ($\omega_{0,OBS}$) measured from a 2D HSQC spectrum. For intermediate-slow exchange with $k_{ex}/\Delta\omega < 1$, the initial alignment of the magnetization is along $\boldsymbol{\omega_{eff,GS}}$ (Section 6.1) and $\omega_{0,ES}$ is given by:

$$\omega_{0,ES} = \omega_{0,GS} + \Delta\omega \quad (68)$$

For intermediate-fast exchange $k_{ex}/\Delta\omega > 1$ for which the initial alignment of the magnetization is along $\boldsymbol{\omega_{eff,AVG}}$ (Section 6.1), $\omega_{0,ES}$ can be calculated using:

$$\omega_{0,ES} = \omega_{0,AVG} + p_{GS}\Delta\omega \quad (69)$$

Note that for special exchange scenarios such as intermediate to fast exchange ($0.1 < k_{ex}/\Delta\omega < 5$) with high $p_{ES} > 10\%$ (Section 6.1), $\omega_{0,OBS}$ does not correspond to either $\omega_{0,AVG}$ nor $\omega_{0,GS}$. Here, line shape simulations under free precession assuming the fitted exchange parameters with $\omega_{0,GS} = 0$ and $\omega_{0,ES} = \Delta\omega$ are used to estimate the shift (ψ) in resonance frequency due to the exchange and obtain $\omega_{0,ES}$:

$$\omega_{0,ES} = \omega_{0,OBS} - \Psi + \Delta\omega \quad (70)$$

6.4.3. Obtaining kinetic and thermodynamic parameters—Kinetic and thermodynamic parameters that provide important insights into the energetics of the ES and transition state (TS) can be derived from the exchange parameters[15, 17]. The free energy difference between the ES and GS ($\Delta G_{ES\text{-}GS}$) at a given temperature can be obtained from the measured p_{ES} and p_{GS} using the following equation:

$$\Delta G_{ES-GS}(T) = -RTln\left(\frac{p_{ES}}{p_{GS}}\right) \quad (71)$$

The activation barrier for the forward $\left(\Delta G_1^{\ddagger}(T)\right)$ or reverse $\left(\Delta G_{-1}^{\ddagger}(T)\right)$ reaction and the corresponding enthalpies ($\Delta H_1^{\ddagger}$ and $\Delta H_{-1}^{\ddagger}$) can be obtained from temperature-dependent $R_{1\rho}$ measurements using the following equation derived by Russu *et al.*[232] that is free of statistical compensation effects and is valid if the specific heat capacity can be assumed to be constant:

$$\ln\left(\frac{k_i(T)}{T}\right) = ln\left(\frac{k_B\kappa}{h}\right) - \frac{\Delta G_i^{\ddagger}(T_{hm})}{RT_{hm}} - \frac{\Delta H_i^{\ddagger}}{R}\left(\frac{1}{T} - \frac{1}{T_{hm}}\right) \quad (72)$$

$$T_{hm} = n\left(\sum_{i=1}^{n}\left(\frac{1}{T_i}\right)\right)^{-1} \quad (73)$$

where $i = 1$ or -1 and T_{hm} is the harmonic mean of the experimental temperatures used. The transmission coefficient κ is often assumed to be equal to 1. This assumes that the frequency of crossing the activation barrier can be approximated by $\frac{k_BT}{h}$, which is valid for the case of a bond vibration. However, as noted by Kay *et al.*, this frequency may be different in the context of conformational changes in biomolecules[233]. Indeed, taking this into account by adjusting the value of κ to be different from 1 can have a large impact on the obtained free energies of activation. For example, assuming $\kappa = 3.3 * 10^{-6}$ as determined by Kay *et al.* for transitions involving formation of ESs in proteins[233] can change the free energies of activation for Watson-Crick to Hoogsteen transitions by as much as 7 kcal/mol (or 29 kJ/mol) (Fig. 33). In contrast, the enthalpies for the forward and backward reactions do not depend on κ and therefore can be reliably extracted from temperature-dependent rate constants obtained from RD measurements. The free energies and enthalpies obtained as described above can be used to obtain the entropy ($\Delta S_1^{\ddagger}$ and $\Delta S_{-1}^{\ddagger}$) of activation for the forward and reverse reactions:

$$T_{hm}\Delta S_i^{\ddagger} = \Delta H_i^{\ddagger} - \Delta G_i^{\ddagger}(T_{hm})\ \#\quad (74)$$

While performing $R_{1\rho}$ RD measurements as a function of temperature, accurate estimates for the sample temperature can be obtained by recording spectra of 99.8% methanol-d_4 (Cambridge Isotope Laboratories, Inc.) as described by Berger *et al.*[234]. The enthalpy (ΔH_{ES-GS}) and entropy (ΔS_{ES-GS}) change for the GS-ES transition can also be calculated as follows:

$$\Delta H_{ES-GS} = \Delta H_{-1}^{\ddagger} - \Delta H_{1}^{\ddagger}\ \#\quad (75)$$

$$\Delta S_{ES-GS} = \Delta S_{-1}^{\ddagger} - \Delta S_{1}^{\ddagger}\ \#\quad (76)$$

The temperature dependence from a van't Hoff analysis can also be used to discriminate between GS versus AVG alignment during B-M fitting[235], in cases where the initial magnetization alignment is ambiguous, and both schemes fit the data equally well. A van't Hoff plot of $\ln(k_1/\mathrm{T})$ (or k_{-1}) versus $(1/T - 1/T_{hm})(\mathrm{K}^{-1})$ (Eqn. 72 and 73) is expected to exhibit linearity if the correct magnetization alignment scheme is assumed, provided that it does not change as a function of temperature. Such an analysis was used to select AVG over GS alignment while fitting RD profiles by Al-Hashimi *et al.*[235].

In addition to obtaining insights into the thermodynamics of transition states and their kinetics, RD methods can also be used for structural characterization of the TS via ϕ value analysis[115, 236] or measurement of kinetic isotope effects for exchange processes[237].

7. Determining structures of excited states in nucleic acids

The biological significance of an exchange process cannot be fully appreciated without determining the structure of the ES. RD experiments provide structural information regarding the ES in the form of chemical shifts. Here, we review how chemical shifts, combined with methods for stabilizing or destabilizing ESs using mutagenesis and chemical modifications, as well as computational approaches for predicting chemical shifts and nucleic acid structures, can be used to determine structures for nucleic acid ESs at various degrees of resolution. These approaches are generally applicable, and can be used in conjunction with CPMG and CEST experiments as well.

7.1. Inferring base pairing and secondary structure from chemical shift fingerprints

Most if not all ESs in nucleic acids characterized to date involve changes in base pairing or secondary structure. The need to break one or two BPs during the transition explains why they occur on the slow micro-to-millisecond timescale. The set of chemical shifts measured for a given ES constitutes a 'fingerprint', which can be used to infer various aspects of its

base pairing and secondary structure. Key to this approach are recent improvements in our understanding of chemical shift-structure relationships in nucleic acids (reviewed in Chi *et al.*[238]). The ^{13}C chemical shifts primarily depend on the base and sugar conformation[239–248], whereas the ^{15}N chemical shifts primarily report on base pairing and hydrogen bonding[240, 249–255], respectively. Below, we review how these dependencies of chemical shifts on structure give rise to chemical shift fingerprints that can aid structural elucidation of nucleic acid ESs.

Nucleic acids are primarily composed of canonical Watson-Crick A-T/U and G-C BPs in A-form RNA and B-form DNA helices, respectively. G-C and A-T/U Watson-Crick BPs that are sandwiched between other Watson-Crick BPs have characteristic ^{13}C and ^{15}N chemical shifts that fall within a narrow spectral region[9], owing to their well defined and regular geometry characterized by canonical values for the backbone torsion angles (*anti* χ, α~300°, β~180°, γ~60°, ε~210°, ζ~270°) and sugar pucker (C3′-endo in RNA & primarily C2′-endo in DNA) (Fig. 34A). These chemical shift fingerprints can readily be used to infer whether transitions toward an ES entail creation or loss of Watson-Crick BPs.

On the other hand, nucleotides not involved in Watson-Crick pairing have chemical shifts that differ from canonical Watson-Crick BPs for at least a subset of ^{13}C and ^{15}N spins. For example, Hoogsteen BPs such as G(*syn*)-C$^+$(*anti*), A(*syn*)-T/U(*anti*), and G(*syn*)-G(*anti*), G(*syn*)A$^+$(*anti*) and G(*anti*)-A(*syn*) have $\Delta\overline{\omega}_{C1}$ and $\Delta\overline{\omega}_{C8}$ values for the *syn* nucleotide, that are shifted downfield by 1 – 4 ppm relative to Watson-Crick BPs[17, 235]. Furthermore, many mismatches such as A(*anti*)$^+$-C(*anti*), A(*anti*)$^+$-G(*syn*), G(*syn*)-C$^+$(*anti*), and C(*anti*)-C(*anti*)$^+$ have protonated bases with $\Delta\overline{\omega}_{A-C2}\sim -8$ ppm, $\Delta\overline{\omega}_{A-C8}\sim -4$ ppm, $\Delta\overline{\omega}_{C-C6}\sim -2.5$ ppm, and $\Delta\overline{\omega}_{C-N4}\sim -10$ ppm relative to their non-protonated counterparts[17, 235, 253, 256]. Rare tautomeric and anionic forms of the bases which occur for example in Watson-Crick-like mismatches such as G^{enol}-T/U, GT^{enol}/U^{enol} and G-T$^-$/U$^-$[257], feature $\Delta\overline{\omega}_{G-N1}$ and $\Delta\overline{\omega}_{T/U-N3}\sim 50$ ppm, and $\Delta\overline{\omega}_{G-C8}$ and $\Delta\overline{\omega}_{T/U-C6}\sim 2$ ppm relative to bases in their canonical tautomeric and ionic forms[165, 195, 197]. The imino ^{15}N chemical shifts are also sensitive to changes in base pairing, with upfield shifts in T/UN3 and G-N1 occurring upon transitions of Watson-Crick A-T/U or G-C BPs to mismatches such as T/U-G, T/U-T/U and G-T/U[9] (Fig. 34B). Unpaired nucleotides in DNA and RNA also have characteristic chemical shifts relative to their duplex counterparts, particularly for the sugar ^{13}C (C1′, C3′, and C4′) due to changes in sugar pucker[166, 239, 244–247] away from canonical C2′endo and C3′-endo geometries respectively (see below) as well as 1D6D8 angles. This may also be accompanied by changes in the base ^{13}C chemical shifts (C6/C8) due to changes in stacking and χ angle[239–243].

In general, C3′-endo sugars in RNA helices have downfield shifted $\omega_{C1'}$ and upfield shifted $\omega_{C4'}$ relative to C2′-endo sugars, which typically occur in non-helical residues such as in bulges, and which tend to have upfield shifted $\omega_{C1'}$ and downfield shifted $\omega_{C4'}$[166, 240, 242, 244, 247] (Fig. 34C). In RNA, changes in sugar pucker are frequently accompanied by coupled changes in χ angle[258] that also influence $\omega_{C1'}$. In some cases, these changes can be compensatory leading to small changes in $\omega_{C1'}$, and consequently, to a lack of observable RD[166]. This shows how the absence of detectable RD for a particular spin cannot be taken

as evidence for the absence of chemical exchange. This also underscores the importance of characterizing the conformation of the ES using as many chemical shift probes as possible, in addition to highlighting potential pitfalls of inferring structural changes based on a limited set of RD measurements. In DNA, C3′-endo sugars have $\Delta\overline{\omega}_{C3'} \sim -7$ ppm and $\Delta\overline{\omega}_{C4'} \sim -2.5$ ppm relative to C2′-endo sugars[239, 240, 245, 246].

$R_{1\rho}(^1H)$ experiments[222] make it possible to measure ^1H chemical shifts that provide information regarding the ES structure that is complementary to ^{13}C and ^{15}N chemical shifts. Proton chemical shifts are sensitive to ring-currents and magnetic anisotropy effects and therefore stacking and χ angles[238]. When combined with empirical tools to predict ^1H chemical shifts based on structure[259–261] and sequence[262, 263], it is likely that proton chemical shifts will be extensively used in the future to help determine the structures of nucleic acid ESs.

Based on the above chemical shift-structure relationships, chemical shift fingerprints (Fig. 35A) can be used to obtain insights into structural features of ESs, and guide the development of structural models for the ES, which can range from localized changes in pairing at an individual BP, to more concerted changes in base pairing that lead to changes in secondary structure as is often observed in RNA[16, 264]. Inferring possible structures for such RNA ESs is greatly aided by secondary structure prediction programs such as Mfold[265] and MC-Fold[266], which can be used to generate a list of putative ES secondary structures ranked according to their predicted free energies[16, 264]. While the lowest energy structures typically correspond to the GS, RNA ESs frequently appear as higher energy structures that form through reshuffling of at least one BP. These putative ES structures are examined for their ability to explain the observed chemical shift fingerprints at sites where conformational changes occur, as well as the absence of RD at sites where little or no conformational change is expected.

7.2. Using chemical and environmental perturbations to determine the structure and function of excited states in nucleic acids

Once generated, a putative ES model is subjected to experimental tests. This involves testing predictions about the impact of mutations, modifications or changes in experimental conditions that bias the system toward or away from the ES. These predictions are then tested experimentally using chemical shift or RD measurements. As ESs are typically destabilized relative to the GS by < 4 kcal/mol or 17 kJ/mol, it often proves feasible to invert the GS-ES equilibrium and achieve $p_{ES} > 50$ % through single nucleotide or atom substitutions[16, 31, 116, 264, 267, 268]. This can be achieved by stabilizing the ES, destabilizing the GS, or both.

7.2.1. Stabilizing the excited state relative to the ground state by mutations or chemical modifications—

If a putative ES model is accurate, one would predict that a mutation or modification stabilizing an ES would cause changes in chemical shifts throughout the RNA at sites with significant RD, resulting in chemical shifts for the mutant that are similar to those measured for the ES using RD measurements in the parent wild-type RNA. Equally important, the mutation/modification should minimally induce changes in

chemical shifts for sites that do not show any RD. In addition to verifying the putative ES model, mutations/modifications provide a means by which to verify whether or not an exchange process involving multiple spins is indeed concerted. This is important because similar p_{ES} and k_{ex} amongst various spins cannot be taken as definitive evidence for a concerted exchange process as various segments in a molecule may undergo transitions independently, yet have similar exchange parameters by chance. In the latter case, one would expect that mutations/modifications would lead to local stabilization of a given segment without affecting other segments. On the other hand, for a cooperative process, the mutation/modification would affect spins in multiple segments. In this manner, mutations and modifications can provide insights into the cooperativity of conformational transitions.

A general strategy for stabilizing the ES relative to the GS is to convert non-canonical mismatches unique to the ES into more stable canonical Watson-Crick BPs while simultaneously converting canonical Watson-Crick BPs in the GS into non-canonical mismatches[9, 16, 264]. For example, in HIV-1 TAR, an ES could be stabilized by a G28U point substitution mutation, which replaces the G28-A35 BP in the ES with a more stable U28-A35 BP while at the same time replacing the G28-C37 BP in the GS with a less stable U28-C37 BP[264] (Fig. 35B, 35C). 2D NOESY-based distances confirm that the G28U mutant folds into the predicted ES2-like secondary structure[264]. The chemical shifts measured for the G28U mutant were found to be in good agreement with those measured for ES2 in HIV-1 TAR using $R_{1\rho}$ (Fig. 35D). In addition, only small differences in chemical shifts were observed for several sites that do not show any RD (e.g. U42-N3 and A22-C8) [264]. The fact that a single point substitution mutation in the upper helix changed the conformation of remotely positioned nucleotides in the bulge such as U23, provides independent support for a concerted transition, in which all BPs are reshuffled in going from the GS to ES2.

ES structures can also be stabilized using commercially available chemical modifications. For example, the definitive confirmation that a Hoogsteen BPs in duplex DNA was the ES detected by $R_{1\rho}$ came with the use of N^1-methyl adenosine (m^1A) and N^1-methyl guanosine (m^1G) modifications, to induce Hoogsteen BPs at specific sites within DNA duplexes[17, 116]. m^1A and m^1G sterically block Watson-Crick type hydrogen-bonding and knock out one hydrogen bond in the Watson-Crick BP without significantly affecting the stability of the Hoogsteen BP (Fig. 35E). The modified nucleotides formed the expected Hoogsteen BPs as verified by 2D NOESY without affecting Watson-Crick base pairing at neighboring sites, which is expected if the Watson-Crick to Hoogsteen transitions occur independently of one another[17, 116]. The chemical shifts of the m^1A and m^1G modified duplexes were in excellent agreement with those measured by RD on the C1′ and C6/C8 atoms, and Density Functional Theory (DFT) calculations[17]. Moreover, the m^1A and m^1G mutants revealed that other resonances should experience large chemical shift perturbations due to formation of Hoogsteen BPs, including upfield shifted ^{15}N signals in imino guanine-N1 and thymine-N3, due to changes in hydrogen bonding[112], and changes in sugar ^{13}C signals (adenine and guanine C3′ and C4′, and thymine and cytosine C3′) indicative of changes in sugar pucker[117]. These predictions were confirmed in subsequent studies in which $R_{1\rho}$ RD were used to measure the ES chemical shifts at these new sites[112, 117]. Once again, no RD was

observed for ^{13}C signals (e.g. thymine and cytosine C4′) showing small chemical shift perturbations in the m^1A and m^1G mutants[117].

An ES stabilizing mutant is not expected to reproduce all ES chemical shifts, especially for residues near the mutation site, and in many cases more than one mutant will be required to verify different aspects of the ES structure[16, 264]. Returning to the G28U mutant mimic of ES2 in TAR, differences as large as 1.5 ppm for C1′ and N1 were observed near the site of the mutation[264] (Fig. 35D). As this mutant replaces tandem G-A mismatches in ES2 with a single G-A mismatch and a Watson-Crick BP, it is likely to alter the structure around these sites. Much better agreement for the G-A mismatch chemical shifts was obtained with a second mutant ($ES2^{uucg}$) that retains the tandem G-A mismatches[269] (Fig. 35B, D). Likewise, in the case of ES Hoogsteen BPs, the m^1A modification introduces a positive charge to the base, and consequently, the m^1A-C8 chemical shift was downfield-shifted more significantly than in the ES Hoogsteen BP[17, 116]. The A-C8 chemical shifts measured for an A-T Hoogsteen BPs stabilized using a drug were found to be in better agreement with those measured by RD[17, 270].

7.2.2. Destabilizing the excited state relative to the ground state by mutations or chemical modifications—Putative ES models can also be tested by introducing mutations or modifications that are predicted to destabilize the ES relative to the GS, reducing p_{ES}, or even making the ES invisible to RD detection. Returning to the TAR example, ES2 could be destabilized by replacing the wild-type apical loop with a UUCG apical loop (Fig. 36A). This mutation quenched RD at all sites sensitive to ES2 including sites within the bulge that are distant from the mutation site[264].

The chemical modification N^6,N^6-dimethyl substituted adenine ($m^{6,6}A$), which blocks interactions of adenine at the Watson-Crick face was used to disrupt an A-C mismatch that forms in TAR ES1 (Fig. 35B), favoring instead the conformation where adenine bulges out as observed in the GS[16] (Fig. 36B). As ES1 is in fast exchange and is highly populated (p_{ES} = 13 %), the $m^{6,6}A$ mutant showed perturbations in the chemical shifts towards the GS at sites showing RD for ES1[16].

Destabilizing a putative ES structure also provides a powerful strategy to test hydrogen bonding that is unique to the ES. For example, if Hoogsteen BPs in DNA were indeed stabilized by hydrogen bonds involving purine-N7, replacement of N7 with C7 (N7-deaza-purines, c7A and c7G) should significantly destabilize the BP[112] (Fig. 36C). Indeed, N7-deaza-purines quenched Watson-Crick to Hoogsteen RD in DNA selectively at the modified BP without affecting Watson-Crick to Hoogsteen exchange at neighboring sites[112]. As a second example, inosine was used to show that ES Watson-Crick-like G-T mismatches were hydrogen bonded in a Watson-Crick-like fashion[165] (Fig. 36D). Removal of the exocyclic amino group was predicted to destabilize ES Watson-Crick-like mismatches by 1–2 kcal/mol or 4–8 kJ/mol, pushing them beyond the limit of detection of $R_{1\rho}$ RD experiments, as was verified experimentally[165].

7.2.3. Stabilizing the ground or excited states by changing experimental conditions—Changing pH or temperature provides an alternative means for testing

putative ES models. Many ESs feature the formation of BPs that are stabilized by base protonation or deprotonation such as A^+(*anti*)-C(*anti*), A^+(*anti*)-G(*syn*), and G(*syn*)-C^+(*anti*), while examples of deprotonated BPs include Watson-Crick-like G-T^-/U^- mismatches. Insights into the appearance or loss of such BPs upon formation of an ES can be obtained from pH-dependent RD measurements. For example, in the case of TAR ES1, decreasing the pH increased the population of ES1, supporting the interpretation that ES1 contained a protonated A^+-C BP[16]. The pH dependence of RD measurements was also used to resolve anionic Watson-Crick-like G-T^- (in DNA) and G-U^- (in RNA) mismatches from their tautomeric counterparts (G^{enol}-T/U and G-T^{enol}/U^{enol}) based on the observed increase in p_{ES} with increasing pH (Section 8.2). In contrast, the population of the tautomeric ES (G^{enol}-T/U and G-T^{enol}/U^{enol}) was found to be independent of pH, consistent with a tautomeric species. Changes in pH were also used to stabilize the structure of an ES of U6RNA[135] and the Murine Leukemia Virus pseudoknot[267], both of which involved the formation of A-C^+ BPs.

Changing the temperature can also help to resolve RD contributions from two distinct exchange processes. For example, in the case of HIV-1 TAR, the R_{ex} contribution from a fast exchange process involving ES1 could be diminished by increasing the temperature, allowing better resolution of a second and slower exchange process involving ES2[264].

Lastly, for the case of exchange scenarios where one is monitoring binding equilibria, it is feasible to bias the equilibrium towards the bound or free conformation by altering the concentrations of the binding partners, so as to obtain their chemical shifts[32, 78, 79].

7.3. Solving high-resolution structures and dynamic ensembles for excited states in nucleic acids

Once validated, high resolution structures or dynamic ensembles can be obtained for a given ES-mutant and be used as high-resolution models for the ES conformation[117]. While this is a potentially general strategy for determining structures of ESs in nucleic acids, a number of precautions have to be taken. First, care must be taken to validate the mutant that stabilizes the ES using a large number of $R_{1\rho}$ measurements on a variety of spins. Second, the structure or dynamic ensemble of the ES mutant determined using NOEs and/or RDCs should be further validated for its ability to independently predict additional experimental data such as the ES chemical shifts.

The above approach has been applied to determine the first atomic resolution structure of a nucleic acid ES, in particular Hoogsteen BPs in two different DNA duplexes, using m^1A to stabilize the Hoogsteen conformation[117] (Fig. 35E). The m^1A mutant was validated based on the excellent agreement observed between its chemical shifts and those measured for the ES using RD for a variety of base and sugar spins (Fig. 37A). Dynamic structural ensembles (Fig. 37C) were determined for the m^1A-T mutants and the corresponding unmodified duplexes[116] using RDCs and computational molecular dynamics simulations[271–274]. An Automated Fragmentation Quantum Mechanics/Molecular mechanics approach[275] was then used to predict chemical shifts for every conformer in the ensembles of the m^1A-T mutant as well as the unmodified DNA[117]. The computed chemical shifts were averaged over the ensembles and the differences between the GS and ES chemical shifts thus

computed ($\Delta\omega_{Ens}$) were compared to values obtained using RD ($\Delta\omega_{RD}$). Excellent agreement was observed between the $\Delta\omega_{Ens}$ and $\Delta\omega_{RD}$ values (Fig. 37B), thus validating the generated ensembles. This also made it possible to rationalize the unique chemical shift signatures associated with the ES in terms of structural features[117].

The above strategy can in principle be extended to RNA, for which there is a growing number of tools for predicting $^{13}C/^{15}N$ chemical shifts based on 3D structures[259, 276]. In addition, even prior to the above study, methods had been developed to solve ES structures of proteins that involve measuring direct structural restraints, such as residual dipolar coupings (RDCs)[277–279], residual chemical shift anisotropies (RCSAs)[280], as well as paramagnetic relaxation enhancements (PREs)[281]. Building on these applications, CEST approaches have recently been developed to measure RDCs for nucleic acid ESs[170]. These approaches can readily be extended in the future to measure ES RCSAs in nucleic acids[282, 283]. These new types of data could be used in the future in conjunction with the mutation strategy described above to robustly determine structures and dynamic ensembles for nucleic acid ESs.

7.4. Using mutations to assess the biological functions of excited states in nucleic acids

Importantly, GS or ES stabilizing mutants can also be used in functional assays to assess the biological importance of the ES[16, 284]. For example, a mutation that destabilizes an ES in the HIV-1 Stem Loop 1 (SL1) was shown to impede duplex dimerization, implying that the ES plays a role for nucleating the transition[16]. More recently, ES-mutants of HIV-1 TAR were used in cell-based experiments to show that the non-native conformation disrupts transactivation[284]. Key to this assessment was the use of subsequent “rescue mutations” that push the ES-GS equilibrium to favor the GS; such mutations reinforce the fact that changes in conformation, rather than changes in sequence due to the mutations themelves, are responsible for the observed biological response.

8. Examples of applications of 1D selective $R_{1\rho}$ relaxation dispersion for the analysis of chemical exchange in nucleic acids

In this section, we review examples of applications of $R_{1\rho}$ RD to the study of chemical exchange in nucleic acids that illustrate the different types of motions characterized to date and their biological implications.

8.1. Watson-Crick to Hoogsteen exchange in DNA and RNA duplexes

As stated throughout this review, application of off-resonance $R_{1\rho}$ RD methodology resulted in the discovery that in the DNA double-helix, A-T and G-C Watson-Crick BPs continually undergo exchange with their Hoogsteen counterparts. Based on these studies, at any given point in time, ~1% and ~0.1% of A-T and G-C BPs in the DNA double helix are Hoogsteen rather than Watson-Crick BPs. This implies that at any given point in time, there could potentially be tens of millions of Hoogsteen BPs in the human genome. *In vivo*, DNA experiences supercoiling, torsional stress, under-winding, and stretching as it wraps around histones to form nucleosomes. Hoogsteen BPs could provide mechanisms for stabilizing such stressed structures of highly compacted DNA. Furthermore, in addition to the currently

known proteins such as p53 that bind to Hoogsteen BPs, other proteins may also promote or recognize Hoogsteen BPs when binding to DNA[114]. Indeed, drugs have been shown to bind duplex DNA and to induce dramatic changes in the Hoogsteen breathing dynamics[270]. We are today still in the early stages of examining the occurrence and biological significance of Hoogsteen BPs in DNA.

In sharp contrast to B-DNA, transient Hoogsteen BPs were not detected in A-RNA duplexes using $R_{1\rho}$ RD[235]. It was later shown that Hoogsteen BPs are less stable in A-RNA because *syn* purine bases are sterically disfavored in the A-form conformation, and because there is a greater energetic cost associated with constricting the backbone to form Hoogsteen type hydrogen bonds in A-RNA relative to that in B-DNA[285]. The markedly different propensities to accommodate Hoogsteen BPs in RNA and DNA duplexes is another important difference between the two nucleic acid polymers, in addition to the presence or absence of the 2′-hydroxyl group. The ability to absorb chemical damage at the Watson-Crick face by forming Hoogsteen BPs makes DNA a better custodian of genetic information and may represent one of the evolutionary pressures that resulted in B-DNA becoming the main carrier of genetic information in higher-order organisms[235]. On the other hand, the inability of A-RNA to accommodate Hoogsteen BPs explains how post-transcriptional modifications such as m^1A and m^1G can markedly influence RNA folding and function[235].

8.2. Exchange between wobble and Watson-Crick-like tautomeric and anionic G-T/U base pairs in DNA and RNA duplexes

Watson-Crick to Hoogsteen exchange converts canonical Watson-Crick G-C and A-T BPs into non-canonical Hoogsteen conformations. $R_{1\rho}$ studies have also uncovered an inverse process in which non-canonical G-T/U wobble mismatches are converted into canonical Watson-Crick-like BPs stabilized by rare tautomeric and anionic forms of the bases[165, 195, 197] (Fig. 38A). In contrast to Hoogsteen transitions, this exchange process occurs in both BDNA and A-RNA duplexes. By adopting conformations similar to Watson-Crick BPs, these ESs can evade fidelity checkpoints and contribute to errors during replication, transcription, and translation[286, 287]. These rare tautomeric bases were originally proposed as a potential source of replication errors by Watson and Crick in 1954, who outlined analogous tautomeric BPs in the case of the A-C mismatch[288].

A kinetic model for the generation of errors during DNA replication constructed using the rate constants of the formation of Watson-Crick-like BPs measured by NMR could predict the frequency of G-T mis-incorporation across a wide range of pH, polymerases, and modified mutagenic bases[195] (Fig. 38B). Likewise, the uridine 5-oxyacetic acid (cmo^5U) modification found in tRNA was recently shown to bias the G-cmo^5U ensemble toward anionic Watson-Cricklike conformations, potentially explaining how the modification “reprograms” translation[289]. Taken together, these studies suggest that Watson-Crick-like ESs provide a general mechanism to explain the generation of errors and re-writing of information transfer in every step of the central dogma of molecular biology.

8.3. Exchange between alternative secondary structures in RNA

RNA molecules can form ESs that dramatically alter their secondary structure. Fig. 39 shows different types of ESs in RNA that have been characterized to date using off-resonance $R_{1\rho}$ RD methods[16, 164]. Functions are beginning to emerge for many of these ESs in RNA. For example, as mentioned previously in the context of HIV-1 SL1[16], RNA ESs appear to provide means by which to break down large conformational transitions into multiple kinetically labile microscopic steps[290]. A similar mechanism has been proposed for an ES in P5abc, which is proposed to form an intermediate during tertiary folding[164]. RNA ESs characterized by other RD methods have also been shown to play important roles in gene regulation[31] and in ligand binding[32, 78, 79].

As they remodel structure and disrupt biological activity, RNA ESs are proposed as opportune targets for the development of RNA-targeted therapeutics[16]. In addition, there is mounting evidence that the mechanism underlying the disease phenotype of many single nucleotide polymorphisms (SNPs) involves changes in RNA ensembles by stabilizing alternative ES conformations[291 – 293]. Future studies of ESs in RNA will undoubtedly clarify their potential roles in biology and disease.

9. Conclusions

Since the earliest studies of chemical exchange in DNA in the late 1980s, the $R_{1\rho}$ RD methodology has matured significantly during the past four decades to the point that it can now be routinely applied to characterize ESs in DNA and RNA. These advances coupled to development of CEST[28, 31] as well as CPMG[18, 136, 174, 294] methodology have opened the door to a world of previously unknown dynamics in DNA and RNA that play essential roles in gene expression and regulation. Central to these developments are experiments for accurately measuring RD data for a variety of spins in uniformly $^{13}C/^{15}N$ labeled samples over a range of spin-lock amplitudes, using mutations and chemical modifications to stabilize or destabilize ESs relative to the GS, an improved understanding of chemical-shift/structure relationships in nucleic acids, as well as advances in predicting nucleic acid chemical shifts based on 3D structure. Existing methods can immediately be applied to study the dynamics in higher-order DNA structures (e.g. quadruplexes, triplexes etc.)[295] and in RNAs ranging from simple singlestrands[199] to RNAs with complex tertiary folds[31, 164]. We can also anticipate advances that extend the methodology in the future to allow studies of dynamics in larger RNAs and DNAs and their complexes with proteins, and provide additional structural and dynamic information regarding ESs. We hope that this review will provide a useful resource for these future studies.

Supplementary Material

Refer to Web version on PubMed Central for supplementary material.

Acknowledgements

We thank Zachary Stein for fruitful discussions as well as other members of the Al-Hashimi laboratory for critically reading the manuscript. This work was supported by the US National Institutes of Health (R01AI066975,

R01GM089846) and US National Institute for General Medical Sciences (4P50GM103297, P01GM0066275) grants to H. M. A.

Glossary

A	Adenine
AIC	Akaike Information Criterion
AVG	population-weighted average
BIC	Bayesian Information Criterion
B-M	Bloch-McConnell
BMNS	Bloch-McConnell Numerical Simulator
BPs	base pairs
BPTI	Bovine Pancreatic Trypsin Inhibitor
C	Cytosine
CEST	Chemical Exchange Saturation Transfer
cmo^{5}U	Uridine 5-oxyacetic acid
CP	cross polarization
CPMG	Carr-Purcell-Meiboom-Gill
CSA	Chemical Shift Anisotropy
c7A	N7-deaza adenosine
c7G	N7-deaza guanosine
DD/CSA	Dipole-Dipole CSA cross-correlated relaxation
DD/DD	Dipole-dipole cross-correlated relaxation
DNA	Deoxyribonucleic acid
ES	Excited State
ES1/ES2	Excited State 1/Excited State 2
G	Guanine
GS	Ground State
HMQC	Heteronuclear Multiple Quantum Coherence
HSQC	Heteronuclear Single Quantum Coherence
I	Inosine

ms	millisecond
m^{1}A	N^1-methyl adenosine
m^{1}G	N^1-methyl guanosine
m^{6,6}A	N^6,N^6-dimethyl adenine
NMR	Nuclear Magnetic Resonance
NOE	Nuclear Overhauser Effect
ns	nanosecond
NTP	nucleotide tri-phosphate
OBS	observed
ps	picosecond
RCSA	Residual Chemical Shift Anisotropy
RD	Relaxation Dispersion
RDC	Residual Dipolar Coupling
RF	Radio Frequency
RNA	Ribonucleic acid
RSS	residual sum of squares
SH3	SRC Homology Domain 3
SL1	Stem Loop 1
T	Thymine
TROSY	Transverse Relaxation Optimized Spectroscopy
TS	Transition State
U	Uracil
ROESY	Rotating frame Overhauser Spectroscopy

References

[1]. Watson JD, Crick FHC, A Structure for Deoxyribose Nucleic Acid, Nature, 171 (1953) 737–738. [PubMed: 13054692]

[2]. Bardaro MF Jr., Varani G, Examining the relationship between RNA function and motion using nuclear magnetic resonance, Wiley interdisciplinary reviews. RNA, 3 (2012) 122–132. [PubMed: 22180312]

[3]. Rinnenthal J, Buck J, Ferner J, Wacker A, Furtig B, Schwalbe H, Mapping the landscape of RNA dynamics with NMR spectroscopy, Accounts of chemical research, 44 (2011) 1292–1301. [PubMed: 21894962]

[4]. Bothe JR, Nikolova EN, Eichhorn CD, Chugh J, Hansen AL, Al-Hashimi HM, Characterizing RNA dynamics at atomic resolution using solution-state NMR spectroscopy, Nature methods, 8 (2011) 919–931. [PubMed: 22036746]

[5]. Palmer AG 3rd, Chemical exchange in biomacromolecules: Past, present, and future, Journal of magnetic resonance (San Diego, Calif. : 1997), 241 (2014) 3–17.

[6]. Mittermaier A, Kay LE, New tools provide new insights in NMR studies of protein dynamics, Science (New York, N.Y.), 312 (2006) 224–228.

[7]. Getz MM, Andrews AJ, Fierke CA, Al-Hashimi HM, Structural plasticity and Mg2+ binding properties of RNase P P4 from combined analysis of NMR residual dipolar couplings and motionally decoupled spin relaxation, RNA (New York, N.Y.), (2006).

[8]. Shajani Z, Varani G, NMR studies of dynamics in RNA and DNA by (13)C relaxation, Biopolymers, 86 (2007) 348–359. [PubMed: 17154290]

[9]. Xue Y, Kellogg D, Kimsey IJ, Sathyamoorthy B, Stein ZW, McBrairty M, Al-Hashimi HM, Characterizing RNA Excited States Using NMR Relaxation Dispersion, Methods in enzymology, 558 (2015) 39–73. [PubMed: 26068737]

[10]. Salmon L, Yang S, Al-Hashimi HM, Advances in the Determination of Nucleic Acid Conformational Ensembles, Annual review of physical chemistry, 65(1) (2013) 293–316.

[11]. Dethoff EA, Chugh J, Mustoe AM, Al-Hashimi HM, Functional complexity and regulation through RNA dynamics, Nature, 482 (2012) 322–330. [PubMed: 22337051]

[12]. Mustoe AM, Brooks CL, Al-Hashimi HM, Hierarchy of RNA functional dynamics, Annual review of biochemistry, 83 (2014) 441–466.

[13]. Palmer AG 3rd, Massi F, Characterization of the dynamics of biomacromolecules using rotating-frame spin relaxation NMR spectroscopy, Chemical reviews, 106 (2006) 1700–1719. [PubMed: 16683750]

[14]. Palmer AG, Chemical Exchange Effects in Biological Macromolecules, eMagRes, (2007).

[15]. Mulder FA, Mittermaier A, Hon B, Dahlquist FW, Kay LE, Studying excited states of proteins by NMR spectroscopy, Nature structural biology, 8 (2001) 932–935. [PubMed: 11685237]

[16]. Dethoff EA, Petzold K, Chugh J, Casiano-Negroni A, Al-Hashimi HM, Visualizing transient low-populated structures of RNA, Nature, 491 (2012) 724–728. [PubMed: 23041928]

[17]. Nikolova EN, Kim E, Wise AA, O'Brien PJ, Andricioaei I, Al-Hashimi HM, Transient Hoogsteen base pairs in canonical duplex DNA, Nature, 470 (2011) 498–502. [PubMed: 21270796]

[18]. Strebitzer E, Nussbaumer F, Kremser J, Tollinger M, Kreutz C, Studying sparsely populated conformational states in RNA combining chemical synthesis and solution NMR spectroscopy, Methods (San Diego, Calif.), 148 (2018) 39–47.

[19]. Carr HY, Purcell EM, Effects of Diffusion on Free Precession in Nuclear Magnetic Resonance Experiments, Phys. Rev, 94 (1954) 630–638.

[20]. Meiboom S, Gill D, Modified Spin-Echo Method for Measuring Nuclear Relaxation Times, Rev. Sci. Instrum, 29 (1958) 688–691.

[21]. Hansen AL, Nikolova EN, Casiano-Negroni A, Al-Hashimi HM, Extending the range of microsecond-to-millisecond chemical exchange detected in labeled and unlabeled nucleic acids by selective carbon R(1rho) NMR spectroscopy, Journal of the American Chemical Society, 131 (2009) 3818–3819. [PubMed: 19243182]

[22]. Palmer AG 3rd, Kroenke CD, Loria JP, Nuclear magnetic resonance methods for quantifying microsecond-to-millisecond motions in biological macromolecules, Methods in enzymology, 339 (2001) 204–238. [PubMed: 11462813]

[23]. Trott O, Palmer AG 3rd, R1rho relaxation outside of the fast-exchange limit, Journal of magnetic resonance (San Diego, Calif. : 1997), 154 (2002) 157–160.

[24]. Forsen S, Hoffman R, Study of Moderately Rapid Chemical Exchange Reactions by Means of Nuclear Magnetic Double Resonance, J. Chem. Phys, 39 (1963) 2892–2901.

[25]. Fawzi NL, Ying J, Ghirlando R, Torchia DA, Clore GM, Atomic-resolution dynamics on the surface of amyloid-beta protofibrils probed by solution NMR, Nature, 480 (2011) 268–272. [PubMed: 22037310]

[26]. Vallurupalli P, Bouvignies G, Kay LE, Studying “invisible” excited protein states in slow exchange with a major state conformation, Journal of the American Chemical Society, 134 (2012) 8148–8161. [PubMed: 22554188]

[27]. Long D, Bouvignies G, Kay LE, Measuring hydrogen exchange rates in invisible protein excited states, Proceedings of the National Academy of Sciences of the United States of America, 111 (2014) 8820–8825. [PubMed: 24889628]

[28]. Zhao B, Hansen AL, Zhang Q, Characterizing slow chemical exchange in nucleic acids by carbon CEST and low spin-lock field R(1rho) NMR spectroscopy, Journal of the American Chemical Society, 136 (2014) 20–23. [PubMed: 24299272]

[29]. Longhini AP, LeBlanc RM, Becette O, Salguero C, Wunderlich CH, Johnson BA, D’Souza VM, Kreutz C, Dayie TK, Chemo-enzymatic synthesis of site-specific isotopically labeled nucleotides for use in NMR resonance assignment, dynamics and structural characterizations, Nucleic acids research, 44 (2016) e52. [PubMed: 26657632]

[30]. Roy S, Lammert H, Hayes RL, Chen B, LeBlanc R, Dayie TK, Onuchic JN, Sanbonmatsu KY, A magnesium-induced triplex pre-organizes the SAM-II riboswitch, PLoS computational biology, 13 (2017) e1005406. [PubMed: 28248966]

[31]. Zhao B, Guffy SL, Williams B, Zhang Q, An excited state underlies gene regulation of a transcriptional riboswitch, Nature chemical biology, 13 (2017) 968–974. [PubMed: 28719589]

[32]. Chen B, LeBlanc R, Dayie TK, SAM-II Riboswitch Samples at least Two Conformations in Solution in the Absence of Ligand: Implications for Recognition, Angewandte Chemie (International ed. in English), 55 (2016) 2724–2727. [PubMed: 26800479]

[33]. Bloch F, Hansen WW, Packard M, Nuclear Induction, Phys. Rev, 69 (1946) 127.

[34]. Purcell EM, Torrey HC, Pound RV, Resonance Absorption by Nuclear Magnetic Resonance in a Solid, Phys. Rev, 69 (1945) 37–38.

[35]. Gorter CJ, Brons F, Magnetic Inhibition of Susceptibilities at Radio Frequencies, Physica, 7 (1937) 579–584.

[36]. Gorter CJ, Paramagnetic Relaxation, Physica, 3 (1936) 503–514.

[37]. Gorter CJ, Broer LJF, Negative Result of an Attempt to Observe Nuclear Magnetic Resonance in Solids, Physica, 6 (1942) 591–596.

[38]. Gorter CJ, Negative Result of an Attempt to Detect Nuclear Magnetic Spins, Physica, 9 (1936) 995–998.

[39]. Heitler W, Wills HH, Teller E, Time Effects in the Magnetic Cooling Method-I, Proc. Roy. Soc. A, 155 (1936) 629–639.

[40]. Bloembergen N, Purcell EM, Pound RV, Relaxation Effects in Nuclear Magnetic Resonance Absorption, Phys. Rev, 73 (1948) 679–712.

[41]. Torrey HC, Transient Nutations in Nuclear Magnetic Resonance, Phys. Rev, 76 (1949) 1059–1068.

[42]. Hahn EN, An Accurate Nuclear Magnetic Resonance Method for Measuring Spin-Lattice Relaxation Times, Phys. Rev, 76 (1949) 145–146.

[43]. Drain LE, A Direct Method of Measuring Nuclear Spin-Lattice Relaxation Times, Proc Phys Soc A, 62 (1949) 301–306.

[44]. Hahn EN, Spin Echoes, Phys. Rev, 80 (1950) 580–594.

[45]. McConnell HM, REACTION RATES BY NUCLEAR MAGNETIC RESONANCE, J. Chem. Phys, 28 (1958) 430–431.

[46]. Bloch F, Phys. Rev, 70 (1946) 460–474.

[47]. Meiboom S, Luz Z, Gill D, Proton Relaxation in Water, J. Chem. Phys, 27 (1957) 1411–1412.

[48]. Grunwald E, Lowenstein A, Meiboom S, Rates and Mechanisms of Protolysis of Methylammonium Ion in Aqueous Solution Studied by Proton Magnetic Resonance, J. Chem. Phys, 27 (1957) 630–640.

[49]. Gutowsky HS, McCall DW, Slichter CP, Nuclear Magnetic Resonance Multiplets in Liquids, J. Chem. Phys, 21 (1953) 279–292.

[50]. Gutowsky HS, Saika A, Dissociation, Chemical Exchange, and the Proton Magnetic Resonance in Some Aqueous Electrolytes, J. Chem. Phys, 21 (1953) 1688–1694.

[51]. Gutowsky HS, Holm CH, Rate Processes and Nuclear Magnetic Resonance Spectra. II. Hindered Internal Rotation of Amides, J. Chem. Phys, 25 (1956) 1228–1234.

[52]. Hahn EL, Maxwell DE, Spin Echo Measurements of Nuclear Spin Coupling in Molecules, Phys. Rev, 88 (1952) 1070–1083.

[53]. Redfield AG, Nuclear Magnetic Resonance Saturation and Rotary Saturation in Solids, Phys. Rev, 98 (1955) 1787–1809.

[54]. Rabi II, Ramsey NF, Schwinger J, Use of Rotating Coordinates in Magnetic Resonance Problems, Rev. Mod. Phys, 26 (1954) 167–171.

[55]. Solomon I, Relaxation magnetique dans les liquides en Presence d'un champ de haute frequence, Compt. Rend, 249 (1959) 1631–1632.

[56]. Winter JM, Resonance Magnetique, Compt. Rend, 249 (1959) 1346–1347.

[57]. Meiboom S, Nuclear Magnetic Resonance Study of the Proton Transfer in Water, J. Chem. Phys, 34 (1961) 375–388.

[58]. Luz Z, Meiboom S, Nuclear Magnetic Resonance Study of the Protolysis of Trimethylammonium Ion in Aqueous Solution—Order of the Reaction with Respect to Solvent, J. Chem. Phys, 39 (1963) 366–370.

[59]. Luz Z, Meiboom S, The Activation Energies of Proton Transfer Reactions in Water, J. Am. Chem. Soc, 86 (1964) 4768–4769.

[60]. Forsen S, Hoffman RA, Exchange Rates by Nuclear Magnetic Multiple Resonance. III. Exchange Reactions in Systems with Several Nonequivalent Sites, J. Chem. Phys, 40 (1964) 1189–1196.

[61]. Allerhand A, Gutowsky HS, Spin—Echo NMR Studies of Chemical Exchange. I. Some General Aspects, J. Chem. Phys, 41 (1964) 2115–2126.

[62]. Allerhand A, Chen F, Gutowsky HS, Spin-Echo NMR Studies of Chemical Exchange. III. Conformational Isomerization of Cyclohexane and d11-Cyclohexane, J. Chem. Phys, 3040 (1965) 3040–3047.

[63]. Deverell C, Morgan RE, Strange JH, Studies of chemical exchange by nuclear magnetic relaxation in the rotating frame, Mol. Phys, 18 (1970) 553–559.

[64]. Rhodes M, Aksness DW, Strange JH, Spin-lattice relaxation in liquid phosphorus tribromide, Mol. Phys, 15 (1968) 541–547.

[65]. Norris MO, Strange JH, Powles JG, Rhodes M, Marsden K, Krynicki K, Nuclear magnetic spin relaxation in solid solutions of hydrogen bromide in deuterium bromide, J. Phys. C: Solid State Phys, 1 (1968) 422–444.

[66]. Morgan RE, Strange JH, Measurements of scalar spin-spin coupling in liquid HCl and HBr by N.M.R. relaxation in the rotating frame, Mol. Phys, 17 (1969) 397–400.

[67]. Strange JH, Morgan RE, Nuclear magnetic interactions and molecular motion in liquids by n.m.r. relaxation in the rotating frame, J. Phys. C: Solid State Phys, 3 (1970) 1999–2011.

[68]. Stilbs P, Moseley ME, Chemical Exchange Rates from Fourier Transform Measurements of Nuclear Spin-Lattice Relaxation in the Rotating Frame. Application to Hindered Internal Rotation in Ureas, J. Magn. Reson, 31 (1978) 55–61.

[69]. Campbell ID, Dobson CM, Ratcliffe RG, Williams RJP, Fourier Transform NMR Pulse Methods for the Measurement Slow-Exchange Rates J. Magn. Reson, 29 (1978) 397–417.

[70]. Dahlquist FW, Longmuir KJ, DuVernet RB, Direct Observation of Chemical Exchange by a Selective Pulse NMR Technique, J. Magn. Reson, 17 (1975) 406–410.

[71]. Campbell ID, Dobson CM, Ratcliffe RG, Fourier Transform Proton NMR in H2O. A Method for Measuring Exchange and Relaxation Rates J. Magn. Reson, 27 (1977) 455–463.

[72]. Brown TA, Saturation transfer in living systems, Phil. Trans. R. Soc. Lond. B, 289 (1980) 441–444. [PubMed: 6106218]

[73]. Sykes BD, An Application of Transient Nuclear Magnetic Resonance Methods to the Measurement of Biological Exchange Rates. The Interaction of Trifluoroacetyl-D-phenylalanine with the Chymotrypsins, J. Am. Chem. Soc, 91 (1969) 949–955. [PubMed: 5778277]

[74]. Gerig JT, Stock AD, Studies of the Kinetics of the Interaction between N-Trifluoroacetyl-D-tryptophan and a-Chymotrypsin by Pulsed Nuclear Magnetic Resonance, Org. Magn. Reson, 7 (1975) 249–255.

[75]. Cayley PJ, Albrand JP, Feeney J, Roberts GCK, Piper EA, Burgen ASV, Nuclear Magnetic Resonance Studies of the Binding of Trimethoprim to Dihydrofolate Reductase, J. Am. Chem. Soc, 18 (1979) 3886–3895.

[76]. Lee AR, Hwang J, Hur JH, Ryu KS, Kim KK, Choi BS, Kim NK, Lee JH, NMR Dynamics Study Reveals the Zalpha Domain of Human ADAR1 Associates with and Dissociates from Z-RNA more slowly than Z-DNA, ACS chemical biology, (2018).

[77]. Moschen T, Grutsch S, Juen MA, Wunderlich CH, Kreutz C, Tollinger M, Measurement of Ligand-Target Residence Times by (1)H Relaxation Dispersion NMR Spectroscopy, J Med Chem, 59 (2016) 10788–10793. [PubMed: 27933946]

[78]. Wunderlich CH, Spitzer R, Santner T, Fauster K, Tollinger M, Kreutz C, Synthesis of (6-(13)C)pyrimidine nucleotides as spin-labels for RNA dynamics, Journal of the American Chemical Society, 134 (2012) 7558–7569. [PubMed: 22489874]

[79]. Moschen T, Wunderlich CH, Spitzer R, Levic J, Micura R, Tollinger M, Kreutz C, Ligand-detected relaxation dispersion NMR spectroscopy: dynamics of preQ1-RNA binding, Angewandte Chemie (International ed. in English), 54 (2015) 560–563. [PubMed: 25403518]

[80]. James TL, Matson GB, Kuntz ID, Protein Rotational Correlation Times Determined in Aqueous Solution by Carbon-13 Rotating Frame Spin-Lattice Relaxation in the Presence of an Off-Resonance Radiofrequency Field, J. Am. Chem. Soc, 100 (1978) 3590–3594.

[81]. James TL, Sawan SP, Unfolding of Ribonuclease A by Guanidinium Chloride. Protein Internal Motions Studied by Nuclear Magnetic Resonance Spin-Lattice Relaxation in an Off-Resonance Rotating Frame, J. Am. Chem. Soc, 101 (1979) 7050–7055.

[82]. Bolton PH, James TL, Molecular Motions in RNA and DNA Investigated by Phosphorus-31 and Carbon-13 NMR Relaxation, J. Phys. Chem, 83 (1979) 3359–3366.

[83]. Smith GM, Yu LP, Domingues DJ, Directly Observed 15N NMR Spectra of Uniformly Enriched Proteins, Biochemistry, 26 (1987) 2202–2207. [PubMed: 3040083]

[84]. McCain DC, Ulrich EL, Markley JL, NMR Relaxation Study of Internal Motions in Staphylococcal Nuclease, J. Magn. Resonan, 80 (1988) 296–305.

[85]. Schmidt PG, Playl T, Agris PF, Internal Dynamics of Transfer Ribonucleic Acid Determined by Nuclear Magnetic Resonance of Carbon-13-Enriched Ribose Carbon V, Biochemistry, 22 (1983) 1408–1415. [PubMed: 6188489]

[86]. Campbell ID, Dobson CM, Moore GR, Perkins SJ, Williams RJP, Temperature Dependent Molecular Motion of a Tyrosine Residue of Ferrocytochrome C, Febs Lett, 70 (1976) 96–100. [PubMed: 186328]

[87]. Bleich HE, Glasel JA, Rotating Frame Spin-Lattice Relaxation Experiments and the Problem of Intramolecular Motions of Peptides in Solution, Biopolymers, 17 (1978) 2445–2457.

[88]. Kopple KD, Wang Y, N.m.r. studies of internal mobility in a cyclic tetrapeptide, Int. J. Peptide Protein Res, 33 (1989) 82–85. [PubMed: 2707972]

[89]. Kopple KD, Wang Y, Cheng AG, Bhandary KK, Conformations of Cyclic Octapeptides. 5. Crystal Structure of Cyclo(Cys-Gly-Pro-Phe)2 and Rotating Frame Relaxation (T1p) NMR Studies of Internal Mobility in Cyclic Octapeptides, J. Am. Chem. Soc, 110 (1988) 4168–4176.

[90]. Blackledge MJ, Bruschweiler R, Griesinger C, Schmidt JM, Xu P, Ernst RR, Conformational Backbone Dynamics of the Cyclic Decapeptide Antamanide. Application of a New Multiconformational Search Algorithm Based on NMR data, Biochemistry, 32 (1993) 10960–10974. [PubMed: 8218162]

[91]. Bothner-By AA, Stephens RL, Lee J, Warren CD, Jeanloz RW, Structure determination of a tetrasaccharide: transient nuclear Overhauser effects in the rotating frame, Journal of the American Chemical Society, 106 (1984) 811–813.

[92]. Bax A, Davis DG, Practical Aspects of Two-Dimensional Transverse NOE Spectroscopy, J. Magn. Reson, 63 (1985) 207–213.

[93]. Cavanagh J, Keeler J, Suppression of HOHAHA and “False” NOE Cross Peaks in CAMELSPIN Spectra, Journal of magnetic resonance (San Diego, Calif. : 1997), 80 (1988) 186–194.

[94]. Desvaux H, Berthault P, Birlirakis N, Goldman M, Piotto M, Improved Versions of Off-Resonance ROESY, Journal of Magnetic Resonance, Series A, 113 (1995) 47–52.

[95]. Desvaux H, Berthault P, Birlirakis N, Goldman M, Off-Resonance ROESY for the Study of Dynamic Processes, Journal of magnetic resonance (San Diego, Calif. : 1997), 108 (1994) 219–229.

[96]. Isaksson J, Zamaratski E, Maltseva TV, Agback P, Kumar A, Chattopadhyaya J, The first example of a Hoogsteen base-paired DNA duplex in dynamic equilibrium with a Watson-Crick base-paired duplex--a structural (NMR), kinetic and thermodynamic study, Journal of Biomolecular Structure & Dynamics, 18 (2001) 783–806. [PubMed: 11444368]

[97]. Boulton S, Akimoto M, Akbarizadeh S, Melacini G, Free energy landscape remodeling of the cardiac pacemaker channel explains the molecular basis of familial sinus bradycardia, J Biol Chem, 292 (2017) 6414–6428. [PubMed: 28174302]

[98]. Maltseva TV, Yamakage SI, Agback P, Chattopadhyaya J, Direct estimation of basepair exchange kinetics in oligo-DNA by a combination of NOESY and ROESY experiments, Nucleic acids research, 21 (1993) 4288–4295. [PubMed: 8414984]

[99]. Halle B, Denisov VP, Water and Monovalent Ions in the Minor Groove of B-DNA Oligonucleotides as Seen by NMR, Biopolymers, 48 (2000) 210–233.

[100]. Conte MR, Conn GL, Brown T, Lane AN, Hydration of the RNA duplex r(CGCAAAUUUGCG)2 determined by NMR, Nucleic acids research, 24 (1996) 3693–3699. [PubMed: 8871546]

[101]. Leroy JL, Broseta D, Gueron M, Proton exchange and base-pair kinetics of poly(rA).poly(rU) and poly(rI).poly(rC), Journal of molecular biology, 184 (1985) 165–178. [PubMed: 2993629]

[102]. Gueron M, Kochoyan M, Leroy JL, A single mode of DNA base-pair opening drives imino proton exchange, Nature, 328 (1987) 89–92. [PubMed: 3037381]

[103]. Leroy JL, Gehring K, Kettani A, Gueron M, Acid multimers of oligodeoxycytidine strands: stoichiometry, base-pair characterization, and proton exchange properties, Biochemistry, 32 (1993) 6019–6031. [PubMed: 8389586]

[104]. Kay LE, Torchia DA, Bax A, Backbone Dynamics of Proteins As Studied by ^{15}N Inverse Detected Heteronuclear NMR Spectroscopy: Application to Staphlococcal Nuclease, Biochemistry, 28 (1989) 8972–8979. [PubMed: 2690953]

[105]. Lipari G, Szabo A, Model-Free Approach to the Interpretation of Nuclear Magnetic Resonance Relaxation in Macromolecules. 1. Theory and Range of Validity, Journal of the American Chemical Society, 104 (1982) 4546–4559.

[106]. Lipari G, Szabo A, Nuclear magnetic resonance relaxation in nucleic acid fragments: models for internal motion, Biochemistry, 20 (1981) 6250–6256. [PubMed: 7306511]

[107]. Liepert TK, Noggle JH, Freeman WJ, Dalrymple DL, Rotating Frame Nuclear Relaxation of PBr, : Off-ResonanceStudiesby Fourier Transform NMR, Journal of magnetic resonance (San Diego, Calif. : 1997), 19 (1975) 208–221.

[108]. Freeman R, Hill HDW, Fourier Transform Study of NMR Spin–Spin Relaxation, The Journal of chemical physics, 55 (1971) 1985–1986.

[109]. Wang Y, Ikuta S, Proton On-Resonance Rotating Frame Spin-Lattice Relaxation Measurements of B and Z Double-Helical Oligodeoxyribonucleotides in Solution, J. Am. Chem. Soc, 111 (1989) 1243–1248.

[110]. Schmitz U, Sethson I, Egan WM, James TL, Solution Structure of a DNA Octamer Containing the Pribnow Box via Restrained Molecular Dynamics Simulation with Distance and Torsion Angle Constraints Derived from Nuclear Magnetic Resonance Spectral Fitting, J. Mol. Biol, 227 (1992) 510–531. [PubMed: 1404366]

[111]. Lane AN, Bauer CJ, Frenkiel TA, Determination of conformational transition rates in the trp promoter by NMR rotating-frame and cross-relaxation rate measurements, Eur. J. Biochem, 21 (1993) 425–431.

[112]. Nikolova EN, Gottardo FL, Al-Hashimi HM, Probing transient Hoogsteen hydrogen bonds in canonical duplex DNA using NMR relaxation dispersion and single-atom substitution, Journal of the American Chemical Society, 134 (2012) 3667–3670. [PubMed: 22309937]

[113]. Nikolova EN, Goh GB, Brooks CL 3rd, Al-Hashimi HM, Characterizing the Protonation State of Cytosine in Transient G.C Hoogsteen Base Pairs in Duplex DNA, Journal of the American Chemical Society, (2013).

[114]. Nikolova EN, Zhou H, Gottardo FL, Alvey HS, Kimsey IJ, Al-Hashimi HM, A historical account of hoogsteen base-pairs in duplex DNA, Biopolymers, (2013).

[115]. Alvey HS, Gottardo FL, Nikolova EN, Al-Hashimi HM, Widespread transient Hoogsteen base pairs in canonical duplex DNA with variable energetics, Nature communications, 5 (2014) 4786.

[116]. Sathyamoorthy B, Shi H, Zhou H, Xue Y, Rangadurai A, Merriman DK, Al-Hashimi HM, Insights into Watson-Crick/Hoogsteen breathing dynamics and damage repair from the solution structure and dynamic ensemble of DNA duplexes containing m1A, Nucleic acids research, 45 (2017) 5586–5601. [PubMed: 28369571]

[117]. Shi H, Clay MC, Rangadurai A, Sathyamoorthy B, Case DA, Al-Hashimi HM, Atomic structures of excited state A-T Hoogsteen base pairs in duplex DNA by combining NMR relaxation dispersion, mutagenesis, and chemical shift calculations, Journal of biomolecular NMR, 70 (2018) 229–244. [PubMed: 29675775]

[118]. Lane AN, Peck B, Conformational flexibility in DNA duplexes containing single G G mismatches, Eur. J. Biochem, 230 (1995) 1073–1087. [PubMed: 7601138]

[119]. Bolton PH, A Primer on Isotopic Labeling in NMR Investigations of Biopolymers, Prog. Nucl. Magn. Resonan. Spectrosc, 22 (1991) 423–452.

[120]. Nirmala NR, Wagner G, Measurement of 13C Relaxation Times in Proteins by Two-Dimensional Heteronuclear 1H-13C Correlation Spectroscopy, Journal of the American Chemical Society, 110 (1988) 7557–7558.

[121]. Nirmala NR, Wagner G, Measurement of 13C Spin-Spin Relaxation Times by Two-Dimensional Heteronuclear'H- "C Correlation Spectroscopy, J. Magn. Reson, 82 (1989) 659–661.

[122]. Szyperski T, Luginbuhl P, Otting G, Guntert P, Wuthrich K, Protein dynamics studied by rotating frame 15Nspin relaxation times, J. Biomol. NMR, 3 (1993) 151–164. [PubMed: 7682879]

[123]. Peng JW, Thanabal V, Wagner G, 2D Heteronuclear NMR Measurements of Spin-Lattice Relaxation Times in the Rotating Frame of X Nuclei in Heteronuclear HX Spin Systems, J. Magn. Reson, 94 (1991) 82–100.

[124]. Stone MJ, Fairbrother WJ, Palmer AG, Reizer J, Saier MH, Wright PE, Backbone Dynamics of the Bacillus subtilis Glucose Permease IIA Domain Determined from 15N NMR Relaxation Measurements, Biochemistry, 31 (1992) 4394–4406. [PubMed: 1316146]

[125]. Stone MJ, Chandrasekhar K, Holmgren A, Wright PE, Dyson HJ, Comparison of Backbone and Tryptophan Side-Chain Dynamics of Reduced and Oxidized Escherichia coli Thioredoxin Using 15N NMR Relaxation Measurements, Biochemistry, 32 (1993) 426–435. [PubMed: 8422352]

[126]. Orekhov VY, Pervushin KV, Arseniev AS, Backbone dynamics of (1–7l)bacterioopsin studied by two-dimensional 'H-l5N NMR spectroscopy, Eur. J. Biochem, 219 (1994) 887–896. [PubMed: 8112340]

[127]. Zhong J, Gore JC, Armitage IM, Relative Contributions of Chemical Exchange and Other Relaxation Mechanisms in Protein Solutions and Tissues, Magn Reson Med, 11 (1989) 295–308. [PubMed: 2550719]

[128]. Milligan JF, Groebe DR, Witherell GW, Uhlenbeck OC, Oligoribonucleotide synthesis using T7RNA polymerase and synthetic DNA templates, Nucleic acids research, 15 (1987) 8783–8798. [PubMed: 3684574]

[129]. Zimmer DP, Crothers DM, NMR of enzymatically synthesized uniformly 13C15N-labeled DNA oligonucleotides, Proc. Natl. Acad. Sci. U. S. A, 92 (1995) 3091–3095. [PubMed: 7724521]

[130]. Gaudin F, Chanteloup L, Thuong NT, Lancelot G, Selectively 13C-Enriched DNA: Dynamics of the C1'H1' and C5'H5' or C5'H5" Vectors in d(CGCAAATTTGCG)2, Magn. Reson. Chem, 35 (1997) 561–565.

[131]. Maltseva TV, Foldesi A, Ossipov D, Chattopadhyaya J, Comparative 13C and 2H relaxation study of microsecond dynamics of the AT tract of selectively 13C/2H double-labelled DNA duplexes, Magn. Reson. Chem, 38 (2000) 403–414.

[132]. Hoogstraten CG, Wank JR, Pardi A, Active site dynamics in the lead-dependent ribozyme, Biochemistry, 39 (2000) 9951–9958. [PubMed: 10933815]

[133]. Latham MP, Brown DJ, McCallum SA, Pardi A, NMR methods for studying the structure and dynamics of RNA, Chembiochem : a European journal of chemical biology, 6 (2005) 1492–1505. [PubMed: 16138301]

[134]. Boisbouvier J, Brutscher B, Simorre J, Marion D, 13C spin relaxation measurements in RNA: Sensitivity and resolution improvement using spin-state selective correlation experiments, J. Biomol. NMR, 14 (1999) 241–252.

[135]. Blad H, Reiter NJ, Abildgaard F, Markley JL, Butcher SE, Dynamics and metal ion binding in the U6 RNA intramolecular stem-loop as analyzed by NMR, Journal of molecular biology, 353 (2005) 540–555. [PubMed: 16181635]

[136]. Johnson JE Jr., Hoogstraten CG, Extensive backbone dynamics in the GCAA RNA tetraloop analyzed using 13C NMR spin relaxation and specific isotope labeling, Journal of the American Chemical Society, 130 (2008) 16757–16769. [PubMed: 19049467]

[137]. Oberstrass FC, Allain FHT, Ravindranathan S, Changes in Dynamics of SRE-RNA on Binding to the VTS1p-SAM Domain Studied by 13C NMR Relaxation, Journal of the American Chemical Society, 130 (2008) 12007–12020. [PubMed: 18698768]

[138]. Shajani Z, Varani G, 13C NMR relaxation studies of RNA base and ribose nuclei reveal a complex pattern of motions in the RNA binding site for human U1A protein, Journal of molecular biology, 349 (2005) 699–715. [PubMed: 15890361]

[139]. Shajani Z, Drobny G, Varani G, Binding of U1A Protein Changes RNA Dynamics As Observed by (13)C NMR Relaxation Studies(,), Biochemistry, 46 (2007) 5875–5883. [PubMed: 17469848]

[140]. Shajani Z, Varani G, 13C relaxation studies of the DNA target sequence for hhai methyltransferase reveal unique motional properties, Biochemistry, 47 (2008) 7617–7625. [PubMed: 18578505]

[141]. Cavanagh J, Venters RA, Protein dynamic studies move to a new time slot, Nature Struct Biol, 8 (2001) 912–914. [PubMed: 11685230]

[142]. Loria JP, Rance M, Palmer AG, A relaxation-compensated Carr-Purcell-Meiboom-Gill sequence for characterizing chemical exchange by NMR spectroscopy, Journal of the American Chemical Society, 121 (1999) 2331–2332.

[143]. Skrynnikov NR, Dahlquist FW, Kay LE, Reconstructing NMR Spectra of “Invisible” Excited Protein States Using HSQC and HMQC Experiments, J. Am. Chem. Soc, 124 (2002) 12352–12360. [PubMed: 12371879]

[144]. Mulder FA, Skrynnikov NR, Hon B, Dahlquist FW, Kay LE, Measurement of slow (micros-ms) time scale dynamics in protein side chains by (15)N relaxation dispersion NMR spectroscopy: application to Asn and Gln residues in a cavity mutant of T4 lysozyme, Journal of the American Chemical Society, 123 (2001) 967–975. [PubMed: 11456632]

[145]. Skrynnikov NR, Mulder FAA, Hon B, Dahlquist FW, Kay LE, Probing Slow Time Scale Dynamics at Methyl-Containing Side Chains in Proteins by Relaxation Dispersion NMR Measurements: Application to Methionine Residues in a Cavity Mutant of T4 Lysozyme, Journal of the American Chemical Society, 123 (2001) 4556–4566. [PubMed: 11457242]

[146]. Orekhov VY, Korzhnev DM, Kay LE, Double- and zero-quantum NMR relaxation dispersion experiments sampling millisecond time scale dynamics in proteins, Journal of the American Chemical Society, 126 (2004) 1886–1891. [PubMed: 14871121]

[147]. Korzhnev DM, Kloiber K, Kay LE, Multiple-quantum relaxation dispersion NMR spectroscopy probing millisecond time-scale dynamics in proteins: theory and application, Journal of the American Chemical Society, 126 (2004) 7320–7329. [PubMed: 15186169]

[148]. Dittmer J, Bodenhausen G, Evidence for Slow Motion in Proteins by Multiple Refocusing of Heteronuclear Nitrogen/Proton Multiple Quantum Coherences in NMR, Journal of the American Chemical Society, 126 (2003) 1314–1315.

[149]. Lundstrom P, Hansen DF, Vallurupalli P, Kay LE, Accurate measurement of alpha proton chemical shifts of excited protein states by relaxation dispersion NMR spectroscopy, Journal of the American Chemical Society, 131 (2009) 1915–1926. [PubMed: 19152327]

[150]. Ishima R, Baber J, Louis JM, Torchia DA, Carbonyl carbon transverse relaxation dispersion measurements and ms-micros timescale motion in a protein hydrogen bond network, Journal of biomolecular NMR, 29 (2004) 187–198. [PubMed: 15014232]

[151]. Pervushin K, Riek R, Wider G, Wuthrich K, Transverse relaxation-optimized spectroscopy (TROSY) for NMR studies of aromatic spin systems in C-13-labeled proteins, Journal of the American Chemical Society, 120 (1998) 6394–6400.

[152]. Korzhnev DM, Kloiber K, Kanelis V, Tugarinov V, Kay LE, Probing Slow Dynamics in High Molecular Weight Proteins by Methyl-TROSY NMR Spectroscopy: Application to a 723-Residue Enzyme, J. Am. Chem. Soc, 126 (2004) 3964–3973. [PubMed: 15038751]

[153]. Korzhnev DM, Salvatella X, Vendruscolo M, Di Nardo AA, Davidson AR, Dobson CM, Kay LE, Low-populated folding intermediates of Fyn SH3 characterized by relaxation dispersion NMR, Nature, 430 (2004) 586–590. [PubMed: 15282609]

[154]. Akke M, Palmer AG, Monitoring macromolecular motions on microsecond to millisecond time scales by R(1)rho-R(1) constant relaxation time NMR spectroscopy, Journal of the American Chemical Society, 118 (1996) 911–912.

[155]. Yamazaki T, Muhandiram R, Kay LE, NMR Experiments for the Measurement of Carbon Relaxation Properties in Highly Enriched, Uniformly 13C,15N-Labeled Proteins: Application to 13Ca Carbons, J. Am. Chem. Soc, 116 (1994) 8266–8278.

[156]. Wang Y-S, NMR rotating frame relaxation measurement of conformational exchanges on the microsecond time scale (part 1), Conc. Magn. Reson, 4 (1992) 327–337.

[157]. Goldman M, Interference effects in the relaxation of a pair of unlike spin-½ nuclei, Journal of magnetic resonance (San Diego, Calif. : 1997), 60 (1984) 437–452.

[158]. Lee AL, Wand AJ, Assessing potential bias in the determination of rotational correlation times of proteins by NMR relaxation, Journal of biomolecular NMR, 13 (1999) 101–112. [PubMed: 10070752]

[159]. Korzhnev DM, Tischenko EV, Arseniev AS, Off-resonance effects in 15N T2 CPMG measurements, Journal of biomolecular NMR, 17 (2000) 231–237. [PubMed: 10959630]

[160]. Pelupessy P, Chiarparin E, Bodenhausen G, Excitation of selected proton signals in NMR of isotopically labeled macromolecules, Journal of magnetic resonance (San Diego, Calif. : 1997), 138 (1999) 178–181.

[161]. Pelupessy P, Chiarparin E, Hartmann – Hahn Polarization Transfer in Liquids: An Ideal Tool for Selective Experiments, Concepts Magn Reson, 12 (2000) 103–124.

[162]. Ferrage F, Eykyn TR, Bodenhausen G, Frequency-switched single-transition cross-polarization: a tool for selective experiments in biomolecular NMR, Chemphyschem, 5 (2004) 76–84. [PubMed: 14999846]

[163]. Korzhnev DM, Orekhov VY, Kay LE, Off-resonance R1(p) NMR studies of exchange dynamics in proteins with low spin-lock fields: An application to a fyn SH3 domain, Journal of the American Chemical Society, 127 (2005) 713–721. [PubMed: 15643897]

[164]. Xue Y, Gracia B, Herschlag D, Russell R, Al-Hashimi HM, Visualizing the formation of an RNA folding intermediate through a fast highly modular secondary structure switch, Nature communications, 7 (2016) ncomms11768.

[165]. Szymanski ES, Kimsey IJ, Al-Hashimi HM, Direct NMR Evidence that Transient Tautomeric and Anionic States in dG.dT Form Watson-Crick-like Base Pairs, Journal of the American Chemical Society, 139 (2017) 4326–4329. [PubMed: 28290687]

[166]. Clay MC, Ganser LR, Merriman DK, Al-Hashimi HM, Resolving sugar puckers in RNA excited states exposes slow modes of repuckering dynamics, Nucleic acids research, (2017).

[167]. Bouvignies G, Kay LE, Measurement of proton chemical shifts in invisible states of slowly exchanging protein systems by chemical exchange saturation transfer, The journal of physical chemistry. B, 116 (2012) 14311–14317. [PubMed: 23194058]

[168]. Bouvignies G, Kay LE, A 2D (1)(3)C-CEST experiment for studying slowly exchanging protein systems using methyl probes: an application to protein folding, Journal of biomolecular NMR, 53 (2012) 303–310. [PubMed: 22689067]

[169]. Vallurupalli P, Bouvignies G, Kay LE, Studying “invisible” excited protein states in slow exchange with a major state conformation, Journal of the American Chemical Society, 134 (2012) 8148–8161. [PubMed: 22554188]

[170]. Zhao B, Zhang Q, Measuring Residual Dipolar Couplings in Excited Conformational States of Nucleic Acids by CEST NMR Spectroscopy, Journal of the American Chemical Society, 137 (2015) 13480–13483. [PubMed: 26462068]

[171]. Tolman JR, Flanagan JM, Kennedy MA, Prestegard JH, Nuclear Magnetic Dipole Interactions in Field-Oriented Proteins - Information For Structure Determination in Solution, Proceedings of the National Academy of Sciences of the United States of America, 92 (1995) 9279–9283. [PubMed: 7568117]

[172]. Tjandra N, Bax A, Direct measurement of distances and angles in biomolecules by NMR in a dilute liquid crystalline medium, Science (New York, N.Y.), 278 (1997) 1111–1114.

[173]. Nussbaumer F, Juen MA, Gasser C, Kremser J, Muller T, Tollinger M, Kreutz C, Synthesis and incorporation of 13C-labeled DNA building blocks to probe structural dynamics of DNA by NMR, Nucleic acids research, 45 (2017) 9178–9192. [PubMed: 28911104]

[174]. LeBlanc RM, Longhini AP, Tugarinov V, Dayie TK, NMR probing of invisible excited states using selectively labeled RNAs, Journal of biomolecular NMR, 71 (2018) 165–172. [PubMed: 29858959]

[175]. Neuner S, Santner T, Kreutz C, Micura R, The “Speedy” Synthesis of Atom-Specific 15N Imino/Amido labeled RNA, Chem. Eur. J, 21 (2015) 11634–11643. [PubMed: 26237536]

[176]. Kloiber K, Spitzer R, Tollinger M, Konrat R, Kreutz C, Probing RNA dynamics via longitudinal exchange and CPMG relaxation dispersion NMR spectroscopy using a sensitive 13C-methyl label, Nucleic acids research, 39 (2011) 4340–4351. [PubMed: 21252295]

[177]. Thakur CS, Luo Y, Chen B, Eldho NV, Dayie TK, Biomass production of site selective 13C/15N nucleotides using wild type and a transketolase E. coli mutant for labeling RNA for high resolution NMR, Journal of biomolecular NMR, 52 (2012) 103–114. [PubMed: 22124680]

[178]. Palmer AG 3rd, Koss H, Chemical Exchange, Methods in enzymology, 615 (2019) 177–236. [PubMed: 30638530]

[179]. Trott O, Abergel D, Palmer AG, An average-magnetization analysis of R 1ρ relaxation outside of the fast exchange limit, Mol. Phys, 101 (2003) 753–763.

[180]. Korzhnev DM, Skrynnikov NR, Millet O, Torchia DA, Kay LE, An NMR experiment for the accurate measurement of heteronuclear spin-lock relaxation rates, Journal of the American Chemical Society, 124 (2002) 10743–10753. [PubMed: 12207529]

[181]. Massi F, Johnson E, Wang C, Rance M, Palmer AG 3rd, NMR R1 rho rotating-frame relaxation with weak radio frequency fields, Journal of the American Chemical Society, 126 (2004) 2247–2256. [PubMed: 14971961]

[182]. Abergel D, Palmer AG, On the use of the Stochastic Liouville Equation in Nuclear Magnetic Resonance: Application to R1p Relaxation in the Presence of Exchange, Concepts Magn. Reson, 19A (2003) 134–148.

[183]. Ishima R, Torchia DA, Estimating the time scale of chemical exchange of proteins from measurements of transverse relaxation rates in solution, J. Biomol. NMR, 14 (1999) 369–372. [PubMed: 10526408]

[184]. Rao BDN, Nuclear Magnetic Resonance Line-Shape Analysis and Determination of Exchange Rates Meth Enzymol, 176 (1989) 279–311. [PubMed: 2811690]

[185]. Peng JW, Thanabal V, Wagner G, 2D Heteronuclear NMR Measurements of Spin-Lattice Relaxation Times in the Rotating Frame of X Nuclei in Heteronuclear HX Spin Systems, Journal of Magnetic Resonance, 94 (1991) 82–100.

[186]. Jones GP, Spin-Lattice Relaxation in the Rotating Frame: Weak-Collision Case, Phys. Rev, 148 (1966) 332–335.

[187]. Yuwen T, Brady JP, Kay LE, Probing Conformational Exchange in Weakly Interacting, Slowly Exchanging Protein Systems via Off-Resonance R1rho Experiments: Application to Studies of Protein Phase Separation, Journal of the American Chemical Society, 140 (2018) 2115–2126. [PubMed: 29303268]

[188]. Cornell BA, Pope JM, A Pulsed NMR Study of Nuclear Spin-Lattice Relaxation in the Off-Resonance Rotating Frame, J. Magn. Reson, 16 (1974) 172–181.

[189]. Davis DG, Perlman ME, London RE, J. Magn. Reson. B, 104 (1994) 266–275. [PubMed: 8069484]

[190]. Ishima R, Torchia DA, Accuracy of optimized chemical-exchange parameters derived by fitting CPMG R2 dispersion profiles when R2(0a) not = R2(0b), Journal of biomolecular NMR, 34 (2006) 209–219. [PubMed: 16645811]

[191]. Kaplan J, Exchange Broadening in Nuclear Magnetic Resonance, J. Chem. Phys, 28 (1958) 278–282.

[192]. Snyder JP, Map projections: A working manual, in: Professional Paper, Washington, D.C., 1987.

[193]. Trott O, Palmer AG 3rd, Theoretical study of R(1rho) rotating-frame and R2 free-precession relaxation in the presence of n-site chemical exchange, Journal of magnetic resonance (San Diego, Calif. : 1997), 170 (2004) 104–112.

[194]. Koss H, Rance M, Palmer AG 3rd, General expressions for R1rho relaxation for N-site chemical exchange and the special case of linear chains, Journal of magnetic resonance (San Diego, Calif. : 1997), 274 (2017) 36–45.

[195]. Kimsey IJ, Szymanski ES, Zahurancik WJ, Shakya A, Xue Y, Chu CC, Sathyamoorthy B, Suo Z, Al-Hashimi HM, Dynamic basis for dG*dT misincorporation via tautomerization and ionization, Nature, 554 (2018) 195–201. [PubMed: 29420478]

[196]. Bothe JR, Stein ZW, Al-Hashimi HM, Evaluating the uncertainty in exchange parameters determined from off-resonance R1rho relaxation dispersion for systems in fast exchange, Journal of magnetic resonance (San Diego, Calif. : 1997), 244 (2014) 18–29.

[197]. Kimsey IJ, Petzold K, Sathyamoorthy B, Stein ZW, Al-Hashimi HM, Visualizing transient Watson-Crick-like mispairs in DNA and RNA duplexes, Nature, 519 (2015) 315–320. [PubMed: 25762137]

[198]. Dethoff EA, Hansen AL, Musselman C, Watt ED, Andricioaei I, Al-Hashimi HM, Characterizing complex dynamics in the transactivation response element apical loop and motional correlations with the bulge by NMR, molecular dynamics, and mutagenesis, Biophysical journal, 95 (2008) 3906–3915. [PubMed: 18621815]

[199]. Eichhorn CD, Feng J, Suddala KC, Walter NG, Brooks CL 3rd, Al-Hashimi HM, Unraveling the structural complexity in a single-stranded RNA tail: implications for efficient ligand binding in the prequeuosine riboswitch, Nucleic acids research, 40 (2012) 1345–1355. [PubMed: 22009676]

[200]. Sun X, Zhang Q, Al-Hashimi HM, Resolving fast and slow motions in the internal loop containing stem-loop 1 of HIV-1 that are modulated by Mg2+ binding: role in the kissing-duplex structural transition, Nucleic acids research, 35 (2007) 1698–1713. [PubMed: 17311812]

[201]. Hansen AL, Al-Hashimi HM, Dynamics of large elongated RNA by NMR carbon relaxation, Journal of the American Chemical Society, 129 (2007) 16072–16082. [PubMed: 18047338]

[202]. Baldwin AJ, Kay LE, An R(1rho) expression for a spin in chemical exchange between two sites with unequal transverse relaxation rates, Journal of biomolecular NMR, 55 (2013) 211–218. [PubMed: 23340732]

[203]. Peng JW, Thanabal V, Wagner G, Improved Accuracy of Heteronuclear Transverse Relaxation Time Measurements in Macromolecules. Elimination of Antiphase Contributions, Journal of Magnetic Resonance, 95 (1991) 421–427.

[204]. Yamazaki T, Muhandiram R, Kay LE, NMR Experiments for the Measurement of Carbon Relaxation Properties in Highly Enriched, Uniformly 13C, 15N-Labeled Proteins: Application to 13Ca Carbons, J . Am. Chem. Soc, 116 (1994) 8266–8278.

[205]. Mulder FAA, de Graaf RA, Kaptein R, Boelens R, An off-resonance rotating frame relaxation experiment for the investigation of macromolecular dynamics using adiabatic rotations, Journal Of Magnetic Resonance, 131 (1998) 351–357. [PubMed: 9571112]

[206]. Mulder FAA, Van Tilborg PJA, Kaptein R, Boelens R, Microsecond time scale dynamics in the RXR DNA-binding domain from a combination of spin-echo and off-resonance rotating frame relaxation measurements, J. Biomol. NMR, 13 (1999) 275–288. [PubMed: 10212986]

[207]. Konrat R, Tollinger M, Heteronuclear relaxation in time-dependent spin systems: (15)NT1 (rho) dispersion during adiabatic fast passage, Journal of biomolecular NMR, 13 (1999) 213–221. [PubMed: 20700818]

[208]. Kim S, Baum J, An on/off resonance rotating frame relaxation experiment to monitor millisecond to microsecond timescale dynamics, Journal of biomolecular NMR, 30 (2004) 195–204. [PubMed: 15702526]

[209]. Zinn-Justin S, Berthault P, Guenneugues M, Desvaux H, Off-resonance rf fields in heteronuclear NMR: Application to the study of slow motions, Journal of biomolecular NMR, 10 (1997) 363–372. [PubMed: 20859782]

[210]. Gueron M, Leroy JL, Griffey RH, Proton Nuclear Magnetic Relaxation of 15N-Labeled Nucleic Acids via Dipolar Coupling and Chemical Shift Anisotropy, Journal of the American Chemical Society, 105 (1983) 7262–7266.

[211]. Boyd J, Hommel U, Campbell ID, Influence of cross - correlation between dipolar and anisotropic chemical shift relaxation mechanisms upon longitudinal relaxation rates of nitrogen-15 in macromolecules, Chem. Phys. Lett, 175 (1990) 477–482.

[212]. Palmer AG III, Skelton NJ, Chazin WJ, Wright PE, Rance M, Suppression of the effects of cross correlation between dipolar and anisotropic chemical-shift relaxation mechanisms in the measurement of spin-spin relaxation rates, Mol. Phys, 75 (1992) 699–711.

[213]. Kay LE, Nicholson LK, Delaglio F, Bax A, Torchia DA, J. Mag. Reson, 97 (1992) 359–375.

[214]. Williamson JR, Boxer SG, Multinuclear NMR studies of DNA hairpins. 1. Structure and dynamics of d(CGCGTTGTTCGCG), Biochemistry, 28 (1989) 2819–2831. [PubMed: 2742814]

[215]. Spitzer R, Kloiber K, Tollinger M, Kreutz C, Kinetics of DNA refolding from longitudinal exchange NMR spectroscopy, Chembiochem : a European journal of chemical biology, 12 (2011) 2007–2010. [PubMed: 21739562]

[216]. Chiarparin E, Pelupessy P, Bodenhausen G, Selective cross-polarization in solution state NMR, Mol Phys, 95 (1998) 759–767.

[217]. Chiarparin E, Pelupessy P, Ghose R, Bodenhausen G, Relative orientation of (CH alpha)-H-alpha-bond vectors of successive residues in proteins through cross-correlated relaxation in NMR, Journal of the American Chemical Society, 122 (2000) 1758–1761.

[218]. Wijmenga SS, van Buuren BNM, The use of NMR methods for conformational studies of nucleic acids, Progress in nuclear magnetic resonance spectroscopy, 32 (1998) 287–387.

[219]. Ban D, Gossert AD, Giller K, Becker S, Griesinger C, Lee D, Exceeding the limit of dynamics studies on biomolecules using high spin-lock field strengths with a cryogenically cooled probehead, Journal of magnetic resonance (San Diego, Calif. : 1997), 221 (2012) 1–4.

[220]. Boyd J, Hommel U, Krishnan VV, Influence of Cross-Correlation Between Dipolar and Chemical Shift Anisotropy Relaxation Mechanisms Upon the Transverse Relaxation Rates of ^{15}N in Macromolecules, Chemical Physics Letters, 187 (1991) 317–324.

[221]. Kumar A, Grace RCR, Madhu PK, Cross-correlations in NMR, Prog. NMR Spectroscopy, 37 (2000) 191–319.

[222]. Steiner E, Schlagnitweit J, Lundstrom P, Petzold K, Capturing Excited States in the Fast-Intermediate Exchange Limit in Biological Systems Using (1) H NMR Spectroscopy, Angewandte Chemie (International ed. in English), 55 (2016) 15869–15872. [PubMed: 27860024]

[223]. Schlagnitweit J, Steiner E, Karlsson H, Petzold K, Efficient Detection of Structure and Dynamics in Unlabeled RNAs: The SELOPE Approach, Chem. Eur. J, 24 (2018) 6067–6070. [PubMed: 29504639]

[224]. Piotto M, Saudek V, Sklenar V, Gradient -tailored excitation for single-quantum NMR spectroscopy of aqueous solutions, J. Biomol. NMR, 2 (1992) 661–665. [PubMed: 1490109]

[225]. More J, The Levenberg-Marquardt Algorithm: Implementation and Theory, in, Springer Verlag, 1977, pp. 105–116.

[226]. Lasdon L, Duarte A, GLover F, Laguna M, Marti R, Adaptive memory programming for constrained global optimization, Computers and Operations Research, 37 (2010) 1500–1509.

[227]. Wagenmarkes E, Farrel S, AIC model selection using Akaike weight, Bull. Rev, 11 (2004) 192–196.

[228]. Burnham KP, Anderson DR, Multimodel Inference: Understanding AIC and BIC in Model Selection, Sociol. Methods Res, 33 (2004) 261–304.

[229]. Shi H, Liu B, Nussbaumer F, Kreutz C, Al-Hashimi HM, m6A slows down the kinetics of RNA duplex hybridization, Submitted, (2019).

[230]. Bouvignies G, Hansen DF, Vallurupalli P, Kay LE, Divided-evolution-based pulse scheme for quantifying exchange processes in proteins: powerful complement to relaxation dispersion

experiments, Journal of the American Chemical Society, 133 (2011) 1935–1945. [PubMed: 21244030]

[231]. Miloushev VZ, Palmer AG 3rd, R(1rho) relaxation for two-site chemical exchange: general approximations and some exact solutions, Journal of magnetic resonance (San Diego, Calif. : 1997), 177 (2005) 221–227.

[232]. Coman D, Russu IM, A nuclear magnetic resonance investigation of the energetics of basepair opening pathways in DNA, Biophysical journal, 89 (2005) 3285–3292. [PubMed: 16126830]

[233]. Vallurupalli P, Chakrabarti N, Pomes R, Kay LE, Atomistic picture of conformational exchange in a T4 lysozyme cavity mutant: an experiment-guided molecular dynamics study, Chem Sci, 7 (2016) 3602–3613. [PubMed: 30008994]

[234]. Findeisen M, Brand T, Berger S, A 1H-NMR thermometer suitable for cryoprobes, Magnetic resonance in chemistry : MRC, 45 (2007) 175–178. [PubMed: 17154329]

[235]. Zhou H, Kimsey IJ, Nikolova EN, Sathyamoorthy B, Grazioli G, McSally J, Bai T, Wunderlich CH, Kreutz C, Andricioaei I, Al-Hashimi HM, m(1)A and m(1)G disrupt ARNA structure through the intrinsic instability of Hoogsteen base pairs, Nature structural & molecular biology, 23 (2016) 803–810.

[236]. Neudecker P, Zarrine-Afsar A, Davidson AR, Kay LE, Phi-value analysis of a three-state protein folding pathway by NMR relaxation dispersion spectroscopy, Proceedings of the National Academy of Sciences of the United States of America, 104 (2007) 15717–15722. [PubMed: 17898173]

[237]. Kovrigin EI, Loria JP, Characterization of the Transition State of Functional Enzyme Dynamics, J. Am. Chem. Soc, 128 (2006) 7724–7725. [PubMed: 16771471]

[238]. Lam SL, Chi LM, Use of chemical shifts for structural studies of nucleic acids, Progress in nuclear magnetic resonance spectroscopy, 56 (2010) 289–310. [PubMed: 20633356]

[239]. Fonville JM, Swart M, Vokacova Z, Sychrovsky V, Sponer JE, Sponer J, Hilbers CW, Bickelhaupt FM, Wijmenga SS, Chemical shifts in nucleic acids studied by density functional theory calculations and comparison with experiment, Chemistry (Weinheim an der Bergstrasse, Germany), 18 (2012) 12372–12387.

[240]. Xu XP, Au-Yeung SCF, Investigation of chemical shift and structure relationships in nucleic acids using NMR and density functional theory methods, Journal of Physical Chemistry B, 104 (2000) 5641–5650.

[241]. Greene KL, Wang Y, Live D, Influence of the glycosidic torsion angle on 13C and 15Nshifts in guanosine nucleotides: Investigations of G-tetrad models with alternating syn and anti bases, J. Biomol. NMR, 5 (1995) 333–338. [PubMed: 7647551]

[242]. Rossi P, Harbison GS, Calculation of 13C chemical shifts in rna nucleosides: structure-13C chemical shift relationships, Journal of magnetic resonance (San Diego, Calif. : 1997), 151 (2001) 1–8.

[243]. Ghose R, Marino JP, Wiberg KB, Prestegard JH, Dependence of C-13 Chemical-Shifts On Glycosidic Torsional Angles in Ribonucleic-Acids, Journal of the American Chemical Society, 116 (1994) 8827–8828.

[244]. Ebrahimi M, Rossi P, Rogers C, Harbison GS, Dependence of 13C NMR chemical shifts on conformations of rna nucleosides and nucleotides, Journal of magnetic resonance (San Diego, Calif. : 1997), 150 (2001) 1–9.

[245]. Santos RA, Tang P, Harbison GS, Determination of DNA sugar pucker using 13C NMR Spectroscopy, Biochemistry, 28 (1989) 9372–9378. [PubMed: 2611236]

[246]. Dejaegere AP, Case DA, Density functional study of ribose and deoxyribose chemical shifts, Journal of Physical Chemistry A, 102 (1998) 5280–5289.

[247]. Ohlenschlager O, Haumann S, Ramachandran R, Gorlach M, Conformational signatures of 13C chemical shifts in RNA ribose, Journal of biomolecular NMR, 42 (2008) 139–142. [PubMed: 18807198]

[248]. Fares C, Amata I, Carlomagno T, 13C-detection in RNA bases: revealing structure-chemical shift relationships, Journal of the American Chemical Society, 129 (2007) 15814–15823. [PubMed: 18052161]

[249]. Goswami B, Gaffney BL, Jones RA, Nitrogen-15-labeled oligodeoxynucleotides. 5. Use of 15N NMR to probe H-bonding in an O6MeG.cntdot.T base pair, Journal of the American Chemical Society, 115 (1993) 3832–3833.

[250]. Gaffney BL, Kung P, Wang C, Jones RA, Nitrogen-15-Labeled Oligodeoxynucleotides. 8. Use of 15N NMR To Probe Hoogsteen Hydrogen Bonding at Guanine and Adenine N7 Atoms of a DNA Triplex, Journal of the American Chemical Society, 117 (1995) 12281–12283.

[251]. Wang C, Gao H, Gaffney BL, Jones RA, Nitrogen-15-Labeled Oligodeoxynucleotides. 3. Protonation of the Adenine N1 in the A.G and A-C mispairs of the Duplexes d[CG(15N1)AGAATTCCCG]2 and (d[CGCGAAITC(‘5N’)ACC]J, Journal of the American Chemical Society, 113 (1991) 5486–5488.

[252]. Tanaka Y, Kojima C, Yamazaki T, Kodama TS, Yasuno K, Miyashita S, Ono AM, Ono AS, Kainosho M, Kyogoku Y, Solution Structure of an RNA Duplex Including a C-U Base Pair, Biochemistry, 39 (2000).

[253]. Nixon PL, Rangan A, Kim YG, Rich A, Hoffman DW, Hennig M, Giedroc DP, Solution Structure of a Luteoviral P1–P2 Frameshifting mRNA Pseudoknot, J. Mol. Biol, 322 (2002) 621–633. [PubMed: 12225754]

[254]. Sowers LC, Eritja R, Chen FM, Khwaja T, Kaplan BE, Goodman MF, Fazakerley GV, Characterization of the high pH wobble structure of the 2-aminopurine cytosine mismatch by N-15 NMR spectroscopy, Biochem. Biophys. Res. Commun, 165 (1989) 89–92. [PubMed: 2590245]

[255]. Cho BP, Kadlubar FF, Culp SJ, Evans FE, 15N Nuclear Magnetic Resonance Studies on the Tautomerism of 8-Hydroxy-2’-deoxyguanosine, 8-Hydroxyguanosine, and Other OS-Substituted Guanine Nucleosides, Chem. Res. Toxicol, 3 (1990) 445–452. [PubMed: 2133096]

[256]. Legault P, Pardi A, Journal of the American Chemical Society, 116 (1994) 8390–8391.

[257]. Westhof E, Isostericity and tautomerism of base pairs in nucleic acids, FEBS letters, 588 (2014) 2464–2469. [PubMed: 24950426]

[258]. Leeuw HPM, Haasnoot CAG, Altona C, Empirical Correlations Between Conformational Parameters in b-D-Furanoside Fragments Derived from a Statistical Survey of Crystal Structures of Nucleic Acid Constituents, Isr J Chem, 20 (1980) 108–126.

[259]. Frank AT, Law SM, Brooks CL, A Simple and Fast Approach for Predicting H and C Chemical Shifts: Toward Chemical Shift-Guided Simulations of RNA, The journal of physical chemistry. B, (2014).

[260]. Sitkoff D, Case DA, Theories of chemical shift anisotropies in proteins and nucleic acids, Progress in NMR Spec, 32 (1998) 165–190.

[261]. Cromsight JAMTC, Hilbers CW, Wijmenga SS, Prediction of proton chemical shifts in RNA, J. Biomol. NMR, 21 (2001) 11–29. [PubMed: 11693565]

[262]. Barton S, Heng X, Johnson BA, Summers MF, Database proton NMR chemical shifts for RNA signal assignment and validation, Journal of biomolecular NMR, 55 (2013) 33–46. [PubMed: 23180050]

[263]. Altona C, Faber DH, Hoekzema AJAW, Double-helical DNA 1H chemical shifts: an accurate and balanced predictive empirical scheme, Magn. Reson. Chem, 38 (2000) 95–107.

[264]. Lee J, Dethoff EA, Al-Hashimi HM, Invisible RNA state dynamically couples distant motifs, Proceedings of the National Academy of Sciences of the United States of America, 111 (2014) 9485–9490. [PubMed: 24979799]

[265]. Zuker M, Mfold web server for nucleic acid folding and hybridization prediction, Nucleic acids research, 31 (2003) 3406–3415. [PubMed: 12824337]

[266]. Parisien M, Major F, The MC-Fold and MC-Sym pipeline infers RNA structure from sequence data, Nature, 452 (2008) 51–55. [PubMed: 18322526]

[267]. Houck-Loomis B, Durney MA, Salguero C, Shankar N, Nagle JM, Goff SP, D’Souza VM, An equilibrium-dependent retroviral mRNA switch regulates translational recoding, Nature, 480 (2011) 561–564. [PubMed: 22121021]

[268]. Reining A, Nozinovic S, Schlepckow K, Buhr F, Furtig B, Schwalbe H, Three-state mechanism couples ligand and temperature sensing in riboswitches, Nature, 499 (2013) 355–359. [PubMed: 23842498]

[269]. Merriman DK, Xue Y, Yang S, Kimsey IJ, Shakya A, Clay M, Al-Hashimi HM, Shortening the HIV-1 TAR RNA Bulge by a Single Nucleotide Preserves Motional Modes overa Broad Range of Time Scales, Biochemistry, 55 (2016) 4445–4456. [PubMed: 27232530]

[270]. Xu Y, McSally J, Andricioaei I, Al-Hashimi HM, Modulation of Hoogsteen dynamics on DNA recognition, Nature communications, 9 (2018) 1473.

[271]. Zhang Q, Stelzer AC, Fisher CK, Al-Hashimi HM, Visualizing spatially correlated dynamics that directs RNA conformational transitions, Nature, 450 (2007) 1263–1267. [PubMed: 18097416]

[272]. Frank AT, Stelzer AC, Al-Hashimi HM, Andricioaei I, Constructing RNA Dynamical Ensembles by Combining MD and Motionally Decoupled NMR RDCs: New insights into RNA Dynamics and Adaptive Ligand Recognition, Nucleic acids research, 37 (2009) 3670–3679. [PubMed: 19369218]

[273]. Salmon L, Bascom G, Andricioaei I, Al-Hashimi HM, A General Method for Constructing Atomic-Resolution RNA Ensembles using NMR Residual Dipolar Couplings: The Basis for Interhelical Motions Revealed, Journal of the American Chemical Society, 135 (2013) 5457–5466. [PubMed: 23473378]

[274]. Salmon L, Giambasu GM, Nikolova EN, Petzold K, Bhattacharya A, Case DA, Al-Hashimi HM, Modulating RNA Alignment Using Directional Dynamic Kinks: Application in Determining an Atomic-Resolution Ensemble for a Hairpin using NMR Residual Dipolar Couplings, Journal of the American Chemical Society, (2015).

[275]. Swails J, Zhu T, He X, Case DA, AFNMR: automated fragmentation quantum mechanical calculation of NMR chemical shifts for biomolecules, Journal of biomolecular NMR, 63 (2015) 125–139. [PubMed: 26232926]

[276]. Frank AT, Bae SH, Stelzer AC, Prediction of RNA 1H and 13C chemical shifts: a structure based approach, The journal of physical chemistry. B, 117 (2013) 13497–13506. [PubMed: 24033307]

[277]. Vallurupalli P, Hansen DF, Stollar E, Meirovitch E, Kay LE, Measurement of bond vector orientations in invisible excited states of proteins, Proceedings of the National Academy of Sciences of the United States of America, 104 (2007) 18473–18477. [PubMed: 18006656]

[278]. Igumenova TI, Brath U, Akke M, Palmer AG, Characterization of Chemical Exchange Using Residual Dipolar Coupling, Journal of the American Chemical Society, 129 (2007) 13396–13397. [PubMed: 17929930]

[279]. Hansen DF, Vallurupalli P, Kay LE, Quantifying Two-Bond 1HN-13CO and One-Bond 1Hr-13Cr Dipolar Couplings of Invisible Protein States by Spin-State Selective Relaxation Dispersion NMR Spectroscopy, Journal of the American Chemical Society, 130 (2008) 8397–8405. [PubMed: 18528998]

[280]. Vallurupalli P, Hansen DF, Kay LE, Probing structure in invisible protein states with anisotropic NMR chemical shifts, Journal of the American Chemical Society, 130 (2008) 2734–2735. [PubMed: 18257570]

[281]. Sekhar A, Rosenzweig R, Bouvignies G, Kay LE, Hsp70 biases the folding pathways of client proteins, Proceedings of the National Academy of Sciences of the United States of America, 113 (2016) E2794–2801. [PubMed: 27140645]

[282]. Hansen AL, Al-Hashimi HM, Insight into the CSA tensors of nucleobase carbons in RNA polynucleotides from solution measurements of residual CSA: towards new long-range orientational constraints, Journal of magnetic resonance (San Diego, Calif. : 1997), 179 (2006) 299–307.

[283]. Ying J, Grishaev A, Bryce DL, Bax A, Chemical shift tensors of protonated base carbons in helical RNA and DNA from NMR relaxation and liquid crystal measurements, Journal of the American Chemical Society, 128 (2006) 11443–11454. [PubMed: 16939267]

[284]. Ganser L, Chu CC, Bogerd HP, Kelly ML, Cullen BR, Al-Hashimi HM, Stabilizing non-native excited states as a therapeutic strategy for targeting RNA, Submitted, (2019).

[285]. Rangadurai A, Zhou H, Merriman DK, Meiser N, Liu B, Shi H, Szymanski ES, Al-Hashimi HM, Why are Hoogsteen base pairs energetically disfavored in A-RNA compared to BDNA?, Nucleic acids research, 46 (2018) 11099–11114. [PubMed: 30285154]

[286]. Kool ET, Active site tightness and substrate fit in DNA replication, Annual review of biochemistry, 71 (2002) 191–219.

[287]. Rozov A, Demeshkina N, Westhof E, Yusupov M, Yusupova G, New Structural Insights into Translational Miscoding, Trends in biochemical sciences, 41 (2016) 798–814. [PubMed: 27372401]

[288]. Watson JD, Crick FH, The structure of DNA, Cold Spring Harbor symposia on quantitative biology, 18 (1953) 123–131. [PubMed: 13168976]

[289]. Strebitzer E, Rangadurai A, Plangger R, Kremser J, Juen MA, Tollinger M, Al-Hashimi HM, Kreutz C, 5-Oxyacetic Acid Modification Destabilizes Double Helical Stem Structures and Favors Anionic Watson-Crick like cmo(5) U-G Base Pairs, Chemistry (Weinheim an der Bergstrasse, Germany), (2018).

[290]. Gracia B, Al-Hashimi HM, Bisaria N, Das R, Herschlag D, Russell R, Hidden Structural Modules in a Cooperative RNA Folding Transition, Cell reports, 22 (2018) 3240–3250. [PubMed: 29562180]

[291]. Halvorsen M, Martin JS, Broadaway S, Laederach A, Disease-associated mutations that alter the RNA structural ensemble, PLoS genetics, 6 (2010) e1001074. [PubMed: 20808897]

[292]. Kutchko KM, Sanders W, Ziehr B, Phillips G, Solem A, Halvorsen M, Weeks KM, Moorman N, Laederach A, Multiple conformations are a conserved and regulatory feature of the RB1 5' UTR, RNA (New York, N.Y.), 21 (2015) 1274–1285.

[293]. Dallaire P, Tan H, Szulwach K, Ma C, Jin P, Major F, Structural dynamics control the MicroRNA maturation pathway, Nucleic acids research, 44 (2016) 9956–9964. [PubMed: 27651454]

[294]. Alvarado LJ, LeBlanc RM, Longhini AP, Keane SC, Jain N, Yildiz ZF, Tolbert BS, D'Souza VM, Summers MF, Kreutz C, Dayie TK, Regio-selective chemical-enzymatic synthesis of pyrimidine nucleotides facilitates RNA structure and dynamics studies, Chembiochem : a European journal of chemical biology, 15 (2014) 1573–1577. [PubMed: 24954297]

[295]. Al-Hashimi HM, Majumdar A, Gorin A, Kettani A, Skripkin E, Patel DJ, Field- and phage-induced dipolar couplings in a homodimeric DNA quadruplex, relative orientation of G center dot(C-A) triad and G-tetrad motifs and direct determination of C2 symmetry axis orientation, Journal of the American Chemical Society, 123 (2001) 633–640. [PubMed: 11456575]

[296]. Bailor MH, Sun X, Al-Hashimi HM, Topology links RNA secondary structure with global conformation, dynamics, and adaptation, Science (New York, N.Y.), 327 (2010) 202–206.

[297]. Bailor MH, Mustoe AM, Brooks CL 3rd, Al-Hashimi HM, 3D maps of RNA interhelical junctions, Nature protocols, 6 (2011) 1536–1545. [PubMed: 21959236]

Highlights

- Historical account of NMR RD with a focus on nucleic acid $R_{1\rho}$ is presented
- A vector model is used to conceptually understand $R_{1\rho}$ RD
- Approaches for fitting, simulating and visualizing $R_{1\rho}$ data are described
- Application of $R_{1\rho}$ RD to study complex three-state exchange scenarios are examined
- Strategies for determining structures of nucleic acid ESs are reviewed

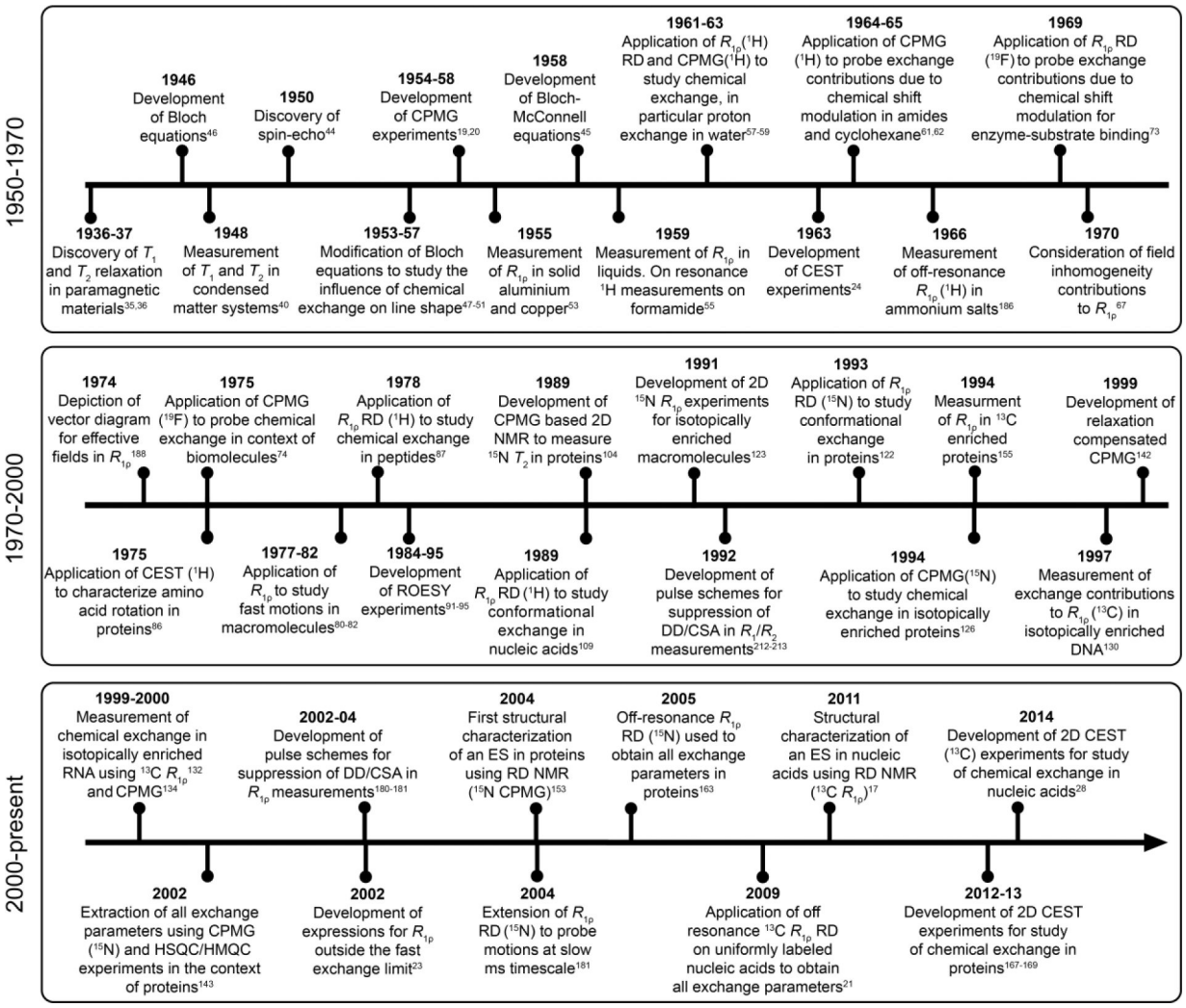

Figure 1.

Time diagram showing key developments in RD NMR techniques for characterizing chemical exchange in biomolecules with emphasis placed on $R_{1\rho}$ studies and their application to nucleic acids.

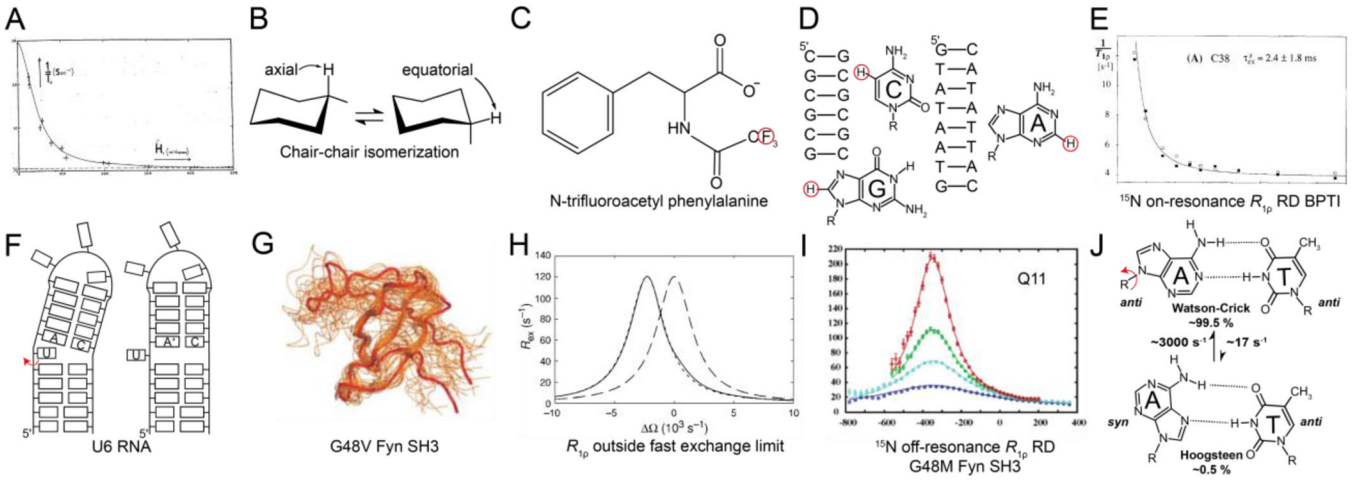

Figure 2.

Historical progression of the development of $R_{1\rho}$ RD techniques for applications to nucleic acids. A) The on-resonance $R_{1\rho}(^{1}H)$ RD profile measured for formamide by Solomon *et al.* [55] was the first reported measurement of $R_{1\rho}$ in liquids. Reproduced with permission from Bibliotheque nationale de France (BNF).B) The chair-chair inter-conversion in cyclohexane was one of the earliest conformational transitions characterized by RD methods[62, 63].C) $R_{1\rho}(^{19}F)$measurements on N-trifluoroacetyl phenylalanine in exchange between free and enzyme-bound states by Sykes *et al.*[73] constituted the first application of $R_{1\rho}$ RD in the context of biological macromolecules. D) Some of the earliest applications of $R_{1\rho}$ in studies of conformational exchange in biomolecules targeted ^{1}H nuclei (red circles) in nucleic acid duplexes in the early 1990s[109–111]. E) On-resonance $R_{1\rho}(^{15}N)$ RD profile for backbone amide ^{15}N of C38 in bovine pancreatic trypsin inhibitor was one of the first reported characterizations of conformational exchange in isotopically labeled proteins using $R_{1\rho}$[122]. Reprinted by permission from [122]. F) Secondary structure transition in U6RNA involving flipping out of a bulge nucleotide; this was one of the first validated models for ESs in nucleic acids[135]. G) First structure of an ES by Kay *et al.*[153] for a folding intermediate of the G48V mutant of the Fyn SH3 domain obtained using chemical shifts measured using CPMG RD and structurebased chemical shift calculations. Reprinted by permission from [153]. H) Expressions for $R_{1\rho}$ outside the fast exchange limit by Palmer *et al.*[23] allowed extensions of the $R_{1\rho}$ method by demonstrating the feasibility of extracting all exchange parameters at a single magnetic field. RD profiles were shown to be centered at the ES chemical shift. Simulated off-resonance profiles (for $p_{ES} = 0.048$, $k_{ex} = 1500\ s^{-1}$, $\Delta\omega = 2400$ rad s^{-1}, $R_{1,GS} = R_{1,ES} = 1.5\ s^{-1}$, $R_{2,GS} = R_{2,ES} = 11\ s^{-1}$ and $\omega_1/2\pi = 1000$ Hz) are shown using the asymmetric population expression in Palmer *et al.*[23] (dotted line) and fast exchange expression (dashed line). The exact numerical solution is shown as a solid black line. Reproduced with permission from [23]. I) Off-resonance $R_{1\rho}(^{15}N)$ RD profile for the amide ^{15}N of Q11 in a G48M mutant of the Fyn-SH3 domain; this was the first experimental measurement of off-resonance $R_{1\rho}$ using low spin-lock amplitudes and selective excitation experiments[163]. This study also represented the first instance wherein a complete set of exchange parameters was extracted using $R_{1\rho}$ measurements. Reprinted with permission from [163]. J) Excited state Hoogsteen BPs in duplex DNA were the first ESs to be

structurally characterized in nucleic acids using $R_{1\rho}$ RD.Rates and populations were obtained using off-resonance $R_{1\rho}$ experiments as described by Al-Hashimi *et al.*[115].

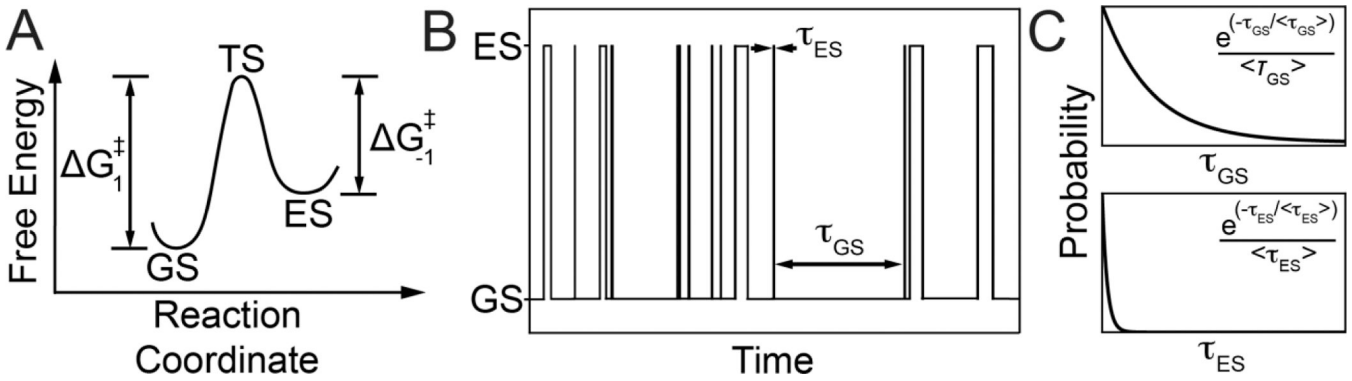

Figure 3.

Thermodynamic and kinetic characteristics of a system undergoing two-state chemical exchange. A) Free energy diagram for two-state exchange. B) Time evolution of a molecule exchanging between a dominant GS and sparsely populated and short-lived ES. C) Distribution of τ_{GS} and τ_{ES}, the dwell times for the GS and ES.

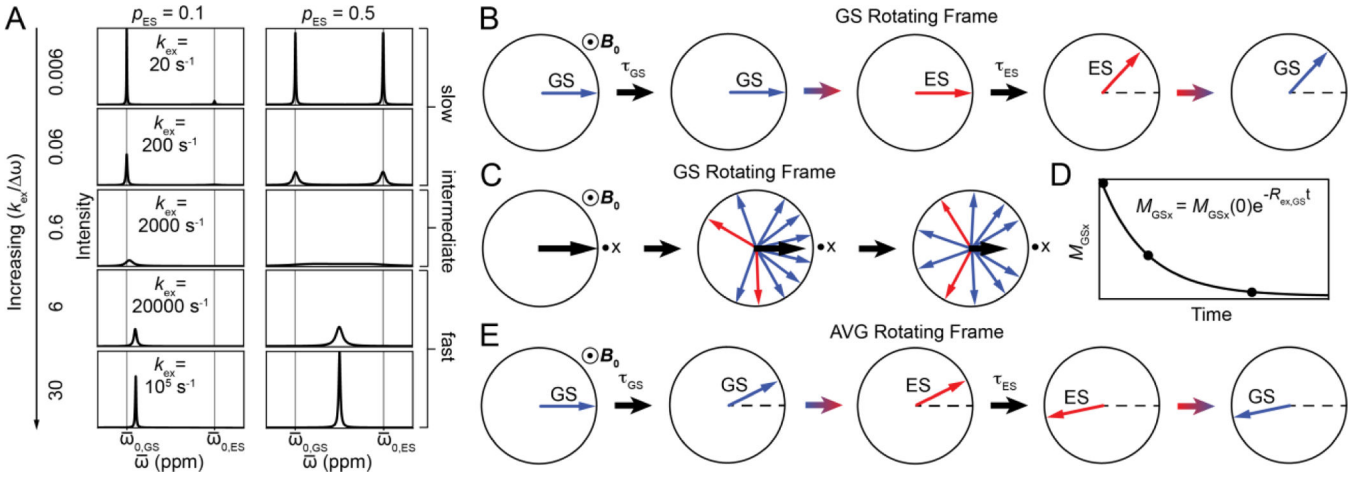

Figure 4.

Chemical exchange under free precession. A) NMR spectra for a system undergoing two-state GS-ES chemical exchange simulated using the B-M equations. Columns correspond to different values of p_{GS} while rows correspond to different values of k_{ex}. Simulations were performed assuming $\Delta\bar{\omega}$ (^{13}C) = 3 ppm, $\gamma(^1H)B_0/2\pi$ = 700 MHz and $R_{2,GS} = R_{2,ES}$ = 10 s^{-1}. B) Magnetization of GS (blue) and ES (red) spins in the rotating frame of the GS at the slow exchange limit. Black arrows represent the passage of time while colored arrows represent exchange events. Dots surrounded by circles denote vectors perpendicular to the plane of the figure. C) GS-ES chemical exchange leads to dephasing with time of the bulk magnetization corresponding to the GS (black arrow). The black dot near the x-axis corresponds to the receiver phase. D) Exponential decay due to chemical exchange of the bulk GS magnetization along the x axis (M_{GSx}) as a function of time. E) The magnetization of the GS (blue) and ES (red) spins in the rotating frame of the population-weighted average (AVG) resonance in the fast exchange limit.

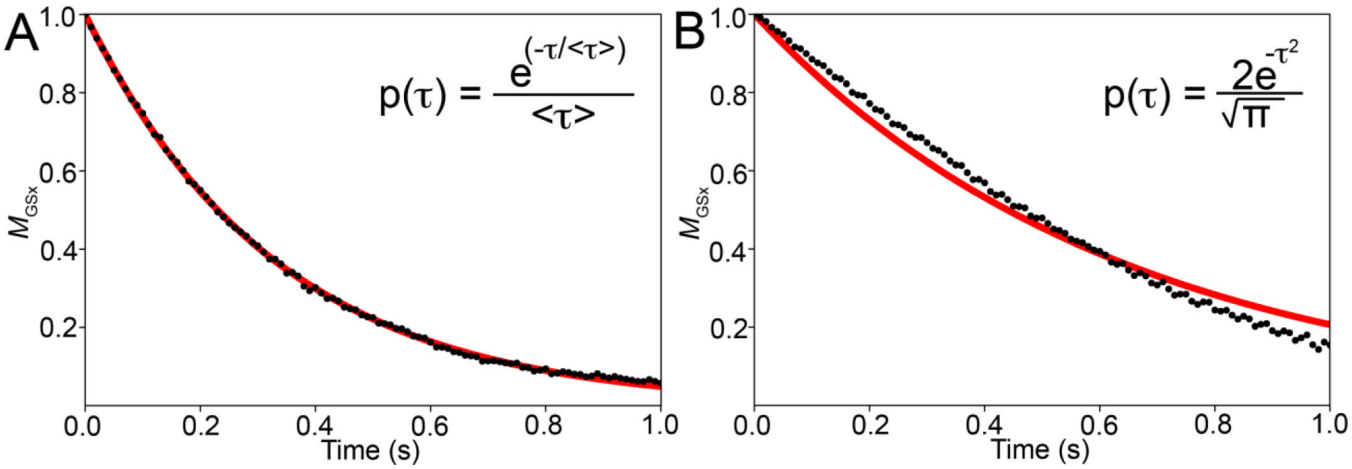

Figure 5.

The mono-exponential decay of magnetization due to chemical exchange under free precession conditions is a consequence of the exponential dwell time distributions of the GS and ES. (A and B) Normalized bulk *x*-magnetization M_{GSx} (black dots) of the GS as a function of time for a system undergoing GS-ES exchange, simulated using the vector model. An exponential fit to the magnetization is shown in red. Panel A is simulated assuming exponential probability distributions for the GS and ES dwell times ($< \tau_{GS} >$ = 0.33 s and $< \tau_{ES} >$ = 0.14 s), while panel B is simulated assuming that the ES and GS dwell times follow a standard normal distribution. Expressions for the probability distributions of τ_{GS} and τ_{ES} are given in the inset. Simulations assumed the following exchange parameters: $\Delta\bar{\omega}$ (^{13}C) = 3 ppm, $\gamma(^1\mathrm{H})B_0/2\pi$ = 700 MHz, and $R_{1,GS} = R_{1,ES} = R_{2,GS} = R_{2,ES}$ = 0 s^{-1} for panels A and B.

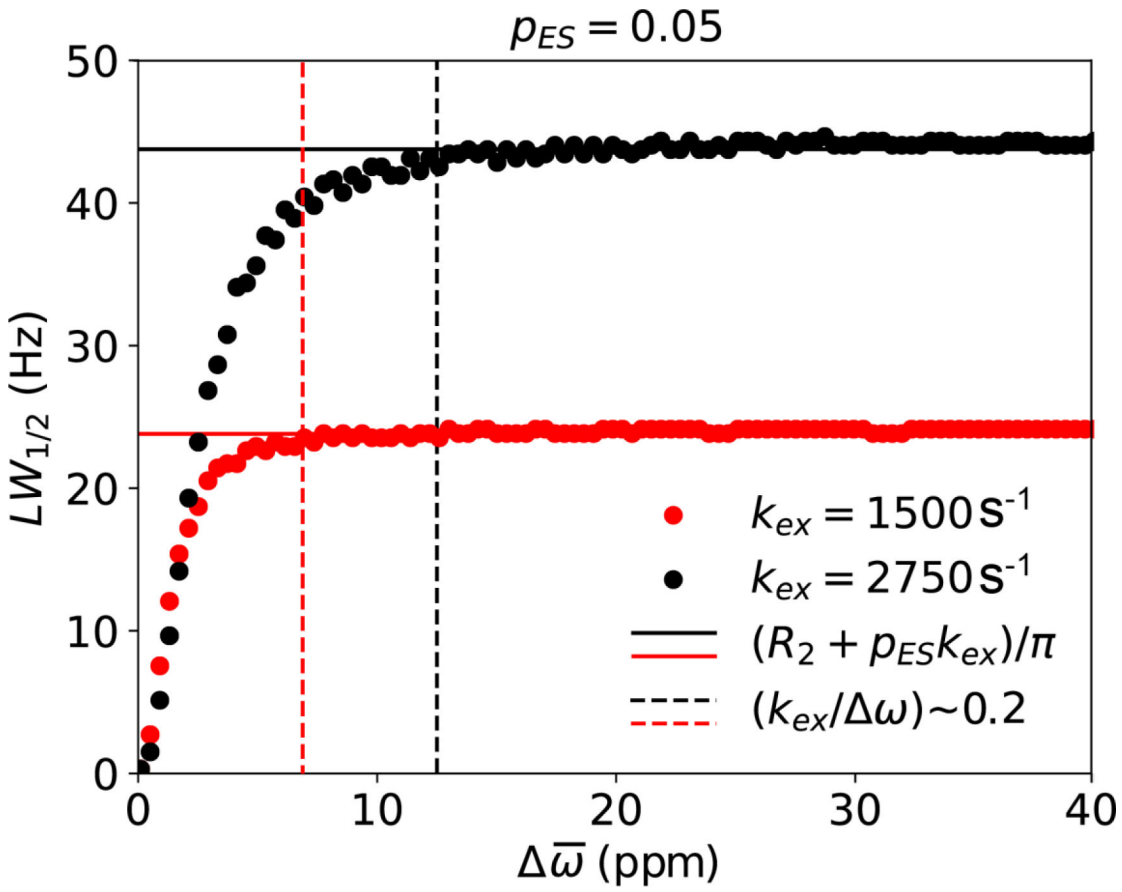

Figure 6.

Line-width at half maximum ($LW_{1/2}$, units Hz) for the dominant GS resonance as a function of $\Delta\bar{\omega}$ for a system undergoing GS-ES exchange under free precession, simulated using the B-M equations (k_{ex} = 1500 in red and k_{ex} = 2750 in black). Simulations assumed the following exchange parameters: p_{ES} = 0.05, $\gamma(^1H)B_0/2\pi$ = 700 MHz, $R_{1,GS} = R_{1,ES} = R_{2,GS} = R_{2,ES}$ = 0.0 s^{-1}, while $\Delta\bar{\omega}$ (^{13}C) was varied linearly between 0.1 and 40 ppm in 100 equally spaced increments. Solid lines denote $(R_2+p_{ES}k_{ex})/\pi$ while dotted lines denote a Δω value where $(k_{ex}/\Delta\omega) \sim 0.2$.

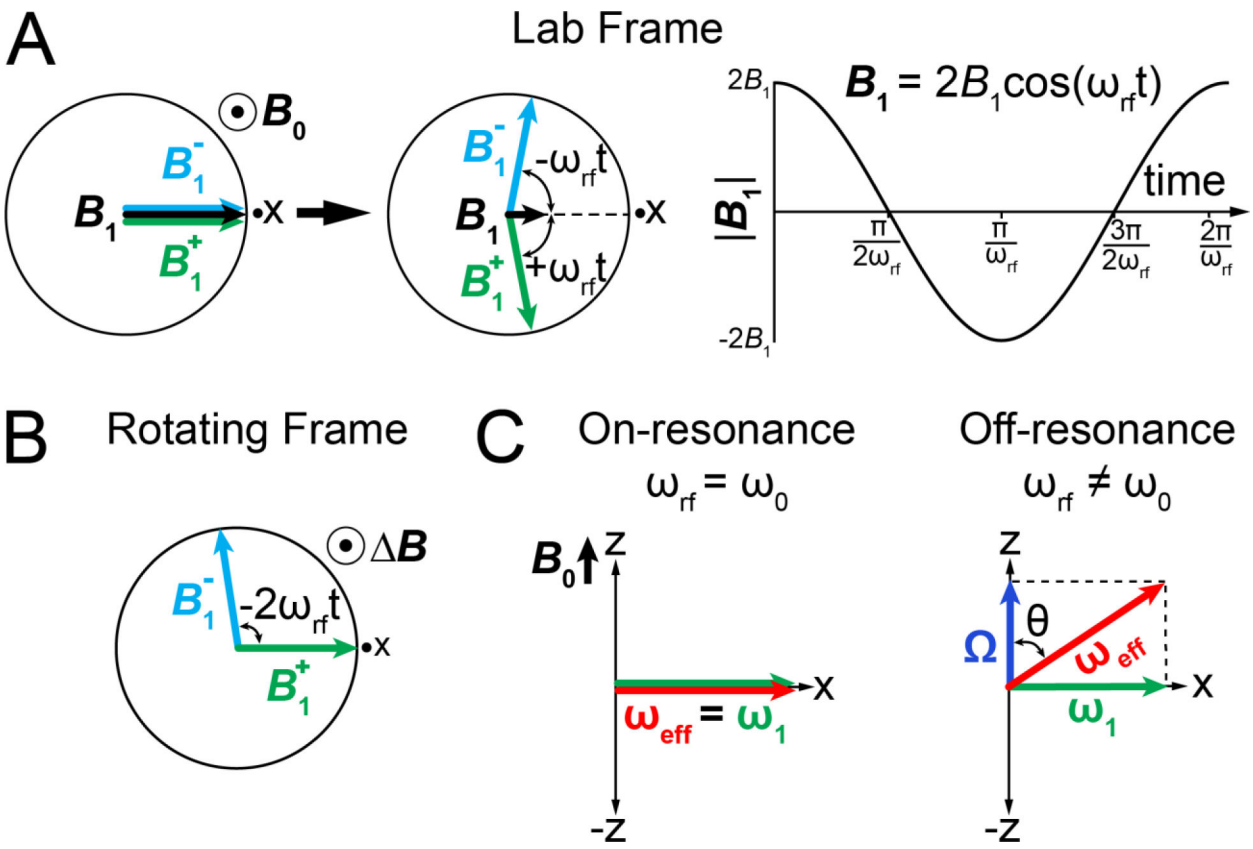

Figure 7.

Influence of the spin-locking field during an $R_{1\rho}$ experiment in the absence of chemical exchange. A) In the lab frame (left), the spin-locking field $\boldsymbol{B_1}$ (black arrow) can be decomposed into two fields $\boldsymbol{B_1^+}$ and $\boldsymbol{B_1^-}$ rotating in opposite directions (green and cyan arrows). The short black arrow represents the passage of time. A black dot surrounded by a circle represents a vector perpendicular to the plane of the figure. Black dots near the x-axes correspond to the receiver phase. ω_{rf} is the angular frequency of the spin-lock. Variation of the spin-locking field amplitude as a function of time is shown on the right. B) Evolution of $\boldsymbol{B_1^+}$ and $\boldsymbol{B_1^-}$ in the rotating frame of $\boldsymbol{B_1^+}$. The static magnetic field is reduced to ΔB. C) Effective fields under on- and off-resonance conditions in the rotating frame of the spin-lock.

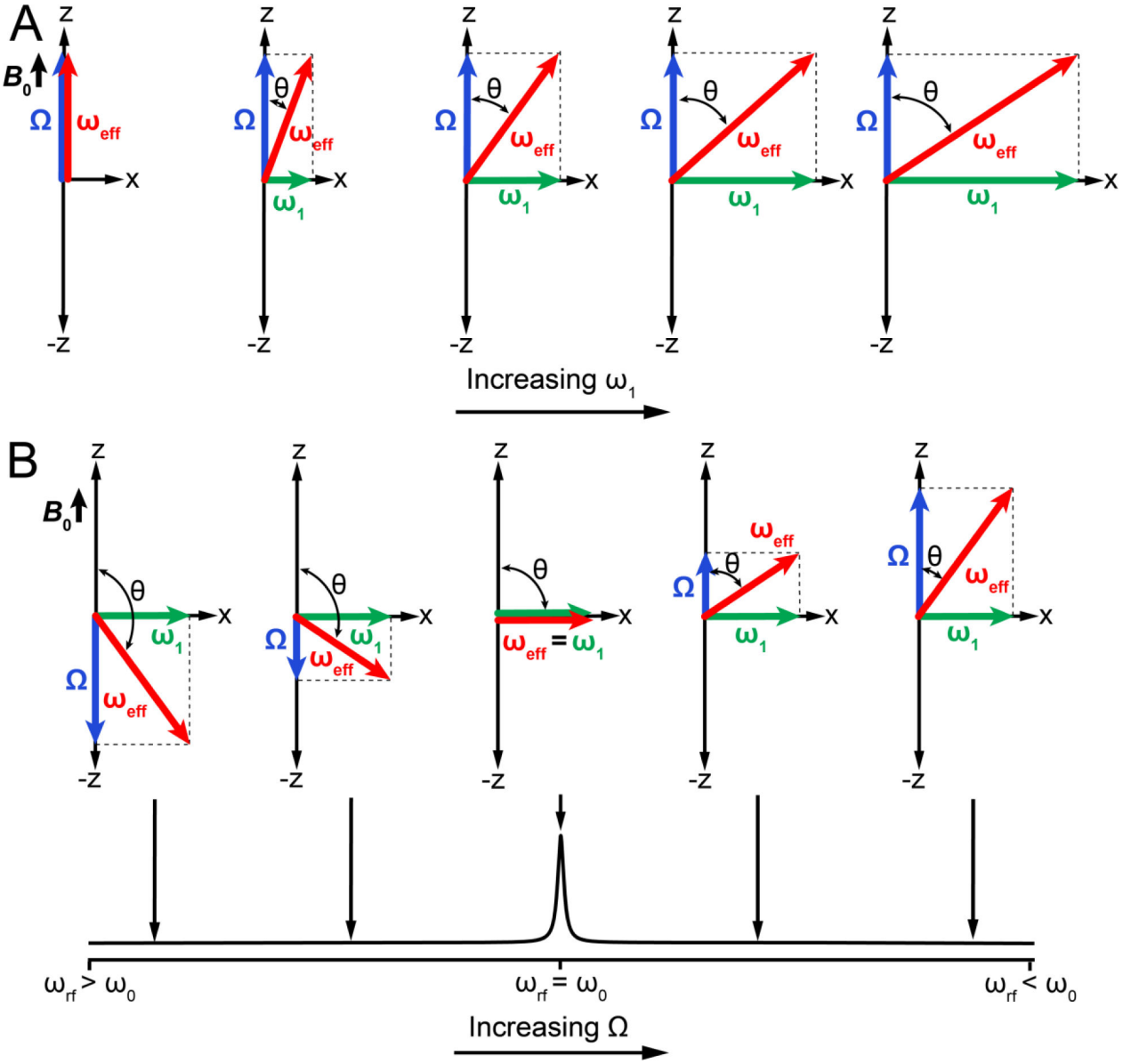

Figure 8.

Modulation of the effective field by variation of the spin-lock amplitude (ω_1) and offset frequency (Ω) in an $R_{1\rho}$ experiment in the absence of chemical exchange. Influence of changing ω_1 (A) and Ω (B) on the effective field $\boldsymbol{\omega_{eff}}$ in the rotating frame.

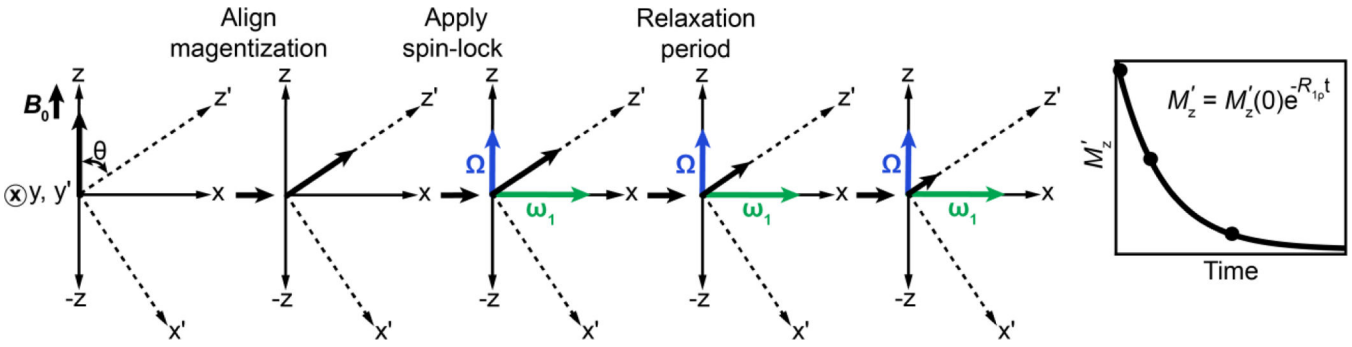

Figure 9.

Schematic representation of the $R_{1\rho}$ experiment in the absence of chemical exchange. The equilibrium magnetization tilted along z′, the direction of $\boldsymbol{\omega}_{\mathbf{eff,OBS}}$, is immediately spin-locked by the application of an RF field (green arrow), after which it decays exponentially due to relaxation with a rate constant $R_{1\rho}$. A cross within a circle denotes a vector perpendicular to the plane of the figure. All vector diagrams are in the rotating frame where the spin-locking field appears stationary.

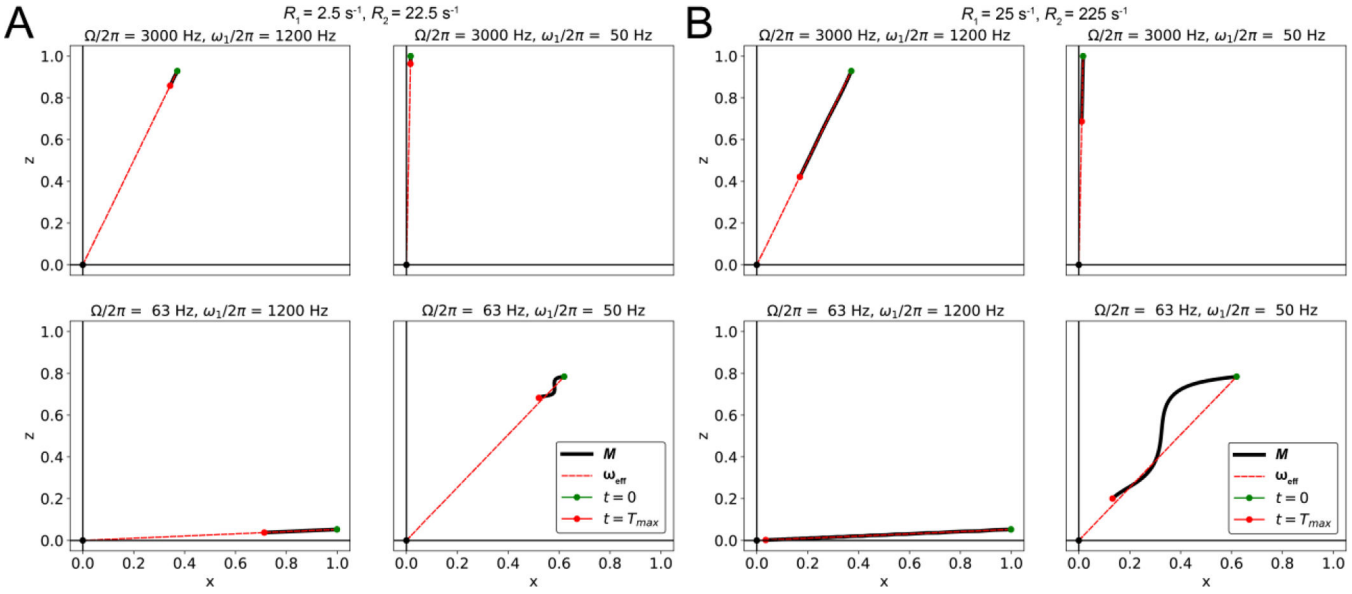

Figure 10.

Time course of the evolution of normalized magnetization during an $R_{1\rho}$ experiment in the absence of chemical exchange, as a function of the spin-lock amplitude ω_1, the offset Ω and the relaxation rates, simulated using the B-M equations. A) R_1 = 2.5 s^{-1} and R_2 = 22.5 s^{-1}; B) R_1 = 25 s^{-1} and R_2 = 225 s^{-1}. The time course for the position of the tip of the net magnetization vector ***M*** (with its base at the origin) is denoted as a solid black line, with green and red dots denoting the positions of the vector tip at the start and end (T_{max} = 0.015s) of the relaxation period, respectively. The effective field direction is denoted using a dashed red line.

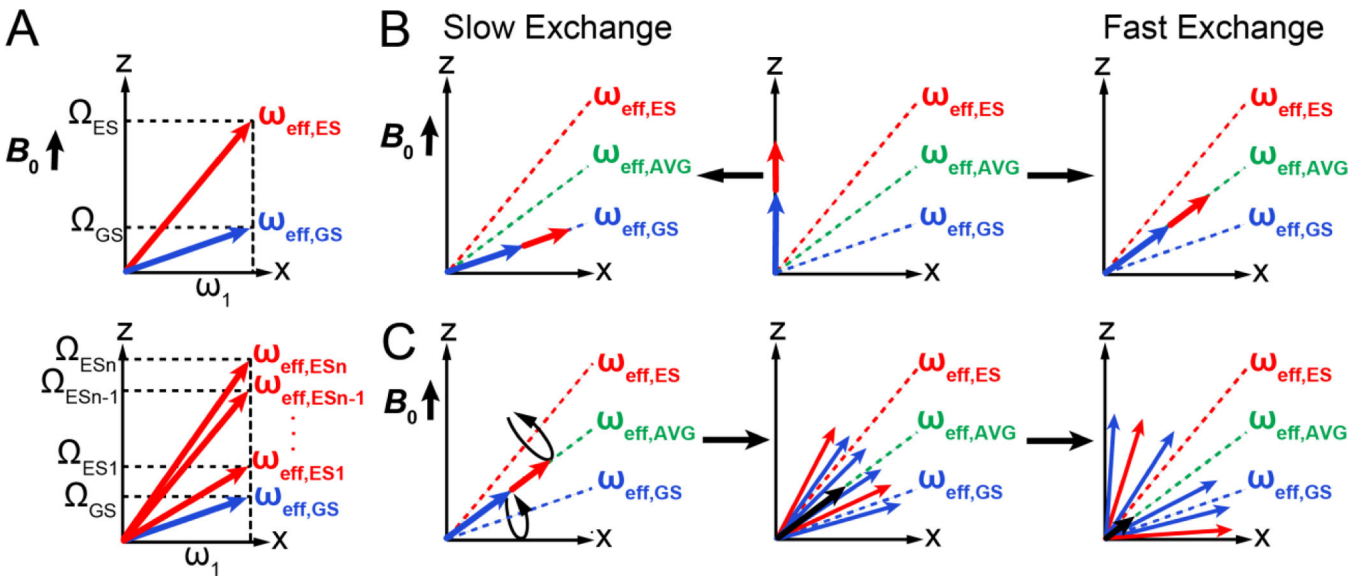

Figure 11.

$R_{1\rho}$ in the presence of chemical exchange. A) $\boldsymbol{\omega_{eff,GS}}$ (blue) and $\boldsymbol{\omega_{eff,ES}}$ (red) in the rotating frame where the spin-locking field $\boldsymbol{\omega_1}$ appears stationary, for two-state and *n*-state exchange. B) Alignment of the net magnetization at the start of an $R_{1\rho}$ experiment for a system undergoing GS-ES exchange under fast and slow exchange regimes. C) Rotation of the magnetization of GS/ES spins around their respective effective fields leads to dephasing of the bulk magnetization along $\boldsymbol{\omega_{eff,OBS}}$ during the $R_{1\rho}$ experiment. Shown is a representative example under conditions of fast exchange.

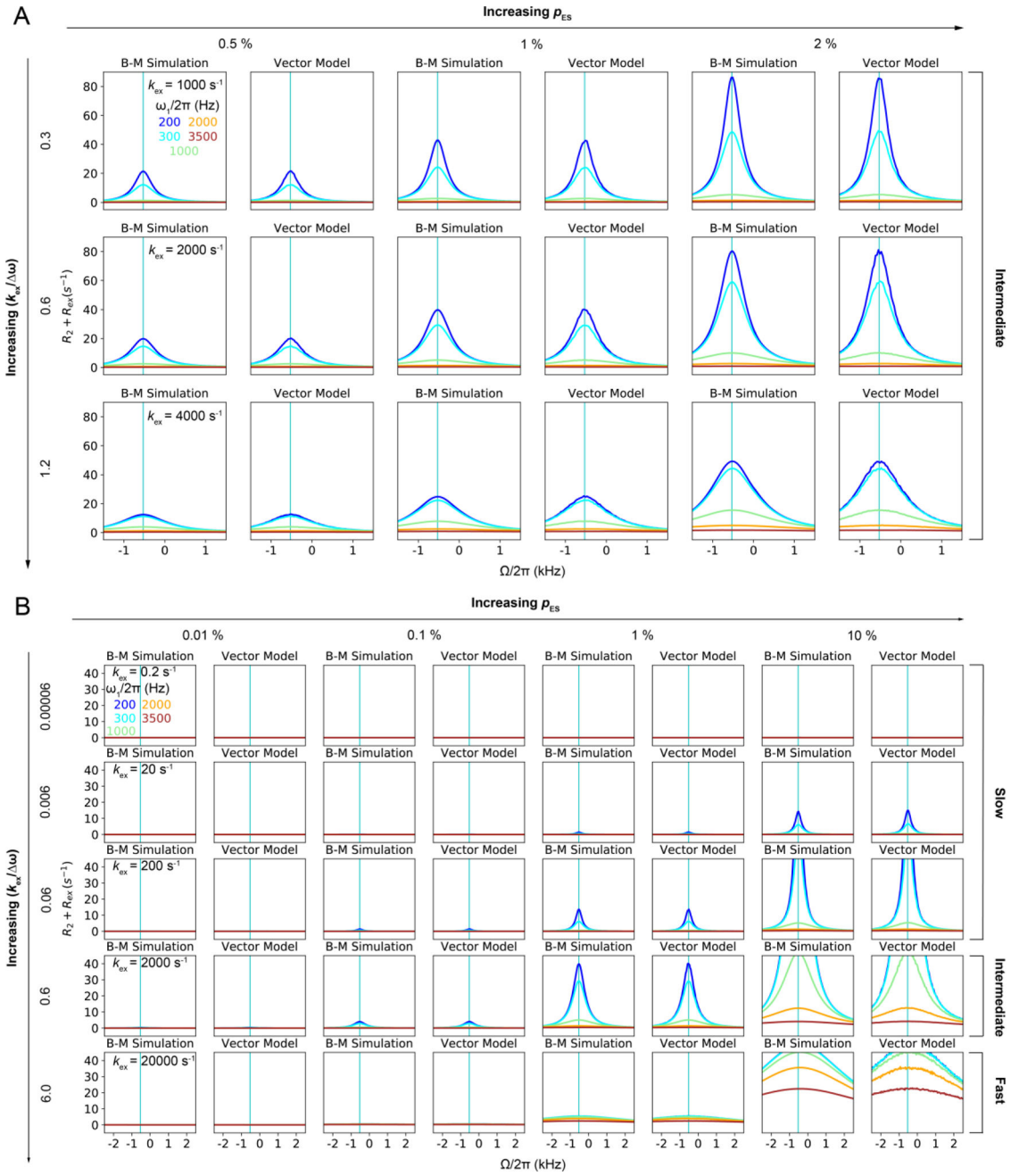

Figure 12.

Comparison of off-resonance $R_{1\rho}$ RD profiles as obtained from B-M simulations and the vector model, in the absence of relaxation, for a wide variety of exchange parameters. Rows correspond to variations in k_{ex} while columns correspond to variations in p_{ES}. Spin-lock amplitudes are color coded while solid vertical green lines correspond to an offset $\Omega = -\Delta\omega$; $\Delta\bar{\omega}(^{13}C) = 3$ ppm, $\gamma(^{1}H)B_0/2\pi = 700$ MHz. 10,000 spins were used for the vector model simulations. The initial alignment of the magnetization for the B-M and vector simulations was performed as described in Section 6.1. In the vector model simulations, the magnetization of the GS and ES spins initially aligned along $\boldsymbol{\omega}_{\mathbf{eff,OBS}}$ was allowed to

precess about $\boldsymbol{\omega}_{\mathbf{eff,GS}}$ and $\boldsymbol{\omega}_{\mathbf{eff,ES}}$ with angular velocities $\omega_{\mathrm{eff,GS}}$ and $\omega_{\mathrm{eff,ES}}$, respectively. The dwell times of the spins in the GS and ES were sampled from exponential probability distributions as described in Section 3.1, following which they were allowed to exchange with each other, while retaining the same orientation of the magnetization in 3D space prior to exchange. The sum of the magnetization of all the spins is projected along $\boldsymbol{\omega}_{\mathbf{eff,OBS}}$ as a function of time to obtain $R_{1\rho}$, which is used to obtain R_{ex}, as described in Section 3.2 – 3.4.

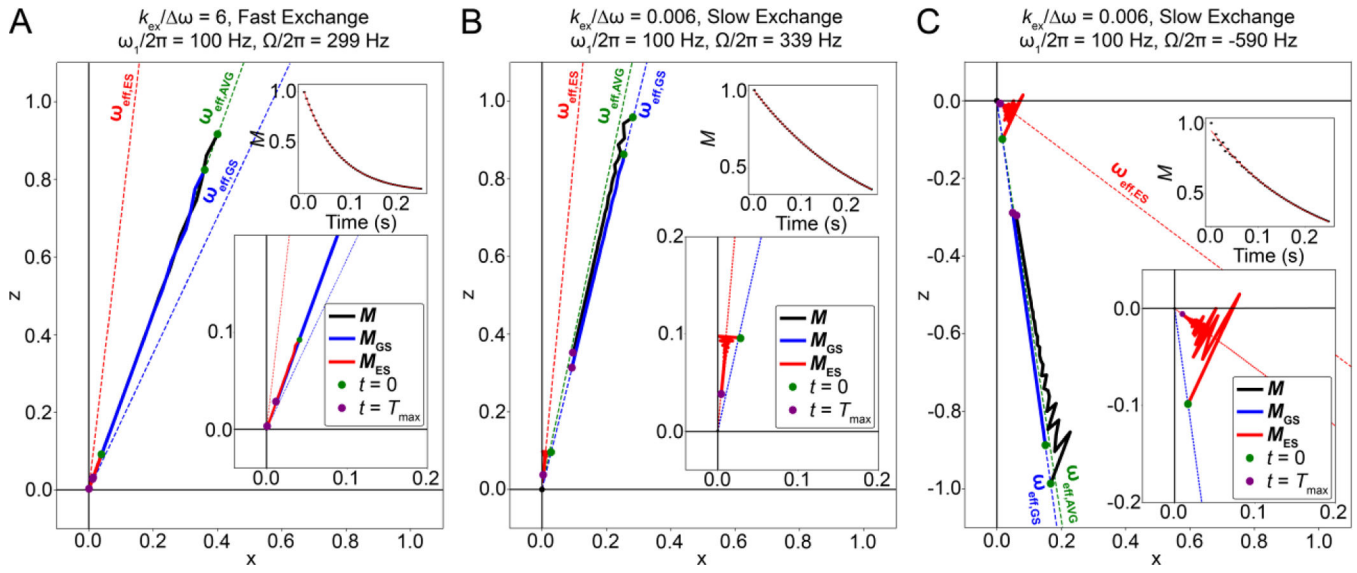

Figure 13.

Time course of the evolution of the normalized GS, ES and net magnetization during an off-resonance $R_{1\rho}$ experiment, simulated using the B-M equations. Time course for the positions of the tips of the GS, ES and net magnetization vectors (each with their base at the origin), denoted as solid blue, red and black lines respectively, with green dots in each case denoting the positions of the vector tips at the start of the relaxation period, and violet dots denoting their positions at the end of the relaxation period, respectively. Directions for the GS,ES and AVG effective fields are denoted using blue, red and green dashed lines, respectively. Also shown as insets are the variations of the normalized projections of the net magnetization along $\boldsymbol{\omega}_{\mathbf{eff,OBS}}$ (M) as a function of time (black dots), along an exponential fit of the same (red line). Simulations were performed using k_{ex} = 20000 s^{-1} for panel A, k_{ex} = 20 s^{-1} for panels B and C. The other parameters used for all simulations were p_{ES} = 0.1, $\Delta\bar{\omega}(^{13}C)$ = 3 ppm, $\gamma(^{1}H)B_0/2\pi$ = 700 MHz, $R_{1,GS} = R_{1,ES}$ = 2.5 s^{-1}, $R_{2,GS} = R_{2,ES}$ = 22.5 s^{-1} and T_{max} = 0.25 s. The initial alignment of the magnetization for the B-M and vector simulations was achieved as described in Section 6.1.

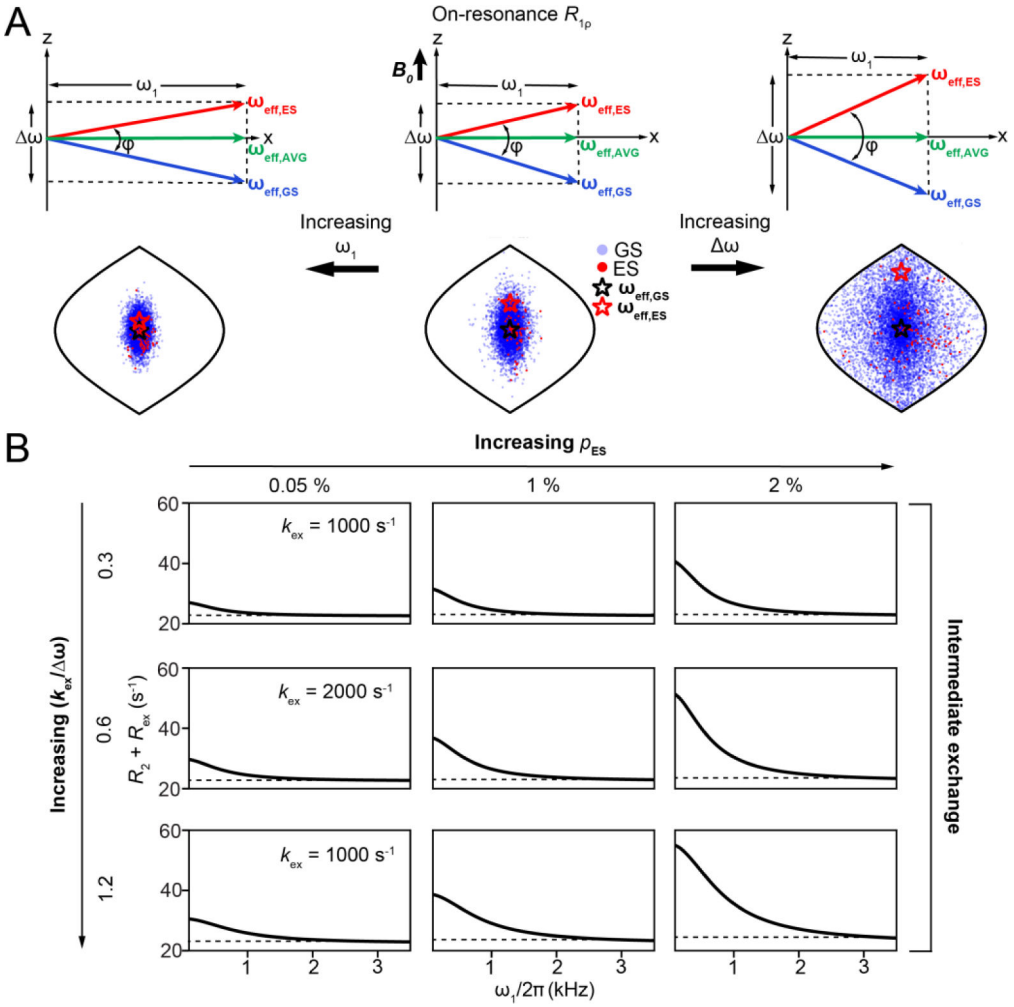

Figure 14.

Dependence of on-resonance $R_{1\rho}$ on exchange and spin-lock parameters.A) $\Delta\omega$ and ω_1 modulate R_{ex} via changes in φ, the angle between $\boldsymbol{\omega_{eff,GS}}$ and $\boldsymbol{\omega_{eff,ES}}$. Also shown are positions of the magnetization vectors corresponding to GS (blue circles) and ES (red circles) obtained using vector model simulations in the form of Sanson-Flamsteed projections[192]. $\boldsymbol{\omega_{eff,GS}}$ and $\boldsymbol{\omega_{eff,ES}}$ are indicated by black and red stars respectively. Simulations were performed with the following parameters - p_{ES} = 0.01, k_{ex} = 20,000 s^{-1}, $\Delta\bar{\omega}(^{13}C)$ = 3 ppm, $\gamma(^1H)B_0/2\pi$ = 700 MHz, $\omega_1/2\pi$ = 1000 Hz when on-resonance with the AVG state. Positions of the spins for a larger $\Delta\bar{\omega}(^{13}C)$ = 10 ppm (right) and $\omega_1/2\pi$ = 3000 Hz (left) are also shown. Simulations employed 10,000 spins with a relaxation delay of 0.012s.B) Variation of $R_2 + R_{ex}$ with ω_1 under on-resonance conditions as a function of exchange parameters, as obtained using B-M simulations. Rows and columns correspond to the indicated values of k_{ex} and p_{ES}, respectively. Dashed line denotes the value of R_2. The other exchange parameters used were $\Delta\bar{\omega}(^{13}C)$ = 3 ppm, $\gamma(^1H)B_0/2\pi$ = 700 MHz, $R_{1,GS}$= $R_{1,ES}$ = 2.5 s^{-1} and $R_{2,GS}$ = $R_{2,ES}$ = 22.5 s^{-1}. The initial alignment of the magnetization during the B-M simulations was performed as described in Section 6.1.

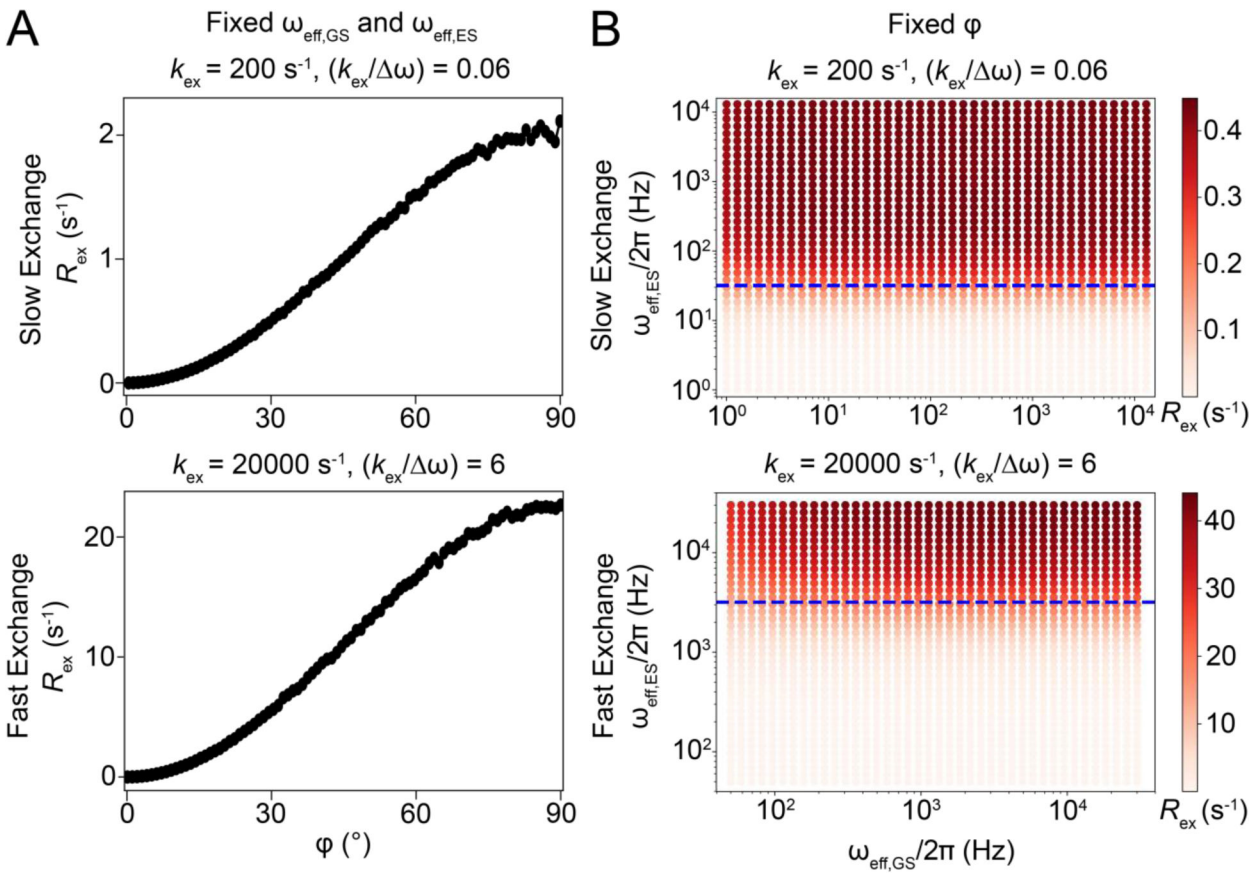

Figure 15.

Vector model simulations to illustrate the dependence of R_{ex} on φ, $\omega_{eff,GS}$ and $\omega_{eff,ES}$ during an on-resonance $R_{1\rho}$ experiment for a system undergoing two-state GS-ES exchange. A) Variation of R_{ex} with φ for a fixed $\omega_{eff,GS}$ and $\omega_{eff,ES}$, under fast and slow exchange conditions. Simulations were performed using $\omega_{eff,GS}$ = 1000*2π rad s^{-1} and $\omega_{eff,ES}$ = 1131*2π rad s^{-1} when on-resonance with the GS under slow exchange conditions. $\omega_{eff,GS}$ = 1000*2π rad s^{-1} and $\omega_{eff,ES}$ = 1128*2π rad s^{-1} under fast exchange conditions while maintaining the AVG state onresonance by suitably adjusting the offset of the GS and ES. Similar trends are observed for alternative values of the precession frequencies (data not shown). B) Heat maps of R_{ex} as a function of $\omega_{eff,GS}$ and $\omega_{eff,ES}$ for a fixed φ under fast and slow exchange conditions. Horizontal dotted lines (blue) correspond to the condition $\omega_{eff,ES}$ = k_{ex}. Orientations of the effective fields were kept fixed at those corresponding to application of $\omega_1/2\pi$ = 1000 Hz on resonance. Similar trends are also observed for $R_{1\rho}$, and for both R_{ex} and $R_{1\rho}$ under off-resonance conditions, as long as the magnetization decay is mono-exponential (data not shown). For panels A and B, simulations were performed using 10,000 spins with p_{ES} = 0.01, $\Delta\varpi(^{13}C)$ = 3 ppm, $\gamma(^1H)B_0/2\pi$ = 700 MHz, $R_{1,GS}$= $R_{1,ES}$ = 0.0 s^{-1}, $R_{2,GS}$ = $R_{2,ES}$ = 0.0 s^{-1}. The relaxation delays used were 3 s and 0.6 s for k_{ex} = 200 and 20000 s^{-1}, respectively. For both panels, the initial alignment of magnetization and its projection to calculate R_{ex}, was performed as described in Section 6.1.

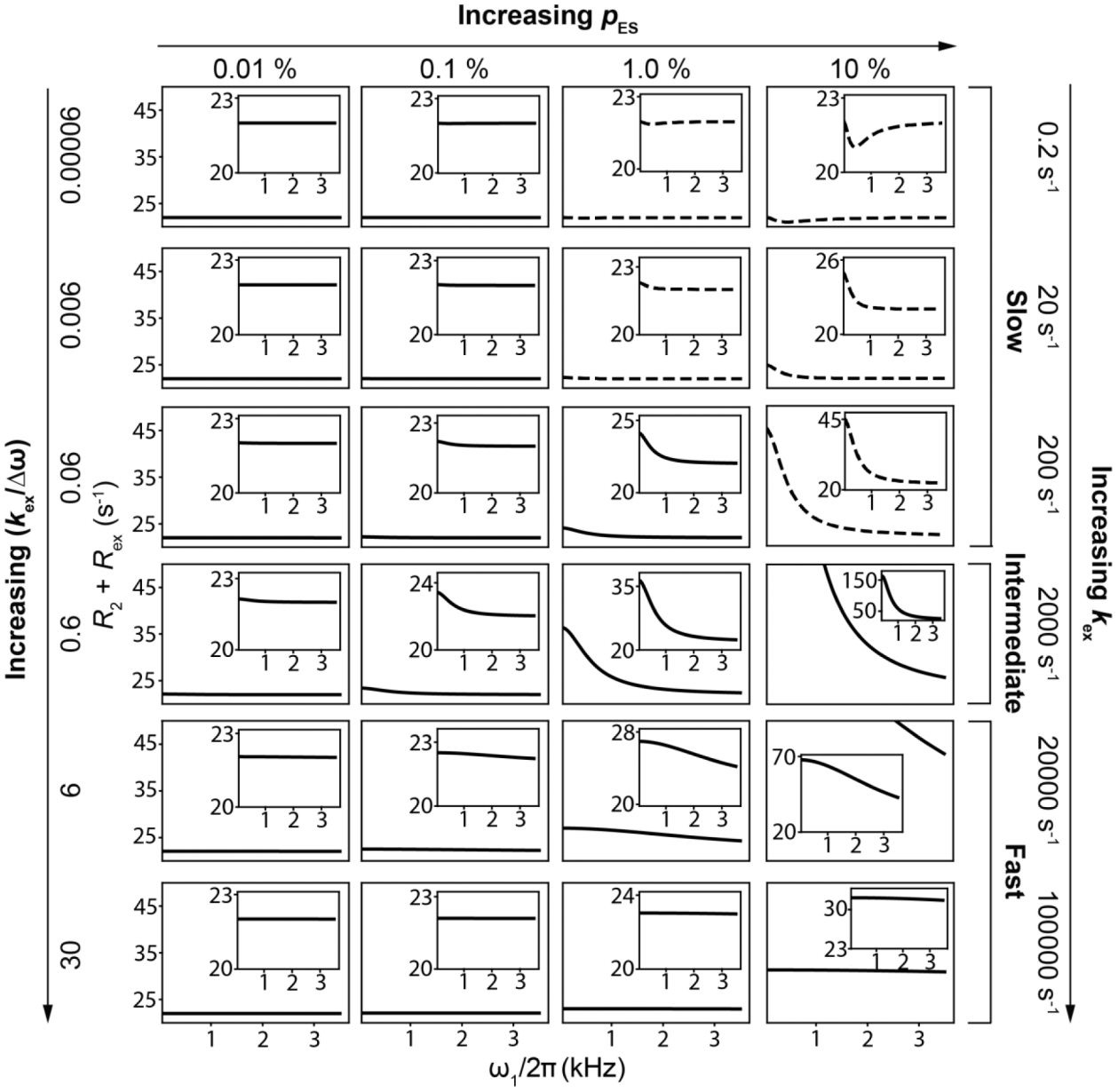

Figure 16.

Variation of $R_2 + R_{ex}$ as a function of ω_1 under on-resonance conditions as a function of exchange parameters, obtained using B-M simulations. Rows and columns correspond to the indicated values of k_{ex} and p_{ES} respectively. Panels with dotted lines correspond to exchange scenarios where the decay of the magnetization is not mono-exponential. Other parameters were: $\Delta\bar{\omega}(^{13}C) = 3$ ppm, $\gamma(^1H)B_0/2\pi = 700$ MHz, $R_{1,GS} = R_{1,ES} = 2.5\ s^{-1}$ and $R_{2,GS} = R_{2,ES} = 22.5\ s^{-1}$. The initial alignment of the magnetization was performed as described in Section 6.1.

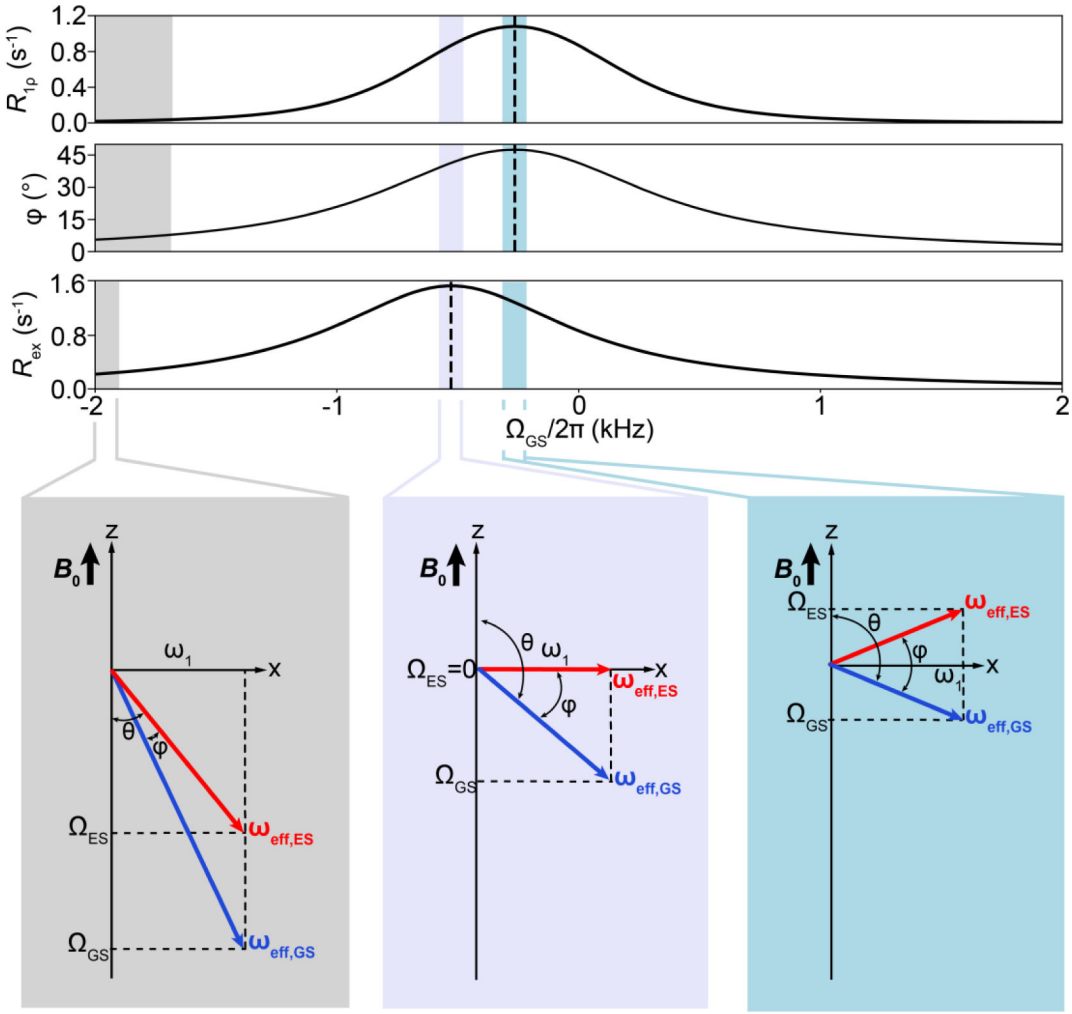

Figure 17.

Variation of $R_{1\rho}$, φ and R_{ex} with Ω_{GS} during an off-resonance $R_{1\rho}$ experiment under slow-exchange conditions with $\omega_{eff,ES} < k_{ex}$. Representative diagrams showing $\boldsymbol{\omega_{eff,GS}}$ (blue vector) and $\boldsymbol{\omega_{eff,ES}}$ (red vector) at selected offsets are also shown. The exchange parameters used were: p_{ES} = 0.01, k_{ex} = 200 s^{-1}, $\Delta\varpi(^{13}C)$ = 3 ppm, $\gamma(^1H)B_0/2\pi$ = 700 MHz, $R_{1,GS}$= $R_{1,ES}$ = 0.0 s^{-1}, $R_{2,GS}$ = $R_{2,ES}$ = 0.0 s^{-1}, $\omega_1/2\pi$ = 600 Hz along with a relaxation delay of 3.0 s. The initial alignment of the magnetization during the B-M simulation was performed as described in Section 6.1.

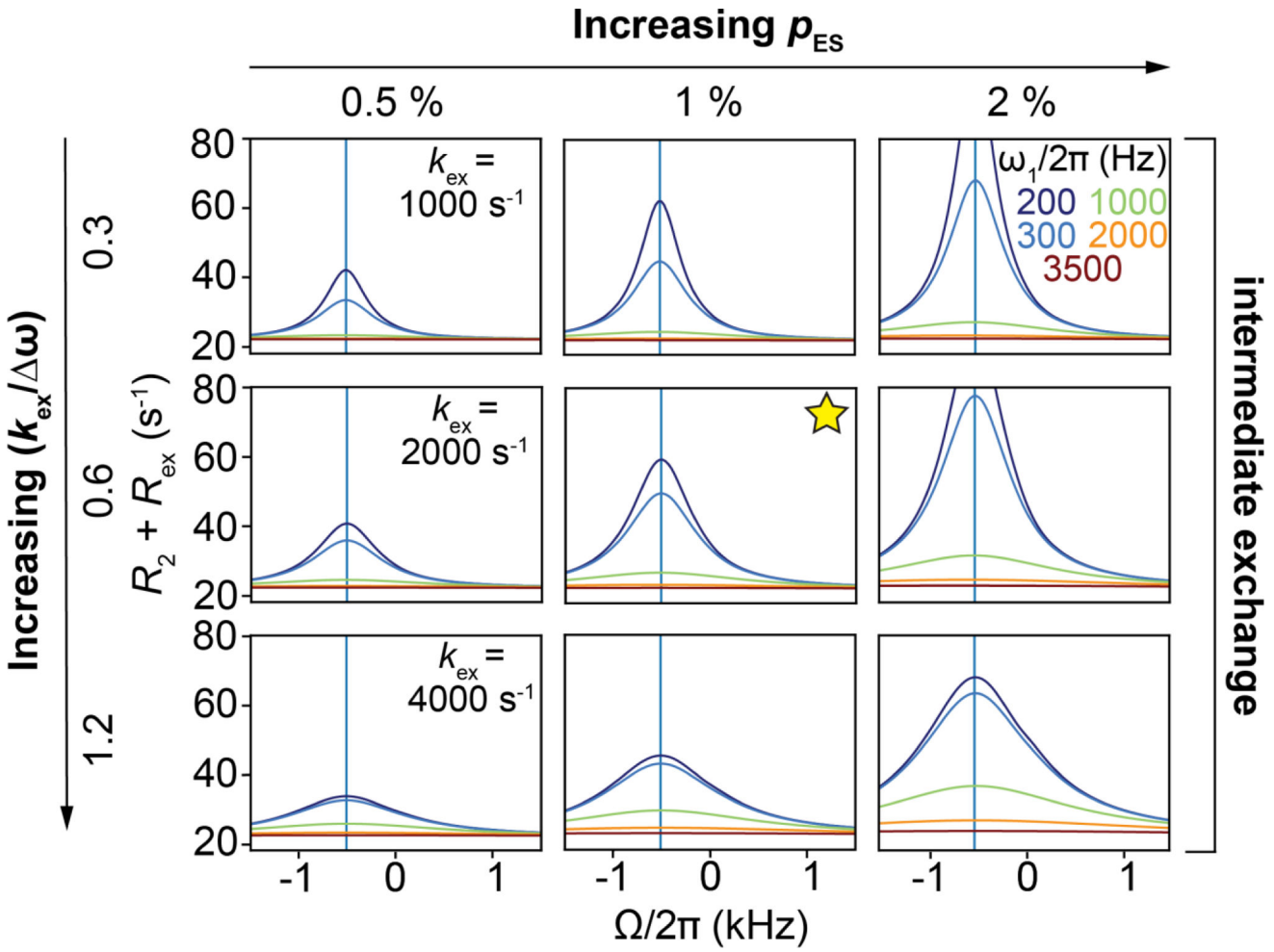

Figure 18.

Changes in $R_2 + R_{ex}$ as a function of k_{ex} and p_{ES} for two-state exchange during an off-resonance $R_{1\rho}$ experiment, simulated using the B-M equations. Horizontal comparisons show changes in k_{ex} while vertical comparisons show changes in p_{ES}. Spin-lock amplitudes are denoted using different colors. Solid gray vertical lines correspond to an offset of –Δω, while the yellow star denotes exchange parameters typical of Watson-Crick to Hoogsteen exchange in B-DNA[115]. Other exchange parameters used are: $\Delta\varpi(^{13}C) = 3$ ppm, $\gamma(^1H)B_0/2\pi = 700$ MHz, $R_{1,GS} = R_{1,ES} = 2.5$ s^{-1} and $R_{2,GS} = R_{2,ES} = 22.5$ s^{-1}. The initial alignment of the magnetization was performed as described in Section 6.1.

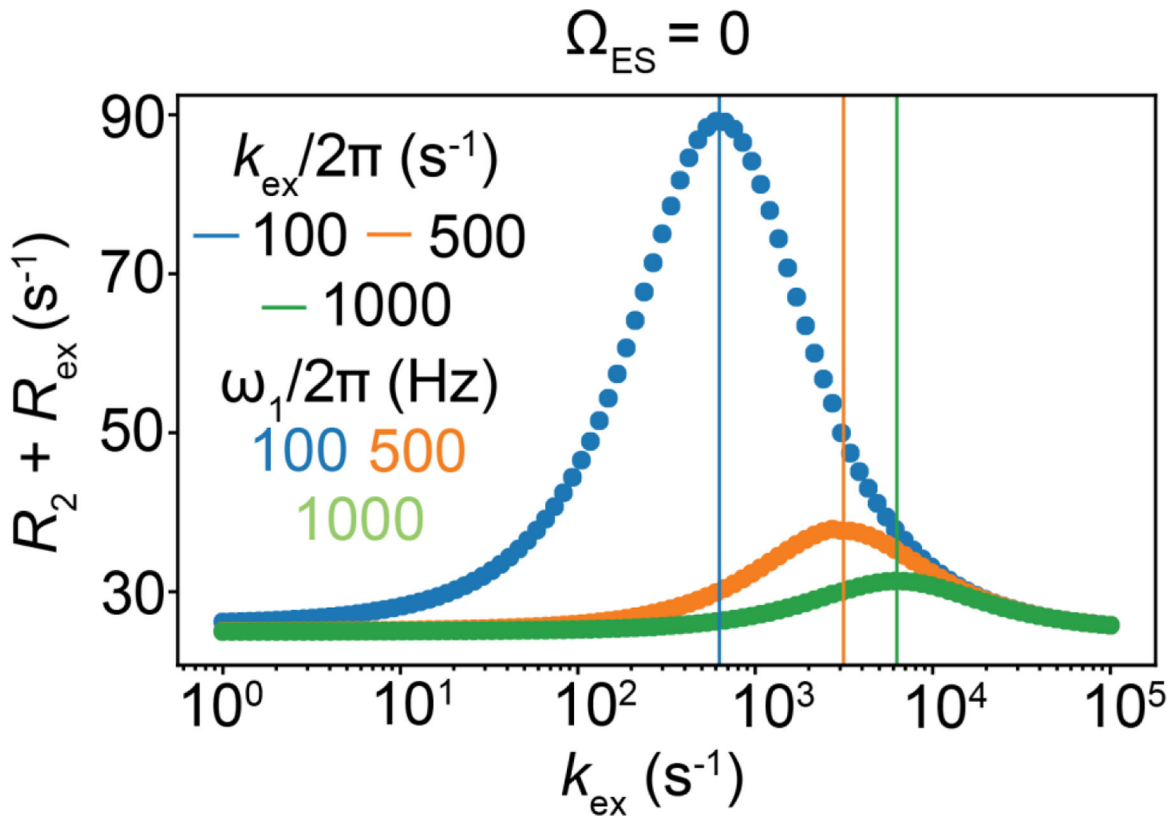

Figure 19.

Variation of $R_2 + R_{ex}$ with k_{ex} during an $R_{1\rho}$ experiment when on-resonance with the ES (p_{ES} = 0.01, $\Delta\varpi(^{13}C)$ = 3 ppm, $\gamma(^1H)B_0/2\pi$ = 700 MHz, $R_{1,GS} = R_{1,ES}$ = 2.5 s $^{-1}$ and $R_{2,GS} = R_{2,ES}$ =22.5 s^{-1}). Spin-lock amplitudes are color-coded. Vertical lines denote the indicated values of k_{ex}. The initial alignment of the magnetization during the B-M simulations was performed as described in Section 6.1.

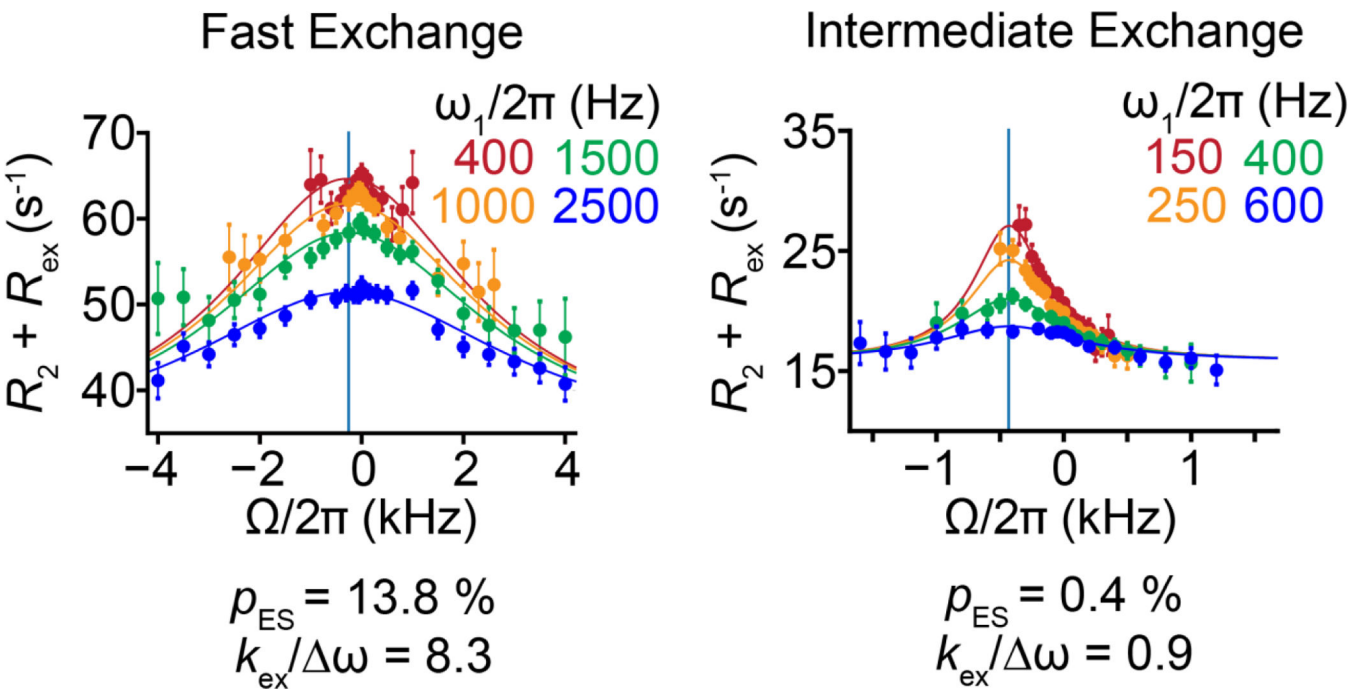

Figure 20.

Representative experimental off-resonance $R_{1\rho}$ RD profiles for two-state exchange under fast and intermediate exchange. The profiles were measured for U31-C1′ and C24-C1′ in HIV-1 TAR at 25 °C and 35 °C, respectively[166]. Spin-lock amplitudes are color-coded. Error bars represent experimental uncertainties determined by a Monte-Carlo scheme (Section 6.3). Solid lines denote global fits to the RD data using the B-M equations[166]. The initial alignment of the magnetization during the B-M fitting was performed as described in Section 6.1. Gray vertical lines correspond to the offset value when on resonance with the ES. Reproduced with permission from [166].

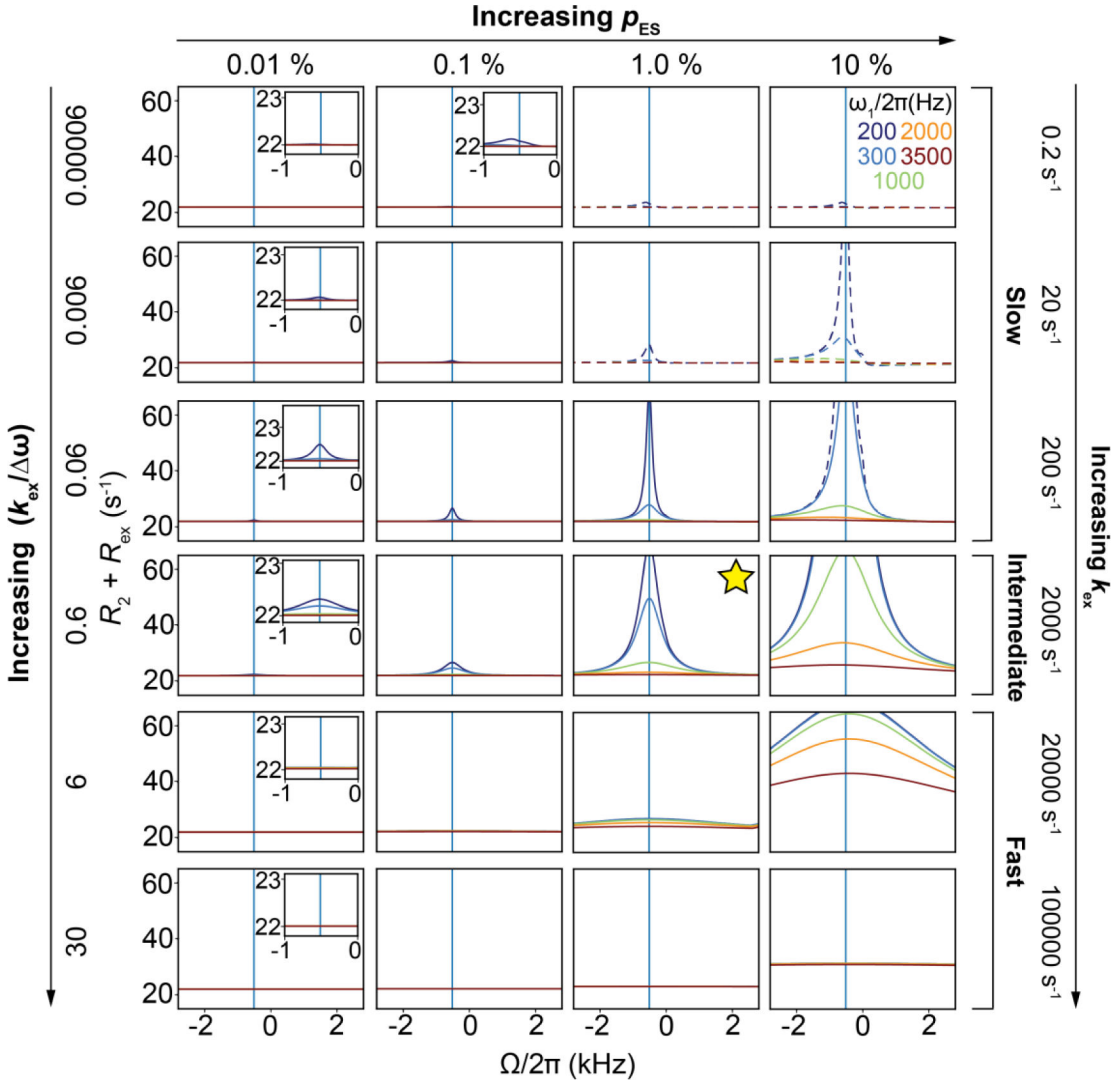

Figure 21.

Variation of $R_2 + R_{ex}$ during off-resonance $R_{1\rho}$ experiments, for a wide range of k_{ex} and p_{ES} values for two-state exchange, simulated using the B-M equations. Horizontal comparisons show changes in k_{ex} while vertical comparisons show changes in p_{ES}. Different spin-lock amplitudes are denoted by colors. Dotted lines correspond to cases where the decay of the magnetization is not mono-exponential. Solid gray vertical lines correspond to an offset of –Δω, while the yellow star denotes a typical Watson-Crick to Hoogsteen exchange scenario in DNA[115]. Simulations assumed the following parameters: $\Delta\varpi(^{13}C) = 3$ ppm, $\gamma(^1H)B_0/2\pi$ = 700 MHz, $R_{1,GS} = R_{1,ES} = 2.5\ s^{-1}$ and $R_{2,GS} = R_{2,ES} = = 22.5\ s^{-1}$. The initial alignment of the magnetization was performed as described in Section 6.1.

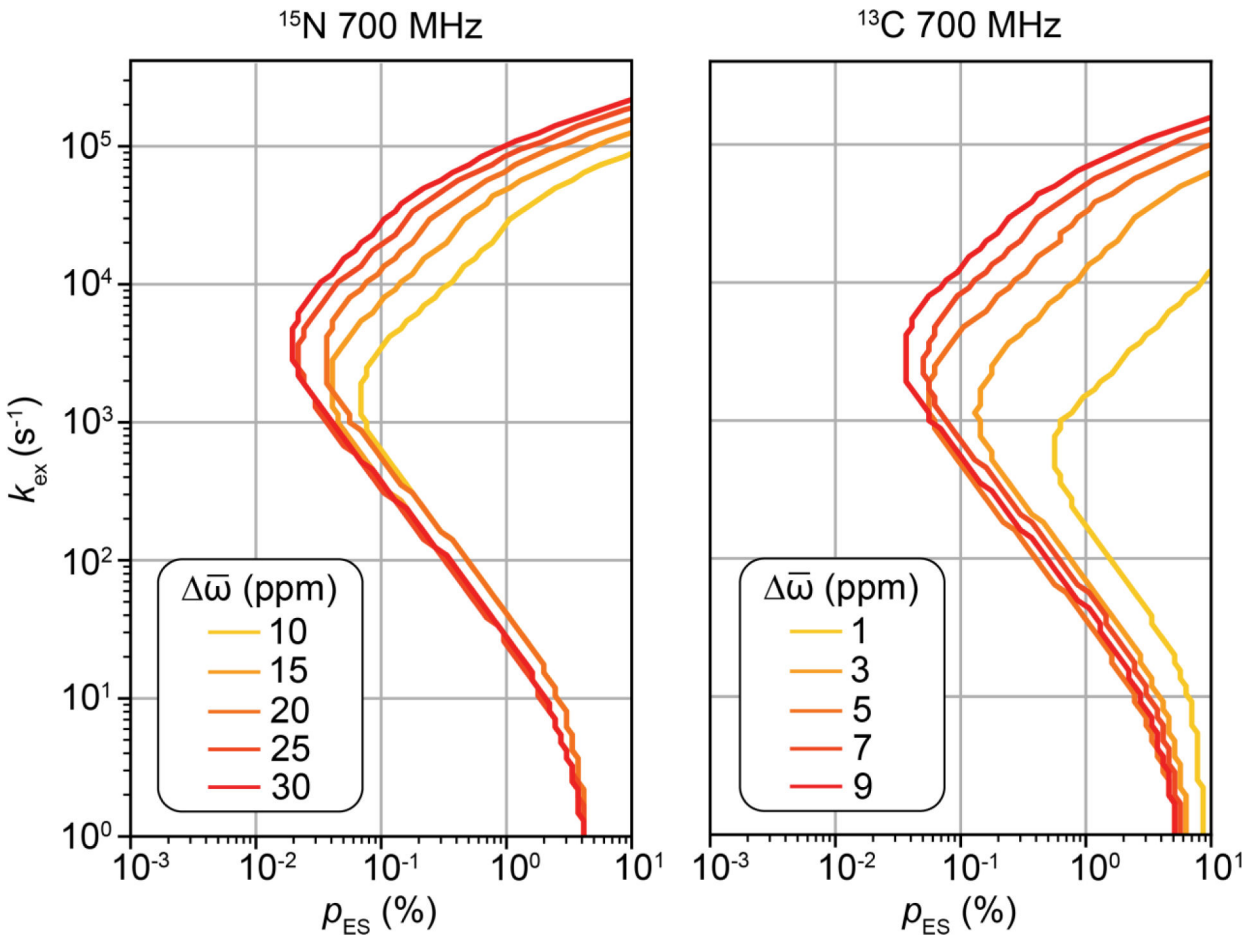

Figure 22.

Exploring the limits of the sensitivity for off-resonance $R_{1\rho}$ experiments using B-M simulations for $R_{1\rho}(^{15}N)$(left) and $R_{1\rho}(^{13}C)$ (right), at $\gamma(^{1}H)B_0/2\pi$ = 700 MHz. For each $\Delta\bar{\omega}$ value, detectability of $R_{1\rho}$ was assessed for 10,000 (p_{ES}, k_{ex}) combinations. 100 p_{ES} values ranging between 0.005 % to 20 % were chosen such that they were equally spaced on a logarithmic scale. For each of these p_{ES} values, 100 k_{ex} values ranging from 1 to 400000 s^{-1} were chosen such that they were equally spaced on a logarithmic scale. For each (p_{ES}, k_{ex}) combination, offresonance $R_{1\rho}$ RD Profiles were simulated using the B-M equations, assuming spin-locking amplitudes $\omega_1/2\pi$ = 100, 250, 500, 1000 and 2000 Hz, each with 24 offset points Ω evenly spaced such that $-3.5*\omega_1 < \Omega < +3.5*\omega_1$, without experimental error. A rate R_{ex} of at least 5 Hz above the baseline R_2 was assumed to be the threshold of detectability. The above curves were obtained by drawing a line through the lowest detectable p_{ES} for every k_{ex} value; thus all combinations of k_{ex} and p_{ES} to the right of the curves are detectable. Similar limits are observed when profiles are simulated with 5% error and re-fit to the Bloch-McConnell equations, and considered to be detectable when the fitted exchange parameters deviate from the simulated exchange parameters by less than 2-fold. For each panel, the $\Delta\bar{\omega}$ values are color-coded. For all simulations, $R_{1,GS} = R_{1,ES} = 2.5\ s^{-1}$ and $R_{2,GS} = R_{2,ES} = 22.5\ s^{-1}$. The initial alignment of the magnetization during the B-M simulations was performed as described in Section 6.1.

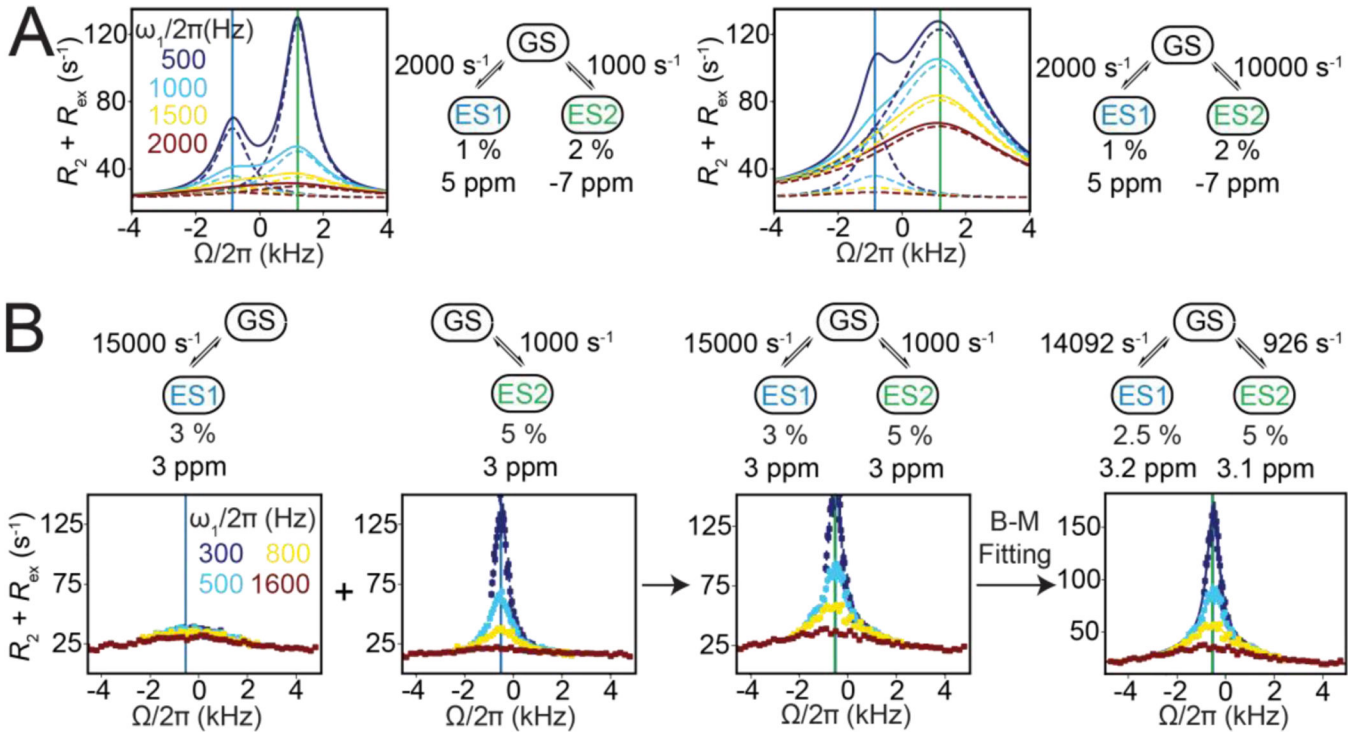

Figure 23.

Off-resonance $R_{1\rho}$ RD profiles for three-state exchange simulated using B-M equations. A) Off-resonance $R_{1\rho}$ RD profiles for three-state exchange in a star-like topology with p_{ES1} = 1 %, p_{ES2} = 2 %, $k_{ex,1}$ = 2,000 s^{-1}, $\Delta\bar{\omega}_1(^{13}C)$ = 5 ppm ^{13}C, $\Delta\bar{\omega}_2(^{13}C)$ = −7 ppm, $\gamma(^1H)B_0/2\pi$ = 700 MHz, $R_{1,GS} = R_{1,ES}$ = 2.5 s^{-1} and $R_{2,GS} = R_{2,ES}$ = 22.5 s^{-1}, with $k_{ex,2}$ = 1,000 s^{-1} (left) and kex,2 = 10,000 s^{-1} (right). Dotted lines correspond to RD profiles for individual GS-ES1 and GS-ES2 exchange, while the solid lines correspond to the RD profiles for the three-state exchange process. Solid blue and green lines correspond to offsets of $-\Delta\omega_1$ and $-\Delta\omega_2$ respectively. B) ESs exchanging in a three-state star-like topology with similar chemical shifts ($\Delta\bar{\omega}_1(^{13}C) = \Delta\bar{\omega}_2(^{13}C)$= 3 ppm, $\gamma(^1H)B_0/2\pi$ = 700 MHz) but different exchange rates and populations (p_{ES1} = 3 %, p_{ES2} = 5 %, $k_{ex,1}$ = 15000 s^{-1}, $k_{ex,2}$ = 1000 s^{-1}, $R_{1,GS} = R_{1,ES}$ = 2.5 s^{-1} and $R_{2,GS} = R_{2,ES}$ = 22.5 s^{-1}) can be resolved using off-resonance $R_{1\rho}$ RD (fitted parameters: p_{ES1} = 2.5 ± 0.4 %, p_{ES2} = 5.0 ± 0.7 %, $k_{ex,1}$= 14092 ± 1605 s^{-1}, $k_{ex,2}$= 926 ± 220 s^{-1}, $\Delta\bar{\omega}_1(^{13}C)$ = 3.2 ± 0.3 ppm and $\Delta\bar{\omega}_2(^{13}C)$ = 3.1 ± 0.7 ppm. The B-M profiles were corrupted by noise with 5 % errors in $R_{1\rho}$ prior to fitting. A vertical green line denotes an offset of $-\Delta\omega_1$. In both panels, spin-lock amplitudes are color coded. The direction of the initial alignment of the magnetization during B-M simulations was determined as described in Section 6.1, while taking into consideration the ES with the highest population.

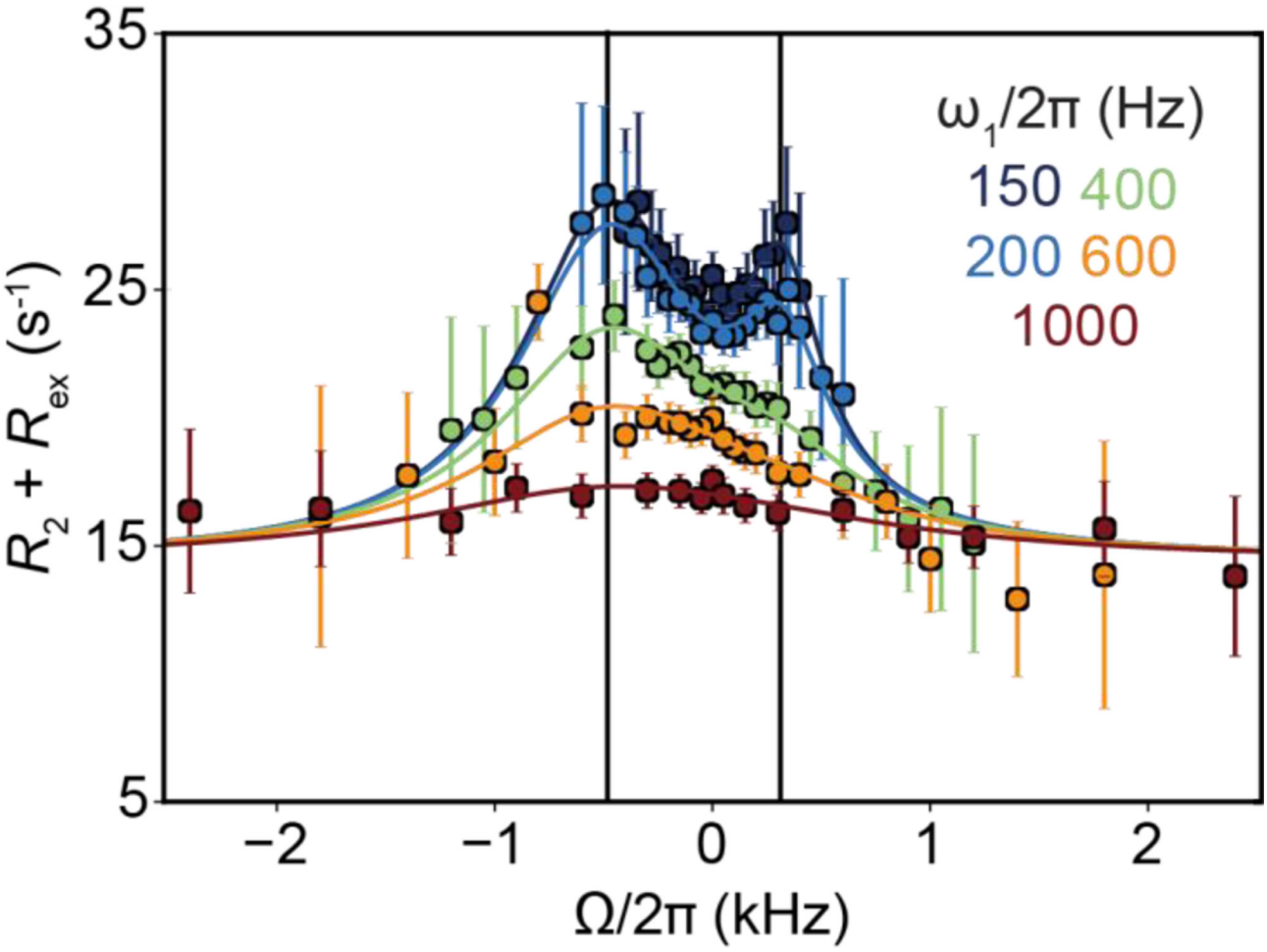

Figure 24.

Representative experimental off-resonance $R_{1\rho}$ RD profiles for a system with threestate exchange in a star-like topology. Measurements were performed on C15-C3′ in A_6-DNA at pH 6.8, 25 °C, as described by Al-Hashimi *et al.*[117]. Spin-lock amplitudes are color-coded. Error bars represent experimental uncertainties determined by a Monte-Carlo scheme (Section 6.3). Solid lines denote a global fit to the RD data[117]. The initial alignment of the magnetization during the B-M fitting was performed as described in Section 6.1, while taking into consideration the ES with the highest population. Vertical black lines correspond to offsets of $-\Delta\omega_1$ and $-\Delta\omega_2$. Reprinted by permission from [117].

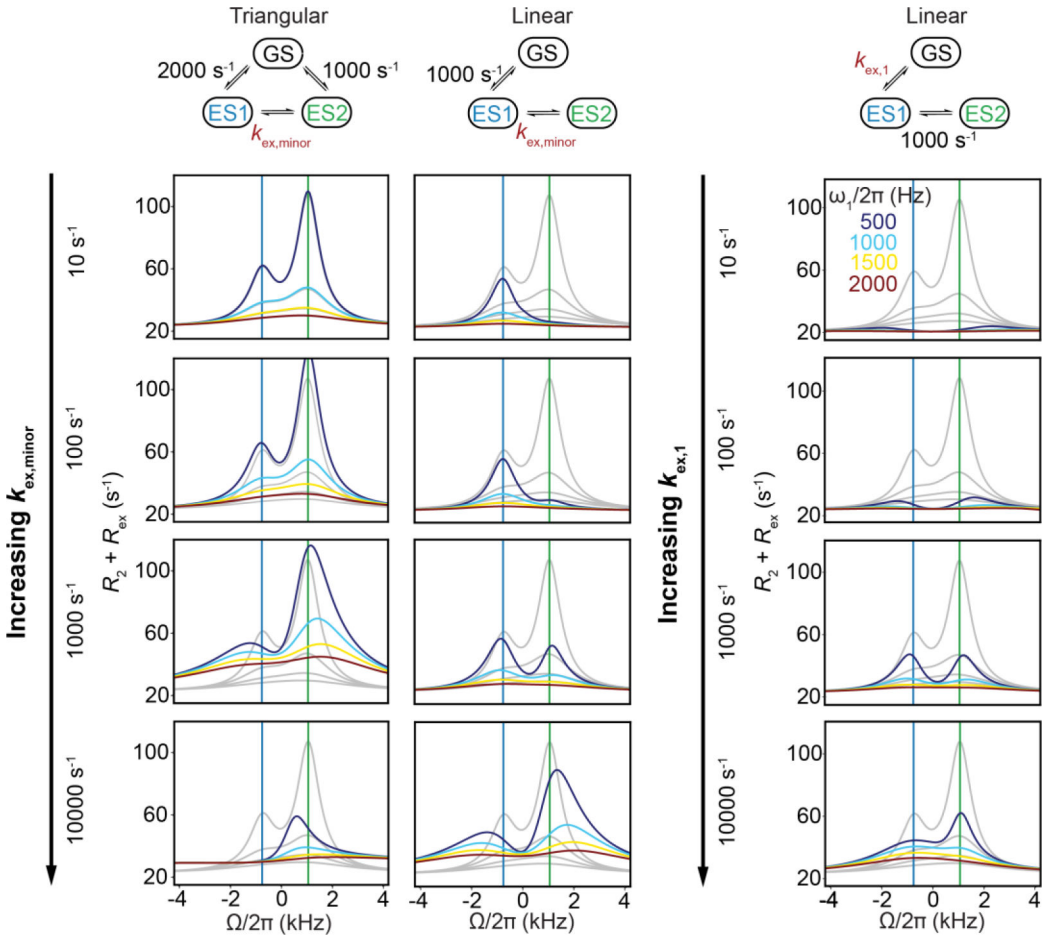

Figure 25.

Off-resonance $R_{1\rho}$ RD profiles for three-state exchange in the presence of direct "minor" exchange between the ES1 and ES2, simulated using B-M equations. Variation of offresonance $R_{1\rho}$ RD profiles for three-state exchange with triangular and linear exchange topologies as a function of $k_{ex,minor}$ and $k_{ex,1}$. Vertical blue and green lines correspond to offsets $\Delta\omega_1$ and $-\Delta\omega_2$, respectively. The RD profile in gray corresponds to three-state exchange in a star-like topology (p_{ES1} = 1 %, p_{ES2} = 2 %, $k_{ex,1}$= 2000 s^{-1}, $k_{ex,2}$ = 1000 s^{-1}, $\Delta\bar{\omega}_1(^{13}C)$ = 5 ppm, $\Delta\bar{\omega}_2(^{13}C)$ = − 7 ppm, $\gamma(^1H)B_0/2\pi$ = 700 MHz, $R_{1,GS}$ = $R_{1,ES}$ = 2.5 s^{-1} and $R_{2,GS}$ = $R_{2,ES}$ = 22.5 s^{-1}). Exchange parameters (other than k_{ex} values) for the linear exchange topologies were the same as for the star-like topology. Different spin-lock amplitudes are indicated by colors. The direction of initial alignment of the magnetization during B-M simulations was determined as described in Section 6.1, while taking into consideration the ES with the highest population.

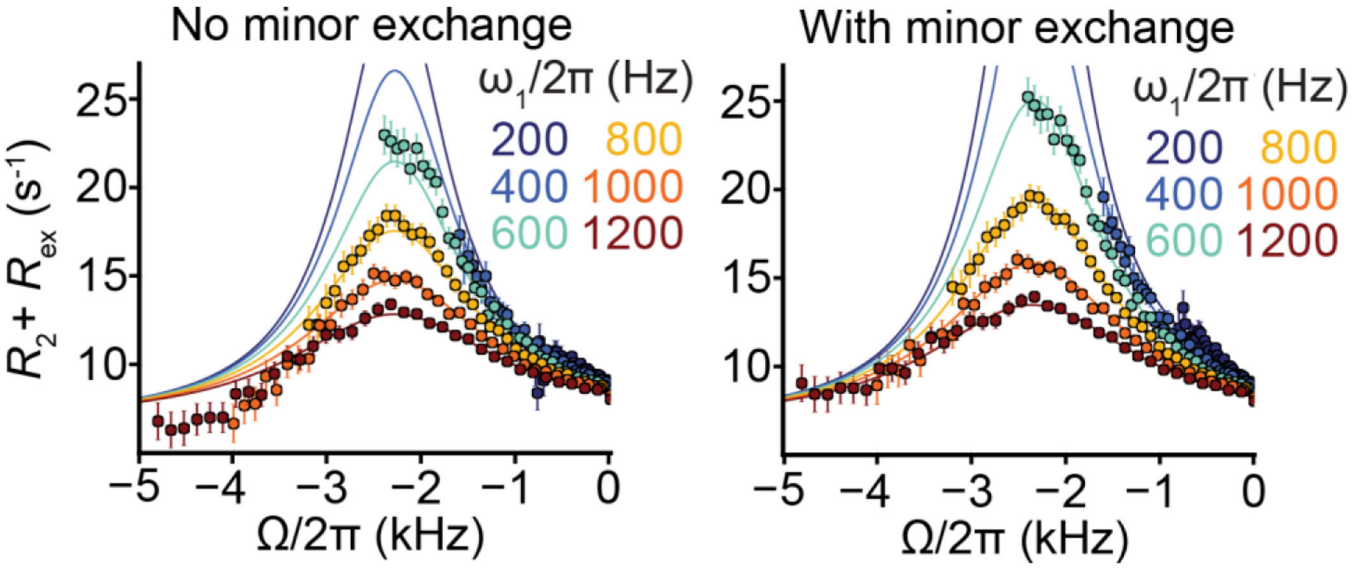

Figure 26.

Representative experimental off-resonance $R_{1\rho}$ RD profiles showing three-state exchange with “minor” exchange i.e., direct exchange between the two excited states[195]. Shown in solid lines are three-state fits to the experimental off-resonance $R_{1\rho}$ RD profiles (hpGT-GGC, pH 8.0, 10 °C) with and without direct “minor” exchange between the two excited states[195], with the inclusion of “minor” exchange fitting the data better. Spin-lock amplitudes are color-coded. Error bars represent experimental uncertainty determined based on a Monte-Carlo error propagation scheme (Section 6.3). The direction of initial alignment of the magnetization during B-M fitting was determined as described in Section 6.1, while taking into consideration the ES with the highest population. Reprinted by permission from [195].

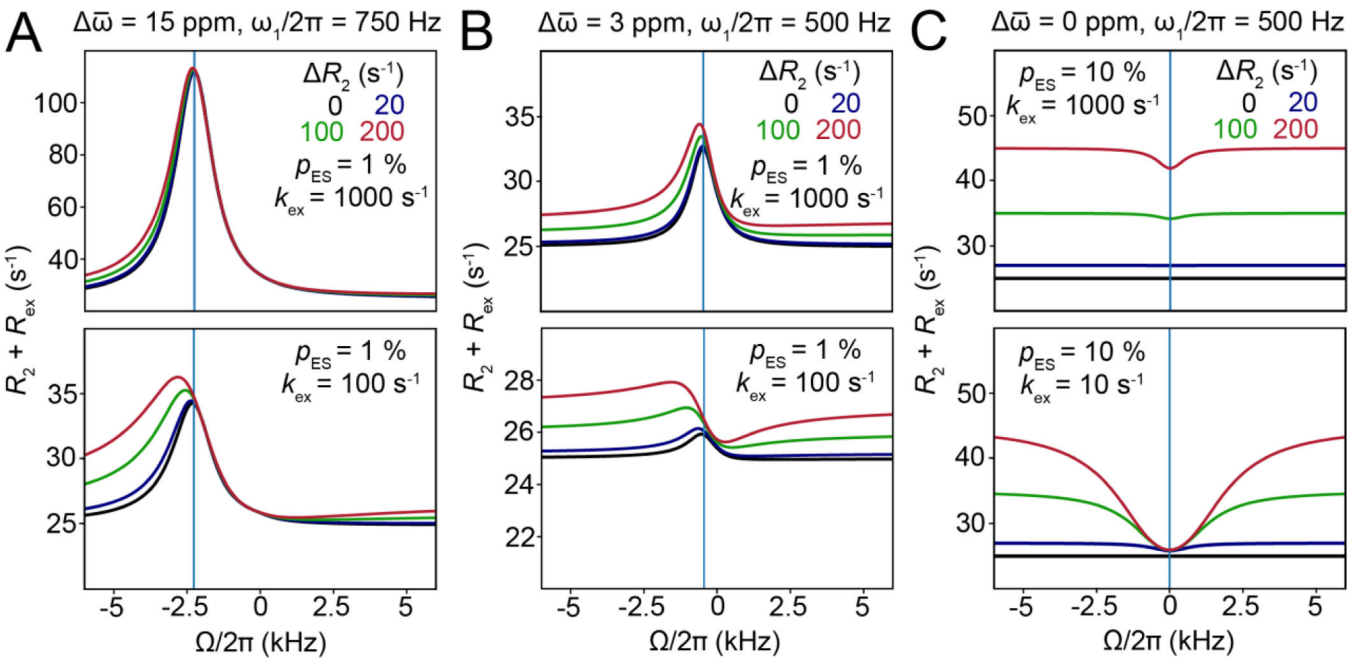

Figure 27.

Impact of unequal $R_{2,GS}$ and $R_{2,ES}$ on off-resonance $R_{1\rho}$ RD profiles for two-state exchange simulated using B-M equations. Variation of off-resonance $R_{1\rho}$ RD profiles with ΔR_2 as function of k_{ex} for A) $\Delta\bar{\omega}(^{13}C) = 15$ ppm, B) $\Delta\bar{\omega}(^{13}C) = 3$ ppm and C) $\Delta\bar{\omega}(^{13}C) = 0$ ppm. Different ΔR_2 values are color coded. Exchange parameters are specified in inset. For all simulations $\gamma(^1H)B_0/2\pi = 700$ MHz and $R_{1,GS} = R_{1,ES} = 2.5\ s^{-1}$. Direction of initial alignment of the magnetization during B-M simulations was determined as described in Section 6.1. While fitting the mono-exponential decay, the magnetization for the first 0.05 s was not considered, in order to exclude the fast initial decay, as proposed by Kay *et al.*[187].

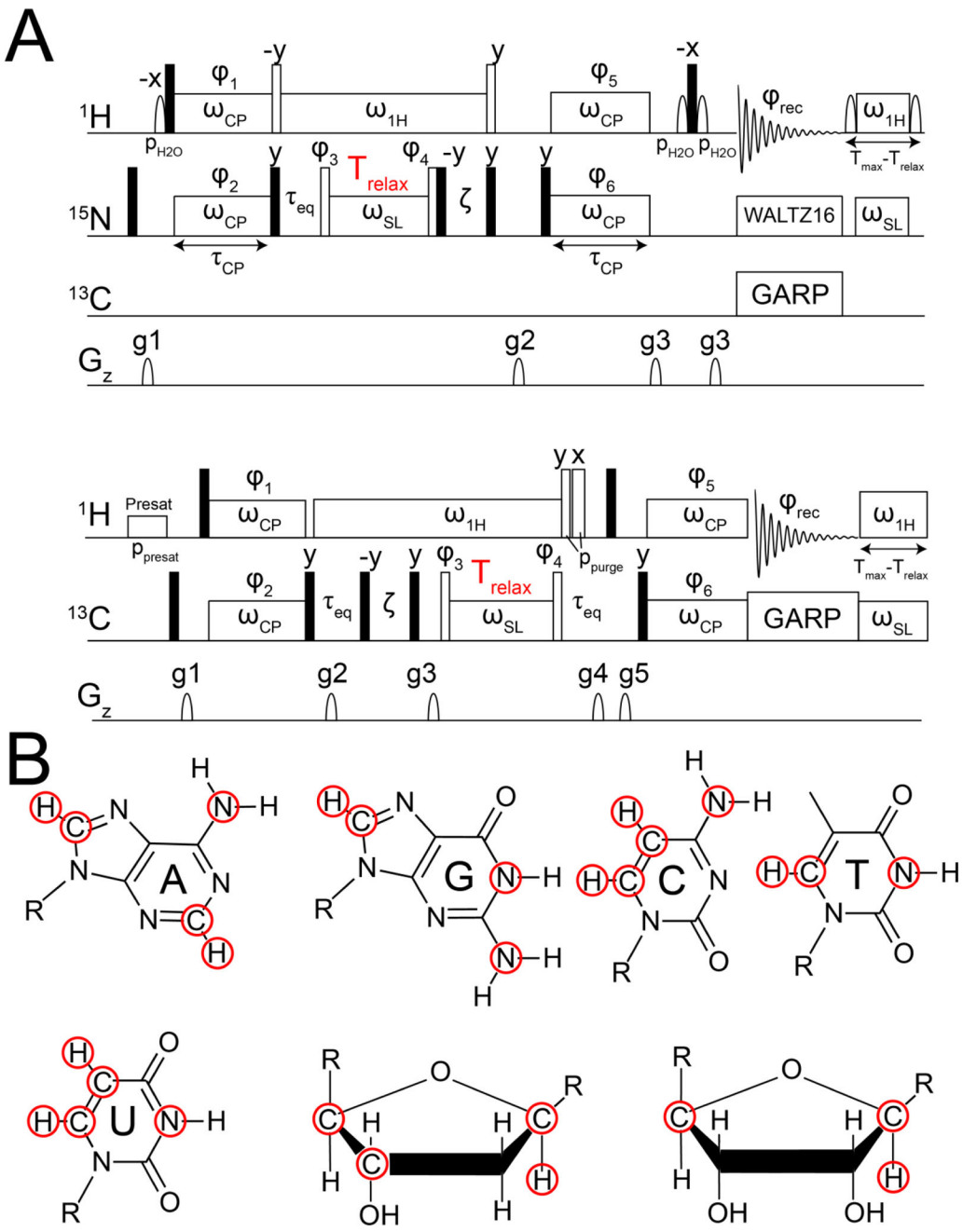

Figure 28.

A) Pulse sequences for measuring off-resonance $R_{1\rho}(^{13}C)$ and $R_{1\rho}(^{15}N)$ in nucleic acids with selective excitation and low spin-lock amplitudes. Hard90° pulses are denoted using filled narrow rectangles, while open narrow rectangles (excluding the purge elements in the ^{13}C sequence) denote hard pulses with flip angles φ. The flip angle φ of the hard pulses φ_3 and φ_4 is equal to $\arctan(\omega_1/\Omega)$, where ω_1 and Ω are the spin-locking amplitude and offset for ^{13}C or ^{15}N. The flip angle of the hard pulse on the proton channel in the ^{15}N $R_{1\rho}$ sequence is equal to $\tan^{-1}(\omega_{1H}/\Omega_H)$ where ω_{1H} is the amplitude of the proton spin-locking field and Ω_H is the frequency offset of the signal of interest from water. Wide open

rectangles denote periods of continuous RF irradiation. Reprinted with permission from [9]. (B) The different spins that can be targeted for $R_{1\rho}$ RD measurements in uniformly $^{13}C/^{15}N$ enriched nucleic acids using the pulse sequences in part (A) are highlighted by red circles. The ^{1}H spins that can be targeted using the 1D $R_{1\rho}$ pulse sequence developed by Petzold *et al.*[222] are also shown using red circles. Spectral crowding in RNA between the C3′ and C2′ sugar carbons prevents measurement of $R_{1\rho}$(C3′ and C2′) in RNA[166] unless one uses selectively labeled samples, while relaxation contributions from germinal protons complicates $R_{1\rho}$(C5′) measurements in both DNA and RNA[166] and $R_{1\rho}$(C2′) measurements in DNA unless selective deuteration is used[131].

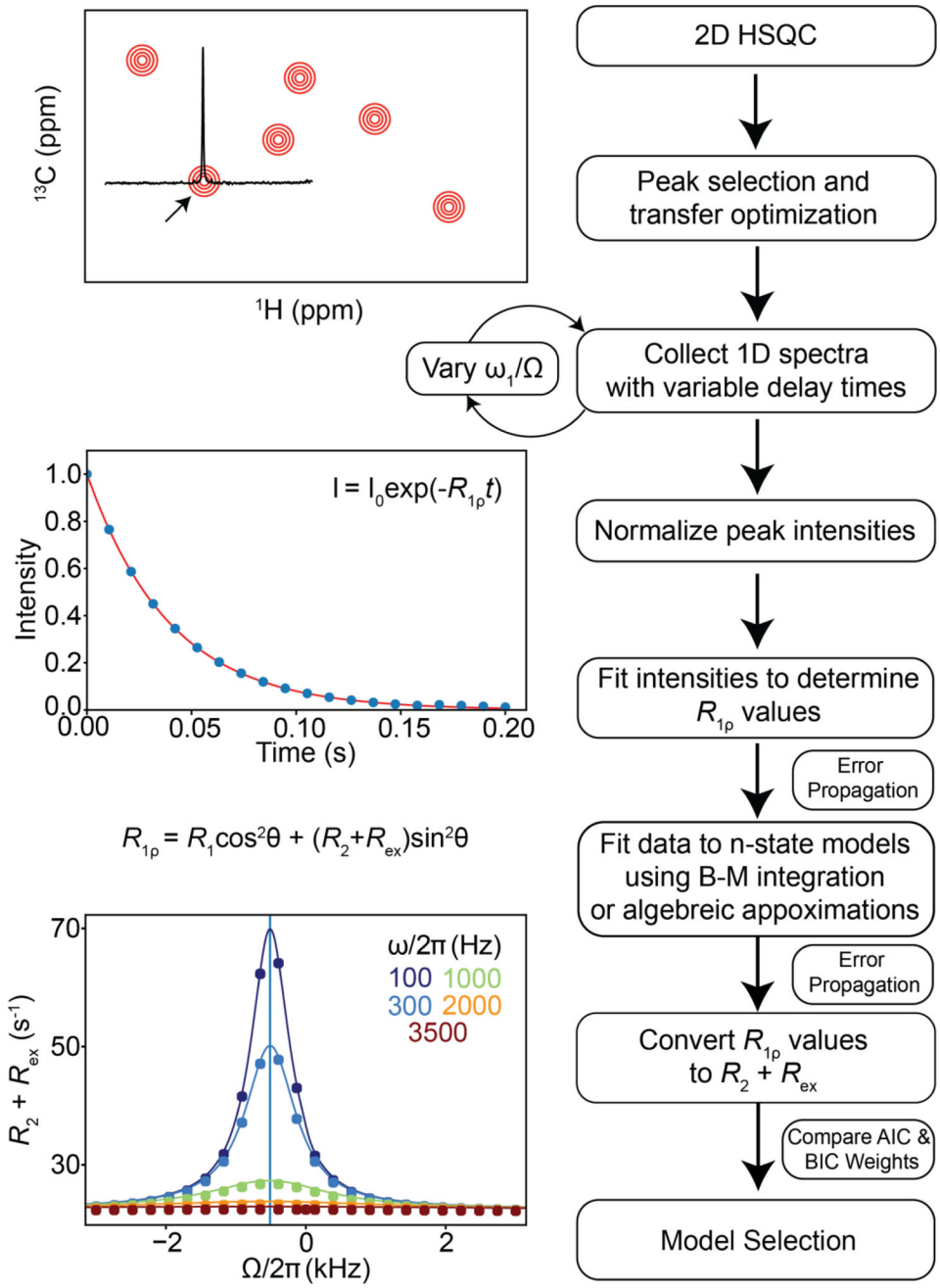

Figure 29.

Flowchart describing the various steps for measuring and analyzing $R_{1\rho}$ RD data using the pulse sequences shown in Fig. 28A.

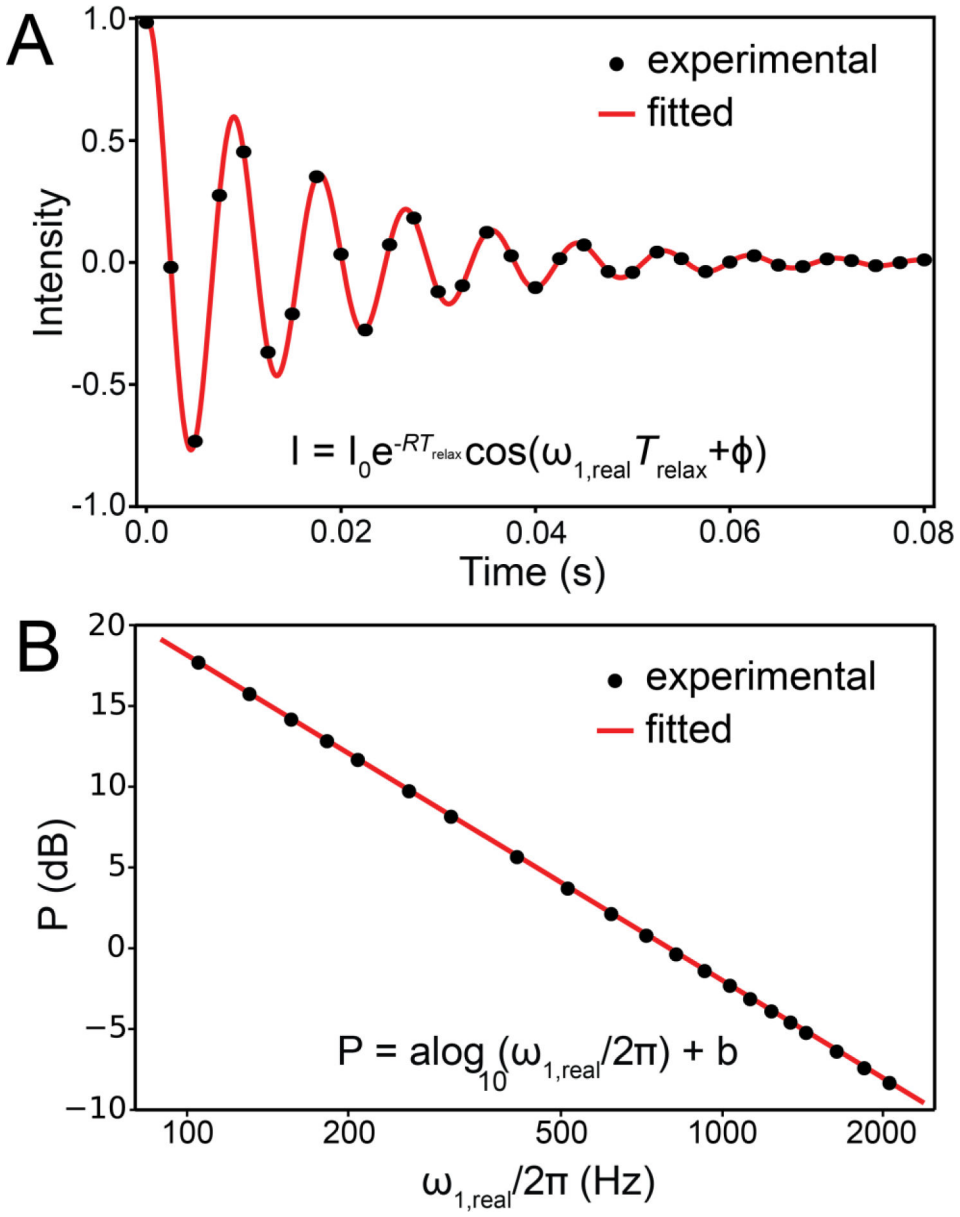

Figure 30.

Calibration of the spin-lock amplitude in $R_{1\rho}$ experiments. A) Nutation curve showing variation of signal intensity (black dots) as a function of time during an $R_{1\rho}$ calibration experiment. The red line is a fit of the intensity to the equation in the inset. B) Variation of the actual spin-lock frequency $\omega_{1,real}$, with the power P of the spin-lock field, obtained by fitting nutation curves in part (A) (black dots). The red line denotes a fit to the equation in the inset.

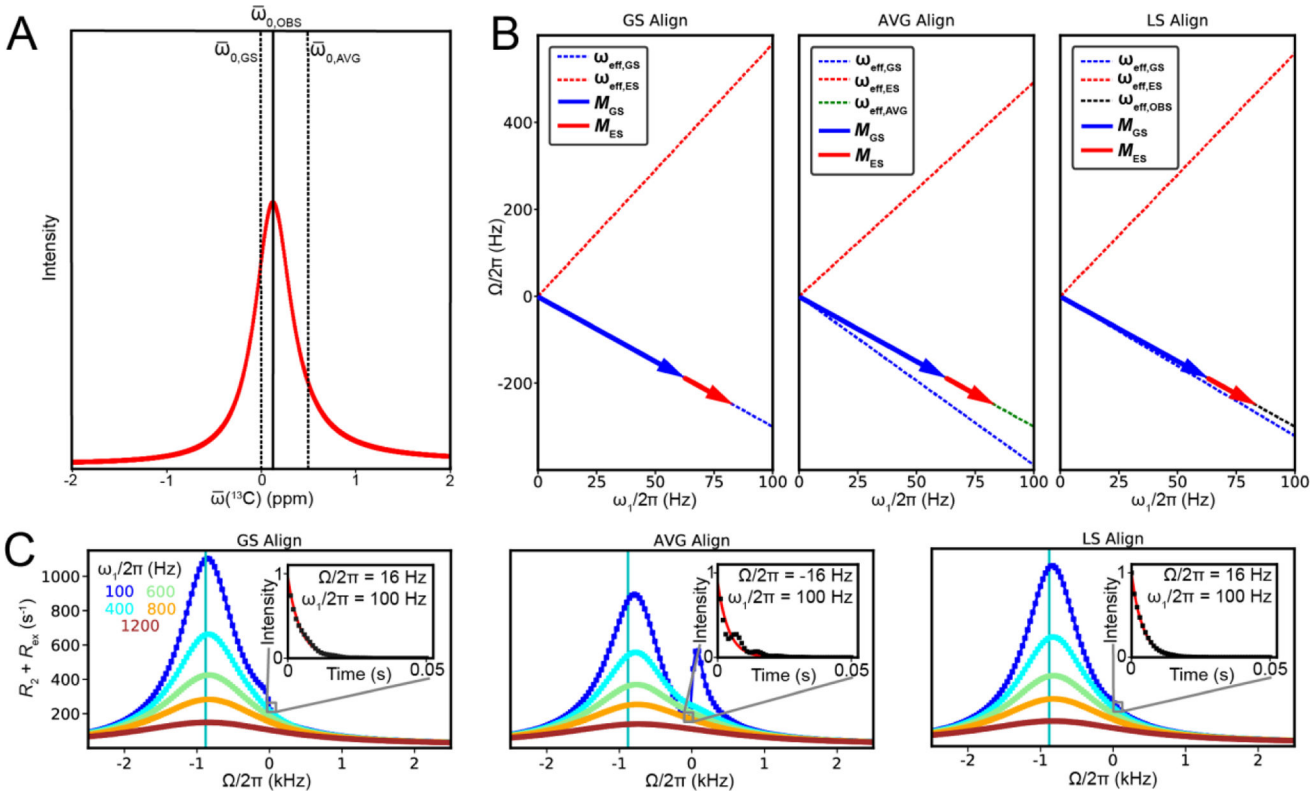

Figure 31.

Asymmetries near 0 offset observed in off-resonance $R_{1\rho}$ RD profiles due to improper alignment of the initial magnetization under intermediate exchange conditions for two-state exchange, obtained using B-M simulations. A) Line shape (LS) simulation using the B-M equations in free precession conditions in the absence of a spin-locking field, for a system in intermediate exchange (p_{ES} = 10 %, k_{ex} = 3000 s^{-1}, $\Delta\bar{\omega}(^{13}C)$ = 5 ppm, $\gamma(^{1}H)B_0/2\pi$ = 700 MHz, $R_{1,GS} = R_{1,ES}$ = 0 s^{-1}, $R_{2,GS} = R_{2,ES}$ = 16 s^{-1}). B) Directions of the effective fields ($\boldsymbol{\omega_{eff,GS}}$: blue, $\boldsymbol{\omega_{eff,ES}}$: red, $\boldsymbol{\omega_{eff,AVG}}$: green, $\boldsymbol{\omega_{eff,OBS}}$: black dotted lines) and initial alignment of the bulk magnetization (GS: blue, ES: red arrows) at the start of the $R_{1\rho}$ experiment ($\omega_1/2\pi$ = 100 Hz, Ω = −300 Hz) for the system in (A) where the magnetization is initially aligned along the effective field of the ground state (GS Align, left), population weighted average (AVG Align, middle) and the observed (OBS) resonance obtained from a lineshape simulation (LS Align, right) . (C) Offresonance $R_{1\rho}$ RD profiles for the system in (A) with $R_{1,GS} = R_{1,ES}$ = 2.5 s^{-1}, when the magnetization is initially aligned along $\boldsymbol{\omega_{eff,GS}}$ (GS Align, left), $\boldsymbol{\omega_{eff,AVG}}$ (AVG align, middle) and $\boldsymbol{\omega_{eff,OBS}}$ (LS Align, right). Note that in all cases, the magnetization at the end of the relaxation delay (0.05 s) is projected parallel to the initial alignment direction to calculate $R_{1\rho}$. The different spin-lock amplitudes are color coded. Also shown in insets are representative decays of the normalized magnetization (black dots) along the initial alignment direction during the relaxation decay, along with exponential fits (red line).

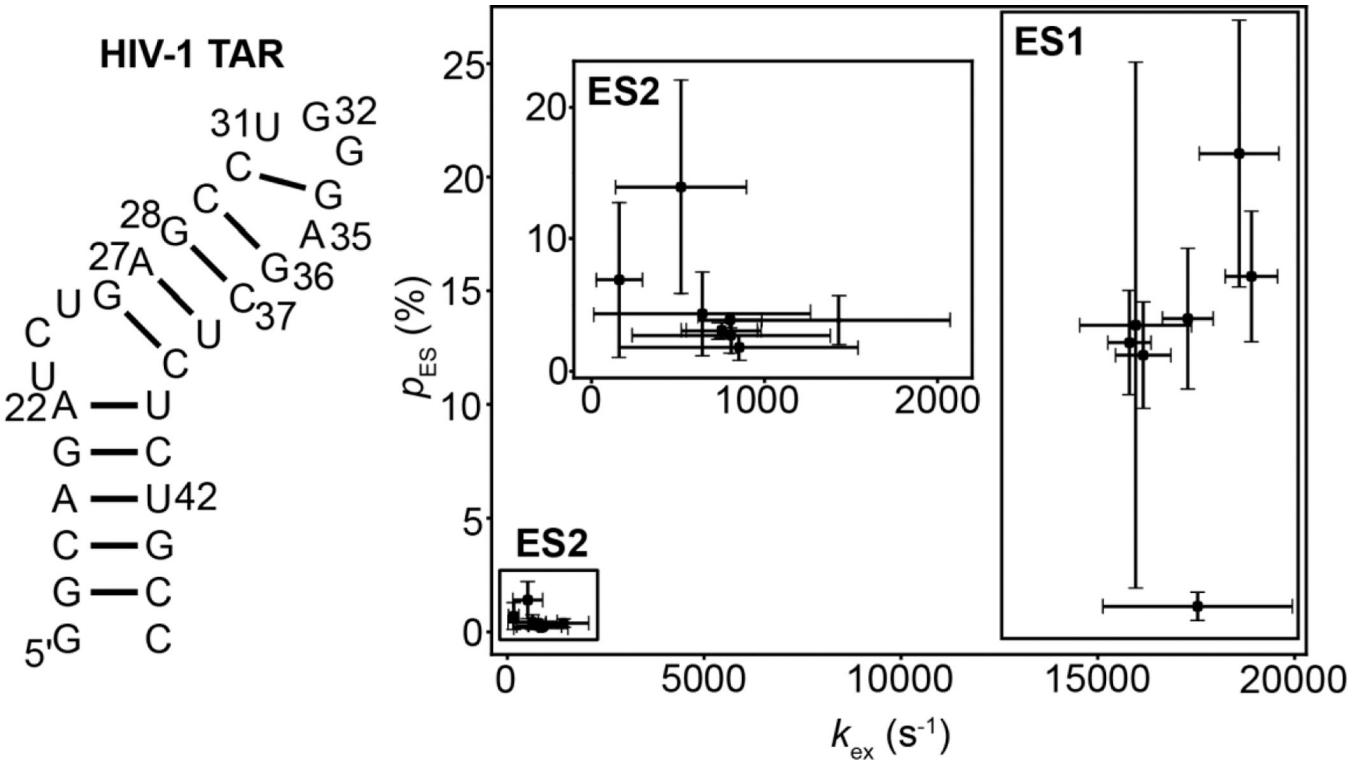

Figure 32.

Deducing the number of ESs sensed by $R_{1\rho}$ RD measurements. A plot of p_{ES} vs. k_{ex} as obtained from $R_{1\rho}$ measurements on individual spins in a given molecule displays clusters corresponding to kinetic and/or thermodynamically distinct ESs. Shown is a representative p_{ES} vs. k_{ex} plot obtained from ^{13}C $R_{1\rho}$ RD (C6/C8/C4′/C1′ spins) measurements on HIV-1 TAR (secondary structure shown on the left) at pH 6.4, 25 °C[166], indicating the presence of two distinct ESs (ES1 and ES2). The zoomed in view of the ES2 region is provided in the inset. Errors were estimated using a Monte-Carlo approach while fitting the individual RD profiles, as explained in Section 6.3.

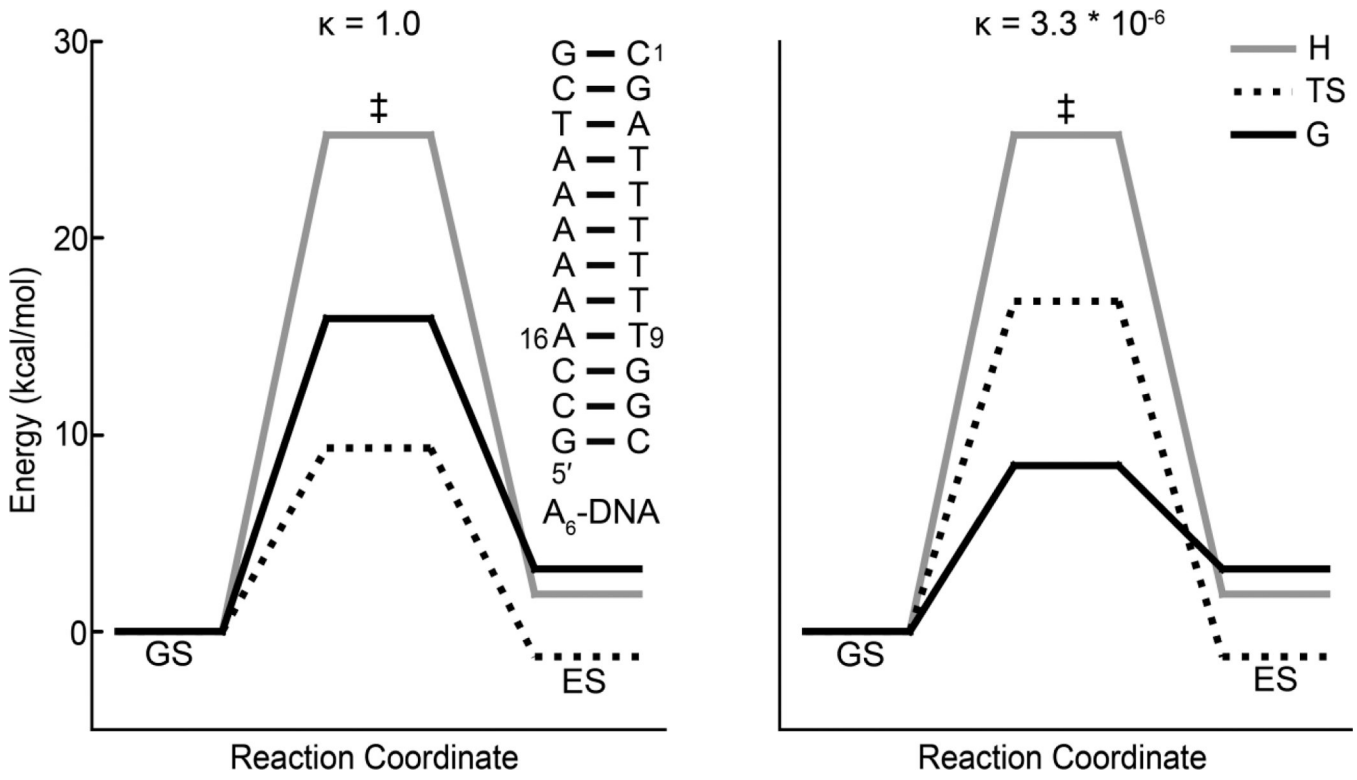

Figure 33.

Thermodynamics and kinetics of GS-ES exchange characterized using temperature dependent $R_{1\rho}$ RD measurements. Free energy diagram (1 kcal/mol = 4.184 kJ/mol) for the Watson-Crick to Hoogsteen transition ($\kappa = 1$, left and $\kappa = 3.3 * 10^{-6}$, right) for A16-T9 in A_6-DNA at pH 5.4, 25 °C obtained using off-resonance $R_{1\rho}$ RD, as reported by Al-Hashimi *et al.*[17]. The secondary structure of A_6-DNA is shown in inset.

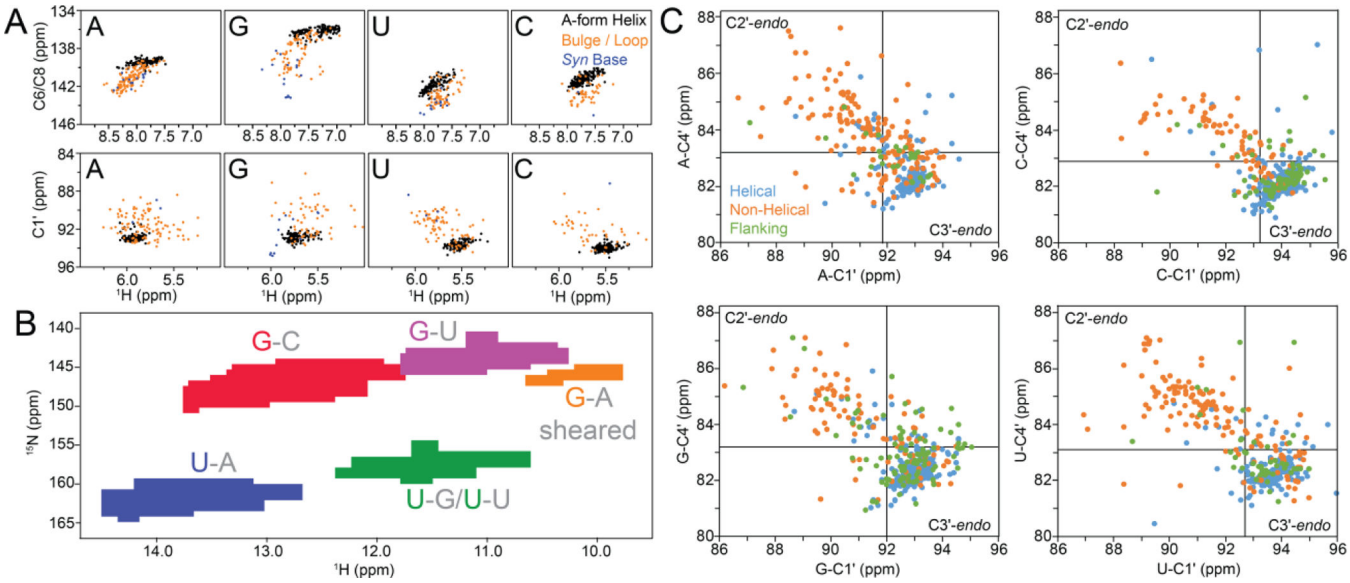

Figure 34.

Chemical shift/structure relationships in nucleic acids can aid structural elucidation of ESs. A) Scatter plot of ^{13}C chemical shifts obtained from the BMRB for different secondary structure contexts in RNA (Watson-Crick BPs in A-form helices: black; nucleotides in bulges, internal or apical loops: gold; *syn* bases: blue). B) Distribution of ^{1}H and ^{15}N chemical shifts for U-N3 and G-N1 as a function of the BP type (G-C Watson-Crick BPs: red; U-A Watson-Crick BPs: blue; G-U wobbles: purple; U-G and U-U wobbles: green; sheared G-A mispairs: orange, with the base whose shifts are shown being colored), as obtained from the BMRB. C) Correlation between the C1′ and C4′ chemical shifts in RNA as obtained from a survey of the BMRB for nucleotides in different structural contexts (helical: blue; non-helical: orange; flanking,i.e., helical BP neighboring loops or bulges: green). Black lines correspond to the upper boundaries for C3′-endo sugar chemical shifts as obtained based on the average and standard deviation of the chemical shifts for helical nucleotides.(A) and (B) were reprinted with permission from [9] while (C) was reproduced with permission from [166].

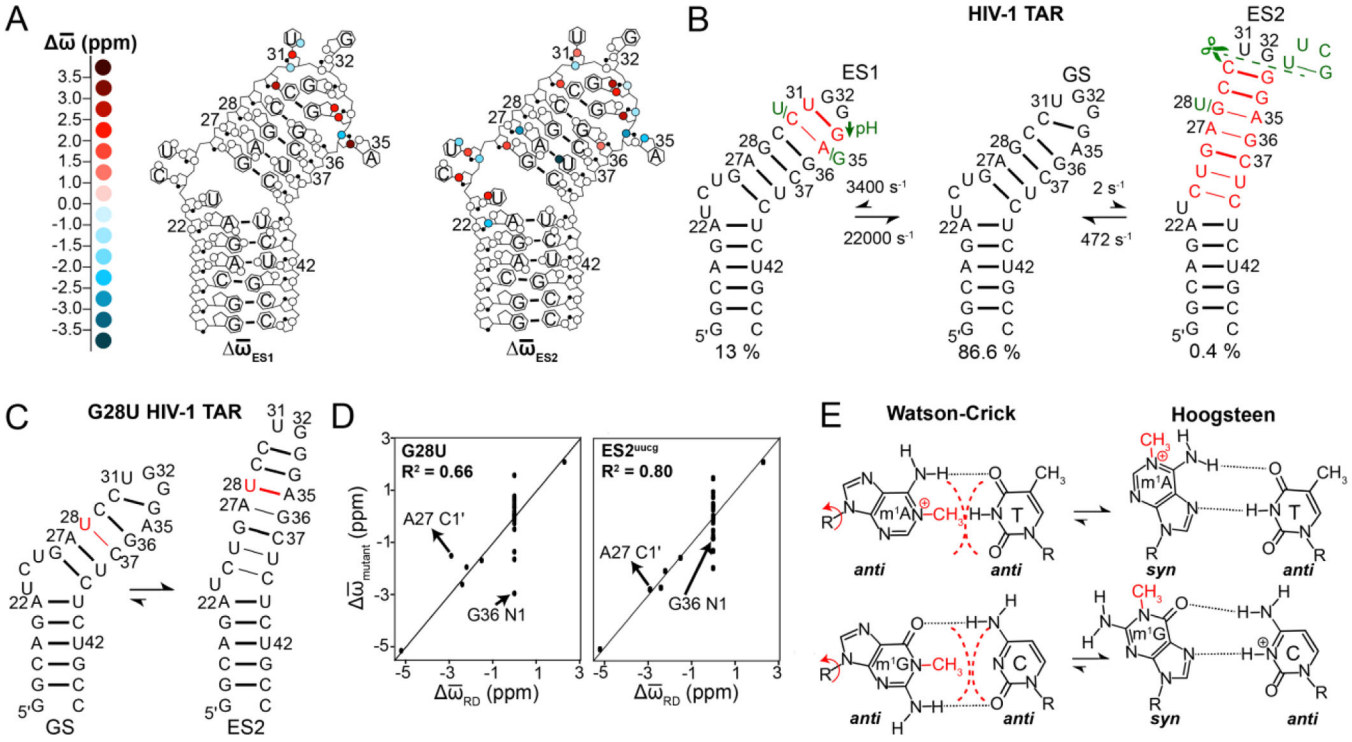

Figure 35.

Probing base pairing in nucleic acid ESs using mutations or chemical modifications designed to stabilize the ES relative to the GS. A) Secondary structure of HIV-1 TAR RNA with the $\Delta\bar{\omega}$ values obtained from off-resonance $R_{1\rho}$ RD experiments[16, 166, 264], color-coded for ES1 and ES2. White circles correspond to sites where no RD was observed. B) Kinetic network of chemical exchange for HIV-1 TAR with ES1 and ES2[16, 264]. Regions undergoing structural changes when transforming into the ES are indicated in red. The exchange rates and populations shown were obtained using NMR RD measurements[16, 264]. Mutations used for stabilizing the ESs are indicated in green. C) Secondary structure of the G28U mutant of HIV-1 TAR in the GS and ES2 conformations. The mutation site is highlighted in red. D)Correlation between $\Delta\bar{\omega}_{\text{mutant}}$, the chemical shift difference between the indicated mutant and unmodified HIV-1 TAR and $\Delta\bar{\omega}_{\text{RD}}$, the change in chemical shift obtained using RD measurements on unmodified HIV-1 TAR, monitoring the GS to ES2 exchange[16, 264]. Vertical line of points at $\Delta\bar{\omega}_{\text{RD}} = 0$ correspond to resonances where RD was flat and $\Delta\bar{\omega}_{\text{RD}}$ was assumed to be equal to zero. E) m^1A and m^1G disrupt Watson-Crick base pairing and create an energetic bias towards the formation of Hoogsteen BPs in DNA. In panels (B) and (C) Watson-Crick BPs and G-U mismatches are indicated using thick lines while thin lines correspond to all other mismatches.

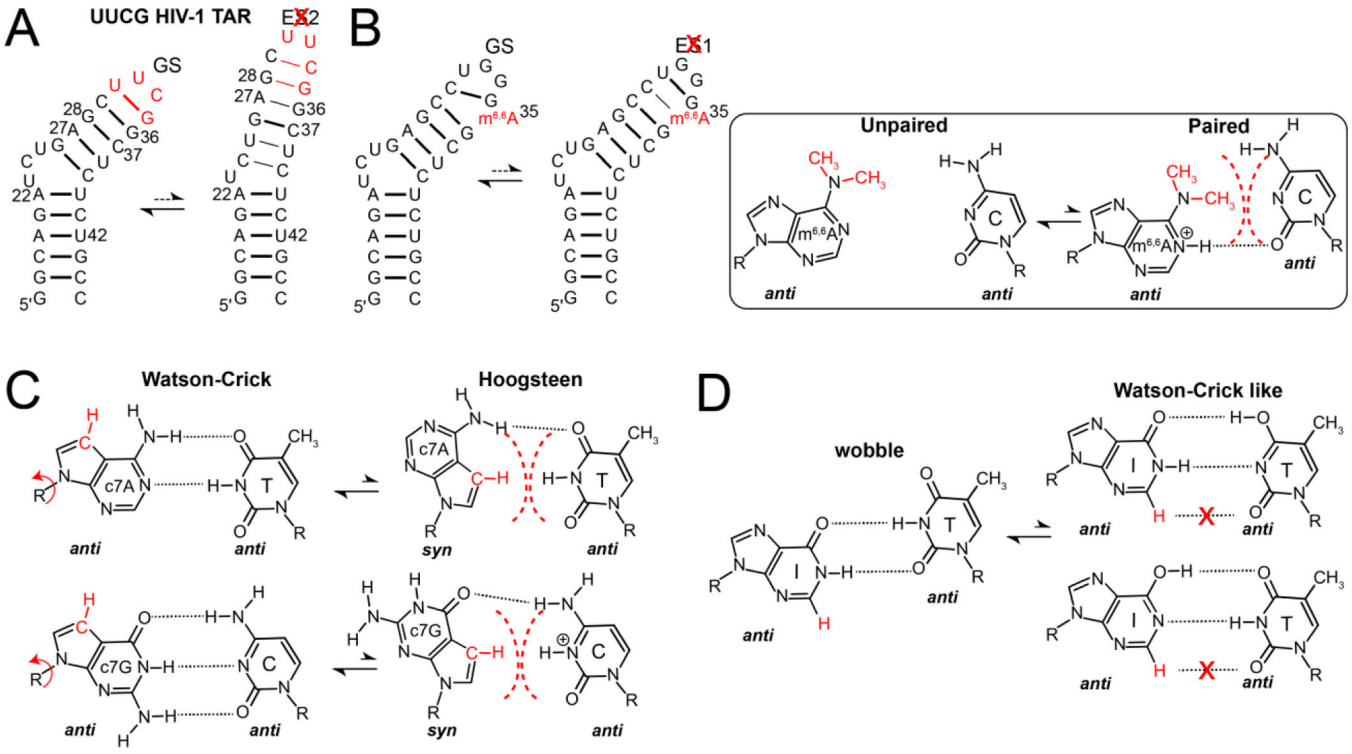

Figure 36.

Probing the structure of nucleic acid ESs using mutations or chemical modifications designed to stabilize the GS relative to the ES. A) Replacement of the HIV-1 TAR apical loop with a UUCG tetraloop destabilizes ES2[264]. B) $N^{6,6}$-dimethyl adenine ($m^{6,6}A$) disrupts base pairing of adenine via the Watson-Crick face in RNA, thereby shifting the GS-ES1 equilibrium in HIV-1 TAR towards the GS[16], in which A35 is unpaired. C) N7-deaza guanine and adenine disrupt Hoogsteen hydrogen bonding and bias A-T and G-C BPs towards the native Watson-Crick conformation[112]. D) Inosine disrupts hydrogen bonding involving the Guanine amino group thereby destabilizing Watson-Crick-like mismatched BPs[165]. In all cases, modifications are highlighted in red. In panels (A) and (B) Watson-Crick BPs and G-U mismatches in the secondary structures are indicated using thick lines while thin lines correspond to all other mismatches.

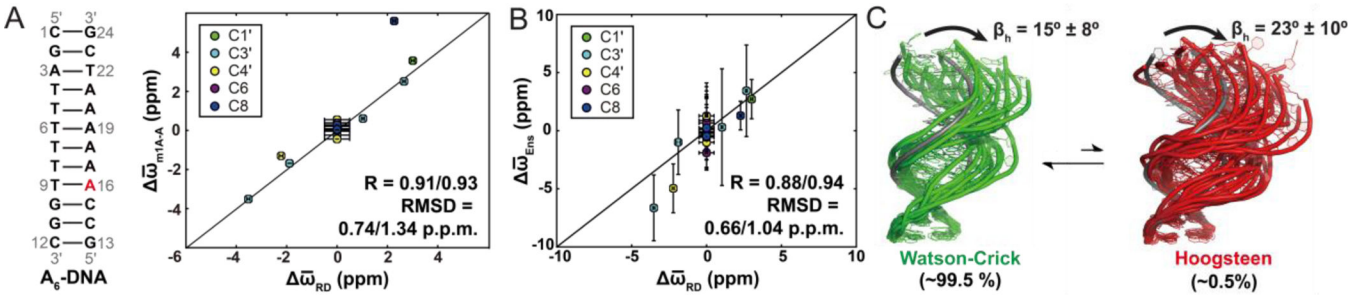

Figure 37.

High-resolution structural characterization of ES Hoogsteen BPs in B-DNA.A) Validation of the ES mutant (m^1A) using an extensive set of chemical shifts. Shown is a representative example of A_6-DNA (secondary structure on the left), with the site of m^1A16 modification to trap Hoogsteen BPs indicated in red. Correlation between $\Delta\bar{\omega}_{m1A-A}$ (the chemical shift difference between the Hoogsteen-stabilizing A_6-DNA^{m1A16} and unmodified A_6-DNA duplex), and $\Delta\bar{\omega}_{RD}$ values obtained from $R_{1\rho}$ RD measurements on unmodified A_6-DNA, monitoring the Watson-Crick to Hoogsteen exchange at A16. B) Correlation between $\Delta\bar{\omega}_{Ens}$, the calculated chemical shift difference between the ensembles of the A_6-DNA^{m1A16} and A_6-DNA duplexes, and $\Delta\bar{\omega}_{RD}$ (C) Dynamic ensembles for A_6-DNA (green, left) and A_6-DNA^{m1A16} (red, right) obtained as described by Al-Hashimi *et al.*[116]. The average inter-helical kink angle β, obtained from an Euler angle analysis[296, 297] is also indicated. In panels A and B, two RMSD and R values are shown. The first value is calculated with the inclusion of all the resonances for which RD was measured, while the second value is calculated excluding data with flat RD where $\Delta\bar{\omega}_{RD}$ was assumed to be zero. Reprinted by permission from [117].

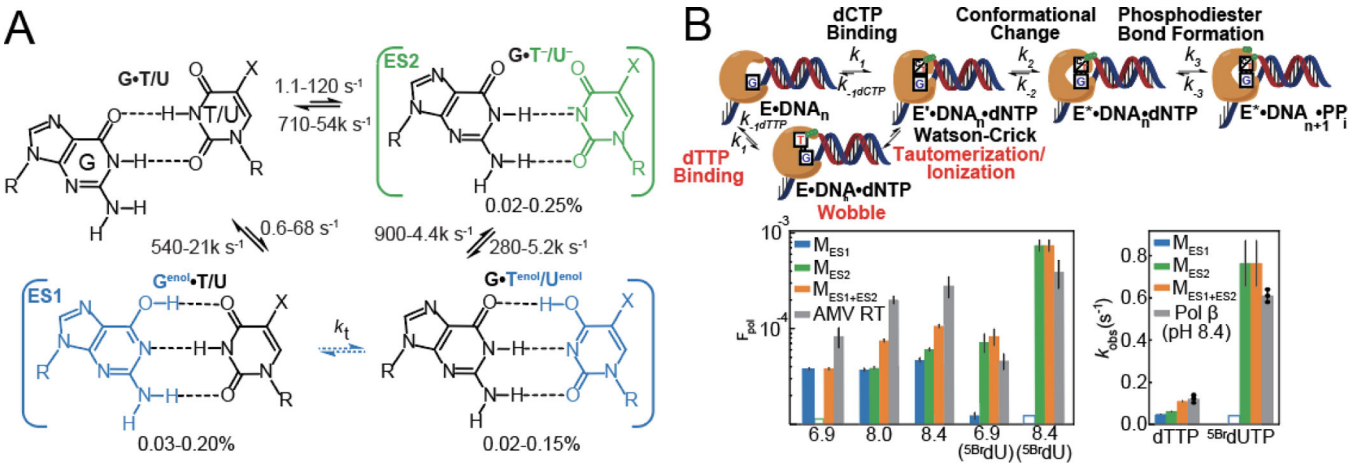

Figure 38.

Watson-Crick-like G-T mismatches and their roles in generating spontaneous mutations during DNA replication. A) Kinetic topology for transforming between G-T/U wobble mismatches and their Watson-Crick-like counterparts formed via tautomerization or ionization. The exchange rates shown were obtained using NMR RD measurements[195, 197]. B) Minimal kinetic model for Watson-Crick BP incorporation by DNA polymerases. The incorporation of a G-T mismatch requires in addition, as shown in the lower pathway, a tautomerization or ionization step allowing for the formation of a Watson-Crick-like species. (Bottom left) Histograms showing F_{pol}, the fidelity of dTTP/^{5Br}dUTP mis-incorporation errors catalyzed by Alfalfa Mosaic Virus Reverse Transcriptase (AMV RT) as computed using kinetic simulations allowing incorporation of tautomeric (blue, M_{ES1}), ionic (green, M_{ES2}) or both (orange, M_{ES1} + M_{ES2}) Watson-Crick-like excited states, and experimentally measured values (gray).(Bottom right) Measured and simulated rates (k_{obs}) of mis-incorporation for dTTP/^{5Br}dUTP catalyzed by human DNA polymerase β. Reprinted by permission from [195].

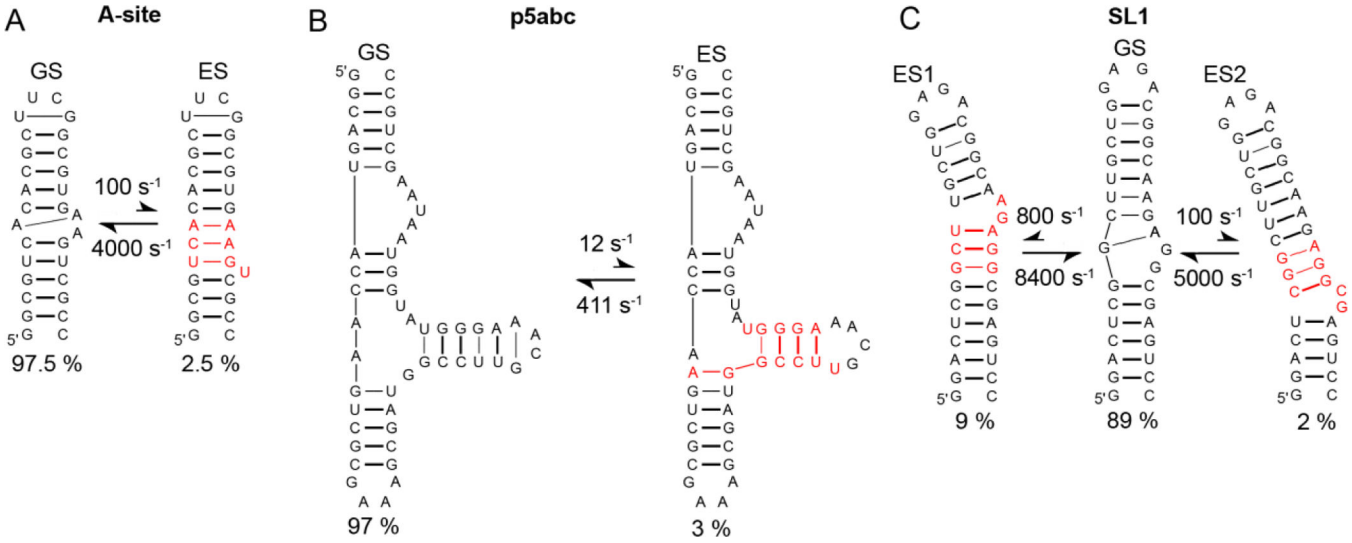

Figure 39.

RNA ESs feature localized changes in secondary structure. Shown are the secondary structures of ES determined for A) bacterial A-site, B) p5abc and C) HIV-SL1 using selective 1D $R_{1\rho}$ RD measurements. The part of the ES undergoing structural changes on transforming from the GS is indicated in red. Thick lines correspond to Watson-Crick BPs and G-U mismatches, whereas thin lines denote other non-canonical mispairing. The populations of the states and the rate constants for GS-ES exchange, as obtained using $R_{1\rho}$ RD measurements[9, 16] are also shown.

Table 1.

Optimal settings for 1D off-resonance $R_{1\rho}$ experiments using the pulse sequences shown in Fig. 21A

Parameter	Optimal Value	
$\omega_{CP}/2\pi$ [a]	85 Hz [b, c]	
τ_{CP}	~1/4 $\lvert^1J_{AH}\rvert$ [d], ~3/4 $\lvert^1J_{AH}\rvert$ [e]	
T_{eq}	~3/k_{ex}	
$\omega_1/2\pi$ [f]	G-N1/U-N3	> ~50 Hz
	A-C8/G-C8	> ~45 Hz
	A-C2	> ~40 Hz
	C1′/C3′/C4′	> ~150 Hz
	C-C6/C-C5/U-C6/U-C5/T-C6	> ~200 Hz
	A-NH2/G-NH2/C-NH2	> ~70 Hz
$\omega_{1H}/2\pi$	~10 kHz for ^{13}C and ~5 – 8 kHz for ^{15}N [g]	
ζ	$\pi/2\delta$ [h]	

[a] $(\omega_{CP}/2\pi) > 3^{1/2}/4\ \lvert^1J_{AH}\rvert$, A = ^{13}C/^{15}N

[b] $R_{1\rho}(^{15}N)$ measurements on imino ^{15}N (N1/N3). In theory, $\omega_{CP}/2\pi$ should be chosen to be equal to $3^{1/2}J_{IS}/4$, the smallest value that can lead to complete magnetization transfer between spins, while also being selective and less sensitive to RF field inhomogeneities and mismatches in the Hartmann-Hahn matching condition[216]. However, in practice, a value of $\omega_{CP}/2\pi$ (= 85 Hz) larger than $3^{1/2}J_{IS}/4$ ~ 39 Hz is typically employed so as to minimize losses of the magnetization due to conformational exchange[163].

[c] $R_{1\rho}(^{13}C)$ measurements on aromatic and sugar ^{13}C nuclei (C2/C5/C6/C8/C1′/C3′/C4′)

[d] For AX (e.g. N1–H1 and C8–H8) and non-equivalent AX_2 (e.g. amino NH_2 group in WatsonCrick G-C BPs) spin systems[161, 217]

[e] For equivalent AX_2 spin systems (e.g. amino NH_2 group in G-T/U wobbles)[161].

[f] Should be greater than 3 times $^2J_{NN}$ or $^1J_{CC}$[21, 28]. The largest value that can be used depends on probe hardware limitations.

[g] Should be > $\omega_{eff(max)}$

[h] δ is the offset in Hz of the undesired resonance in the ^{13}C/^{15}N dimension from the resonance of interest

Table 2.

Offsets for $R_{1\rho}(^{13}C)$ measurements in nucleic acids that are susceptible to Hartmann-Hahn transfers during application of a spin-lock.

Magnetization transfer between nuclei that are coupled to each other can serve as an extraneous mode of relaxation during the application of spin-locking pulses in an $R_{1\rho}$ experiment. Offset values that are susceptible to such magnetization transfer via attainment of a Hartmann-Hahn matching condition (efficiency $A_{\mathrm{HAHA}} > 1\%$, Eqn. 55) for a pair of spins S1 and S2 were computed assuming $\gamma(^1\mathrm{H})B_0/2\pi = 700$ MHz and spin-lock amplitudes between 50–3600 Hz. J_n is the multiple-bond scalar coupling constant between the spins under consideration while $\Delta\bar{\omega}_{\mathrm{S2-S1,avg}}$ is the average difference in chemical shift between them. J_n couplings were obtained by van Buuren *et al.*[218].

S1	S2	Nucleic Acid	J_n(Hz)	$\Delta\bar{\omega}_{\mathrm{S2-S1,avg}}$(ppm)	Offsets (Hz)
C4′	C5′	RNA	−40	−17	(−1700, −1300)
C4′	C3′	RNA	−40	−9	(−900, −700)
C4′	C5′	DNA	−40	−20	(−1900, −1600)
C4′	C3′	DNA	−40	−9	(−900, −700)
C3′	C4′	DNA	−40	9	(700, 900)
C3′	C2′	DNA	−40	−38	(−3500, −3100)
C1′	C2′	RNA	−42	−15	(−1450, −1150)
C1′	C2′	DNA	−42	−46	(−4200, −3900)
C/U-C6	C/U-C5	RNA/DNA	−68	−44	(−4100, −3600)
C/U-C5	C/U-C6	RNA/DNA	−68	44	(3600, 4100)
C/U-C5	C/U-C4	RNA/DNA	−60	70	(5800, 6400)